NIELS BOHR INSTITUTE
THE GRADUATE SCHOOL OF SCIENCE
FACULTY OF SCIENCE
UNIVERSITY OF COPENHAGEN
DENMARK

PhD thesis

Julia Preu

Structural changes in charged membrane models systems

Academic advisor: Prof. Dr. Thomas Heimburg
Dr. Thomas Gutberlet

Submitted: 20.04.2010

Abstract

The thesis presented here is result of the work performed as member of the Marie Curie Research Training Network BioControl - Bio-interfaces: From molecular understanding to application, conducted in the Laboratory for Neutron Scattering at the Paul Scherrer Institute and in the Membrane Biophysics Group at the Niels Bohr Institute. The work will focus on the influence of charges on model membrane systems. Lung surfactant and bacterial cell membranes are rich in charged lipids, an example is the short-chained anionic phospholipid dimyristoylphatidylglycerol. Particular interesting about this lipid is a complex melting behaviour accompanied by changes in the optical and viscous behaviour, limited by the amount of salt in the buffer. So far it was not possible to get a handle on the underlying morphological changes and the particular driving forces. This challenge was mainly addressed by means of scattering techniques using light, x-rays and neutrons as sources of radiation. To be highlighted is the use of a combination of rheology and small angle neutron scattering, allowing to study structural changes under the influence of shear. Together with the application of differential scanning calorimetry, rheology and confocal fluorescence microscopy a decreased degree of bilayer fluctuations could be shown, especially in comparison to analog zwitterionic lipids.

Charges also play an important role for the interaction of membrane-active compounds with the membrane. This is shown by comparing the interaction of the blood pressure regulating petide-hormone Angiotensin II, the drug Losartan and its active derivate E-3174 with model membranes. For Angiotensin II a concentration dependent binding to the membrane could be shown. Losartan and E-3174, even though quite similar in their molecular structure exhibit differences in their way of binding to the membrane, that for all three compounds may contribute to their in vivo function.

Danske resume

Denne afhandling er resultatet af arbejde, der blev udført som medlem af Marie Curie Research Training Network BioControl - Bio-interfaces: From molecular understanding to application i Laboratory for Neutron Scattering ved Paul Scherrer Instituttet og i Membrane Biophysics Group ved Niels Bohr Instituttet. Arbejdet fokuserede på hvorledes elektriske ladninger påvirker modelmembransystemer.

Lungesurfaktanter og bakteriers cellemembraner har et højt indhold af ladet lipider. Et eksempel herpå er den kortkædet, anioniske fosfolipid dimyristoylphatidylglycerol. En interessant egenskab ved denne lipid er dens komplekse opførelse når den smelter, som akkompagneres af ændringer i både viskositet og de optiske egenskaber af systemet. Disse ændringer kan begrænses ved at øge mængden af salt i bufferen. Indtil videre har det ikke været muligt at få styr på de underliggende ændringer i morfologi og, i særdeleshed, drivkræfter. Disse spørgsmål blev primært undersøgt ved hjælp af lys-, røntgen-, og neutronspredning. Mere specifikt, så blev der benyttet en kombination af reologi og småvinkel neutronspredning, hvilket tillod os at studere strukturændringer som følge af forskydningsspændinger. Ved anvendelse af differentiel scanning kalorimetri, reologi og konfokalmikroskopi kunne vi vise at membranfluktuationerne reduceres, især i forhold til de tilsvarende zwitterioniske lipider.

Elektriske ladninger spiller også en vigtig rolle for interaktionerne mellem membrane-aktive stoffer og selve membranen. Dette er blevet vist ved at sammenligne interaktionen mellem modelmembraner og det blodtryksregulerende peptidhormon, Angiotensin II, stoffet Losartan og dets aktive derivat, E-3174. For Angiotensin II kunne en koncentrationsafhængig binding til membranen påvises. Losartan og E-3174 udviser også forskelle i måden hvorpå de binder til membranen, til trods for at de næsten er identiske i deres molekylære struktur. Disse forskelle kan bidrage til alle tre stoffers *in vivo* funktion.

Contents

Chapter 1

Introduction

1.1 Cells and membranes

1.1.1 Cells as basic units of biological live

Thinking about life, in a biological sense, it is characterized by self-sustaining biological processes, making the difference to inorganic non-living matter. Apart from viruses, where there is room for discussion, single cells are considered as the simplest units of life, capable to sustain independent function. Examples for this level of organization are bacteria or red blood cells. Higher forms of organization are found in tissues and organs, with cells fulfilling more complex functions in a regulated network. Cells differ in their architecture from unilamellar prokaryotic cells, like bacteria to eukaryotic cells containing a nucleus and organelles, a schematic representation is found in Figure 1.1 a. The main difference between prokaryotic and eukaryotic cells is the absence or presence of compartments dividing the cell lumen in discrete sections by a lipid layer. These compartments and organelles fulfill a variety of functions, ensuring the spacial localization and targeting of molecules and are involved in signaling cascades. It is accepted today that some organelles, like the mitochondria and plastids originate from serial endocytotic uptake of bacteria by other bacteria [1][2][3].

1.1.2 Cell membrane

Common to all cells is a cell membrane functioning as an active barrier, dividing the interiour of a cell towards the surrounding. This film, with an on average three nm thick hydrophobic core, consists mainly of proteins and lipids and is unique for each cell type and tissue (Figure 1.1 b) [5]. The variety of chemically different and modified lipids and proteins leads

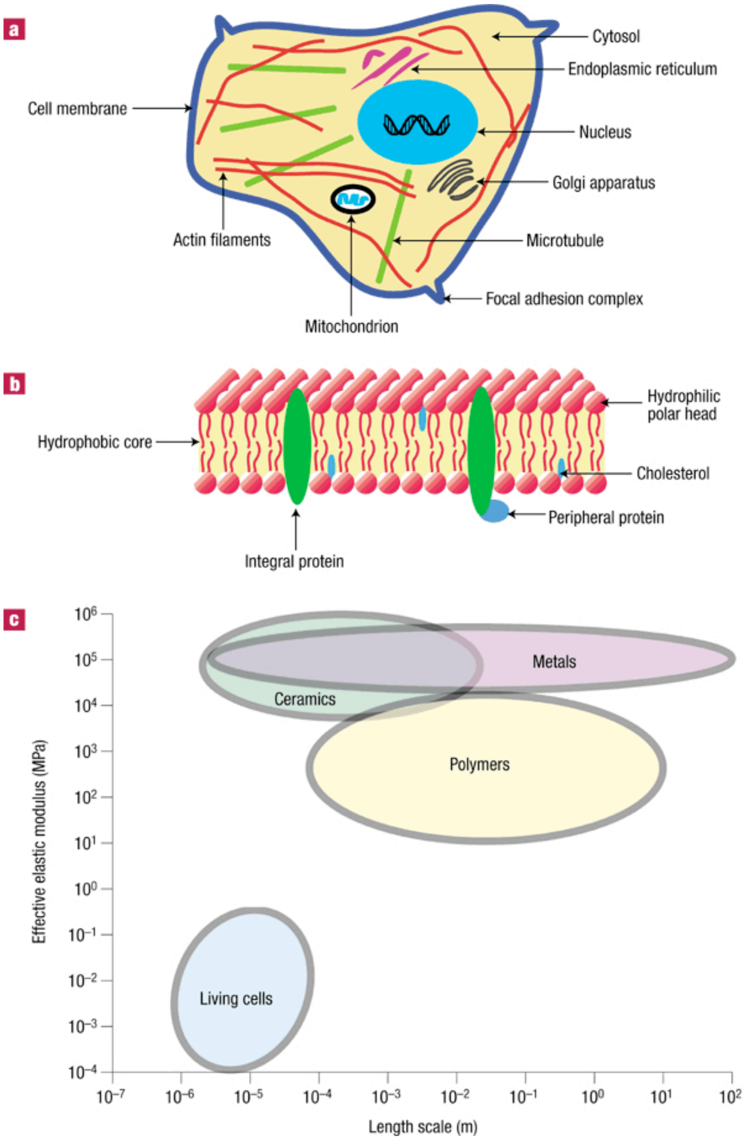

Figure 1.1: Cell structure and elastic properties. a, Schematic diagram of a typical eukaryotic cell, which contains many subcellular elements. b, The membrane comprises a phospholipid bilayer, with hydrophilic heads and hydrophobic tails, whose mechanical rigidity is altered by the presence of integral protein molecules and cholesterol. c, Approximate range of values for the elastic modulus of biological cells and comparisons with those of engineering metals, ceramics and polymers. (From [4])

to a dynamic organization across the bilayer and in the lateral dimension [5]. The proteins existing as peripheral and integrated membrane proteins can be attached to the membrane, e.g. by lipid anchors or span the membrane with hydrophobic helices or sheet structures [6]. The lipids are amphipatic, containing a hydrophobic and hydrophilic section, whereas the hydrophobic moieties tend to self-aggregate, the hydrophilic parts interact with the aqueous environment. This spontaneous emergence of order tends to contradict with the second law of thermodynamics. In a closed thermodynamic system the entropy is approaching a maximum and an ordered state emerges in equlibrium, even though it is static [7]. In a thermodynamically open system the energy that flows through it can be used to decrease the entropy. This principle gave rise to the first cells and is responsible for the occurance of discrete organelles. Open is the origin and maintenance of the structure. It is still unclear if the overall lateral organization, for example after cell division, is achieved by *de novo* or templated synthesis [8], but it is accepted that the lateral organization is a key feature for the functioning of a membrane. In recent years the model for the membrane architecture changed and evolved from the fluid-mosaic model, as introdued by Singer and Nicholsen [9], to a more dynamic structural organization [10] paying respect to the heterogenity in thickness, the emergence of domains [11] and a dynamic rearrangement of the lipids and the proteins [12] to substain function [13][14]. This view on the membrane contributes to a better understanding of biological function [15] and dysfunction and lipid-associated disorders like Artherosclerosis, the Tangier and the Niemann-Pick disease type C [16]. In early onset of Artherosclerosis plasma lipoproteins get accumulated in the subendothelium of focal areas of the arterial tree and the retained lipoproteins stay in the arterial walls due to the increased particle size [17]. Apart from an unusual type of inflammation [18], in particular oxidized phospholipids that derive from modified lipoproteins lead to an increase in the formation of the known plaques [19].

1.2 Lipids

Biological lipids are, in the most general case, defined as water insoluble molecules. This rather general definition comprises a variety of chemically different molecules, giving rise to diverse function. Fats and oils are used as energy storage molecules whereas phospholipids, glycolipids and some sterols are functioning as structural lipids in the cell membrane. These two classes build the major fraction of lipids. A number of less abundant lipids plays a crucial role, functioning in signal transduction, like steroid hormones or as pigments, like retinal.

The structural lipids contributing to the membrane structure can be grouped in three categories, phospholipids, glycolipids and ether lipids as found in Archaebacteria (Figure 1.2). Focusing on the glyerophospholipids, they vary in the length and degree of unsaturation of the acyl chains and the headgroup. Common are chain lengths between twelve and 24 carbon atoms and up to four double bonds. The five alcohols, building the headgroup together with the phosphate group, are serine, glycerol, ethanolamine, inositol and choline, depending on their charge, the lipids are zwitterionic or anionic.

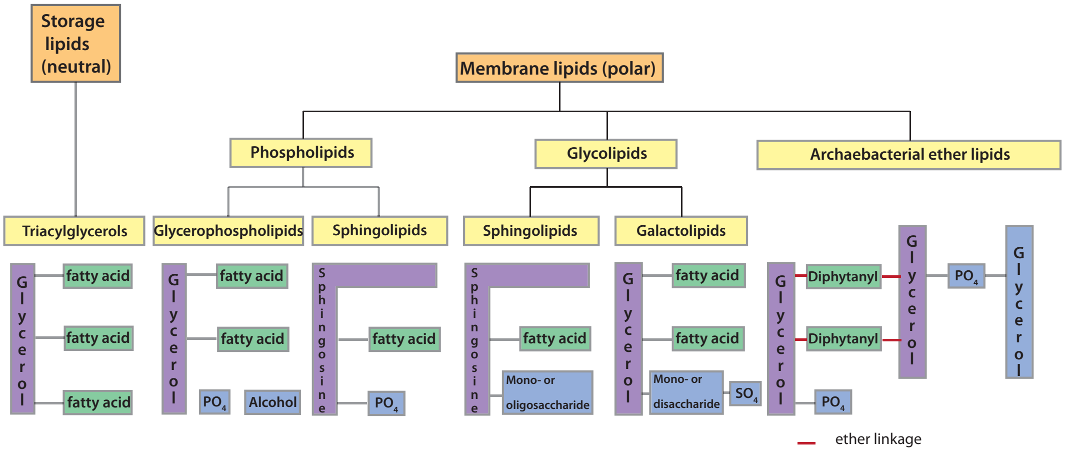

Figure 1.2: Overview of the most abundant lipids and their building blocks. Lipids can be grouped in storage and membrane lipids. In the membrane the different lipids are grouped referring to the backbone alcohol and the different headgroups.

1.2.1 Pure lipid dispersions as membrane models

Even if one is only considering lipids abundant in the cell membranes and organelles, their heterogenity makes it complicated to derive meaningful information from most experimental techniques. A strategy to overcome this difficulty lies in the use of model systems, in the most simple case pure lipid dispersions. Immersing lipids in water leads to the spontaneous formation of discrete shapes, most common are micelles, vesicles and bilayers as sketched in Figure 1.3.

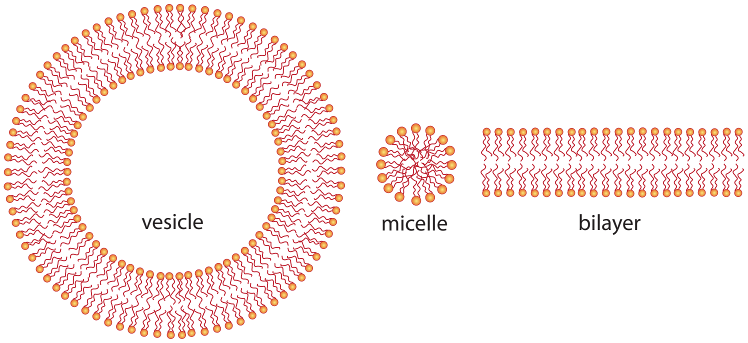

Figure 1.3: Common shapes emerging from lipids dispersed in water, vesicles, micelles and bilayers.

Other structures occur under certain conditions, as high lipid content, variation of temperature, pH and addition of divalent cations, sugars, or other charged molecules for instance ordered structures, as different cubic, hexagonal and inverted hexagonal phase or other less ordered species as different network structures or inverted micelles. Some of this shapes have only little biological relevance, whereas others are versatile tools to model biological functions, like processes in neurotransmission, the fusion and fission of synaptic vesicles, endo- and exocytosis and viral fusion. The emergence of phenomena like high membrane curvature, the maintenance of curvature in organelles like the inner membrane of mitochondria and the cisternae of the endoplasmatic reticulum can be addressed. The preservation of this functions and structures is depending on manifold internal and external factors. Internal features, as the chemical composition are varying over time, the same is true for the external factors, like pH and temperature. In a model system the stoichiometry of the chemical compounds, pH, ionic strength, temperature and pressure can be defined, monitored and altered in a controlled fashion. Even for single lipid dispersions with a defined composition it can be challenging to understand the interplay of all factors giving rise to structural changes. This phenomena will now be introduced for a charged lipid.

1.3 Charged phospholipids - The case of DMPG

Charged phospholipids are found in all cell membranes, especially bacterial cell membranes are rich in charged lipids. In higher organisms charged lipids can be found in the lung as pulmonary surfactant, responsible for the reduction of the surface tension. The lipids are adsorbing to the air-water interface with the hydrophobic part pointing towards the air interface and the hydrophilic in contact with the water. More then ten percent of the lung surfactant are build by short chained phosphadidylglycerols [20].

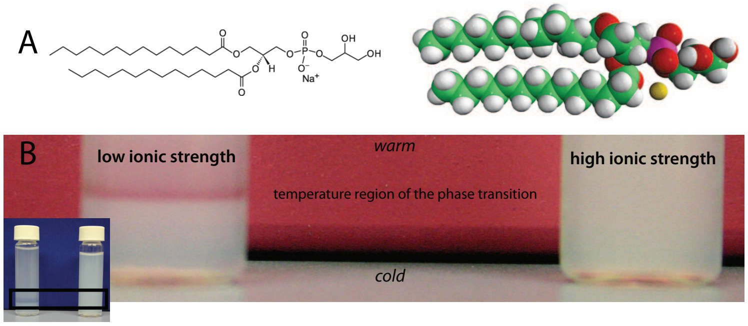

Figure 1.4: (A) chemical drawing (left) and room-filling model (right) of DMPG, (B) picture of vials filled with DMPG at low ionic strength (left) and high ionic strength (right). In the dispersion with low ionic strength a transparent band can be observed, at a temperature that is corresponding to the temperature of the phase transition.

Dispersing charged phospholipids in water and comparing them with similar zwitterionic lipids reveals some interesting differences. Early calorimetric studies comparing zwitterionic and charged lipids indicated that, according to the Gouy-Chapmann theory, the temperature of the phase transition is depending on the charge density [21]. Apart from "just" a shift in the transition temperature, more astonishing effects can be observed for short chained phosphatidylglycerols. One example is the saturated glyerophospholipid

1,2-dimyristoyl -sn -glycero -3 -phosphatidyl-sn-1'-glycerol (DMPG, systematic name: 1,2-ditetradecanoyl -sn -glycero -3-phospho-1'-rac-glycerol) as shown in Figure 1.4 Panel A. Observed with bare eyes DMPG dispersions show some unique features. In a certain temperature range at low ionic strength the dispersion becomes transparent and viscous (Figure 1.4 Panel B). Calorimetric experiments revealed a correlation between the phase transition and the observed effects on optical and viscous properties as shown in Figure 1.5 on the left. This effect is accompanied by an increased conductivity [22]. A number of theories are discussed in literature to explain this findings and unravel the underlying driving forces. It was speculated that vesicles disaggregate in the transition region [22] and a connected bilayer phase, similar to a sponge phase was proposed [23].

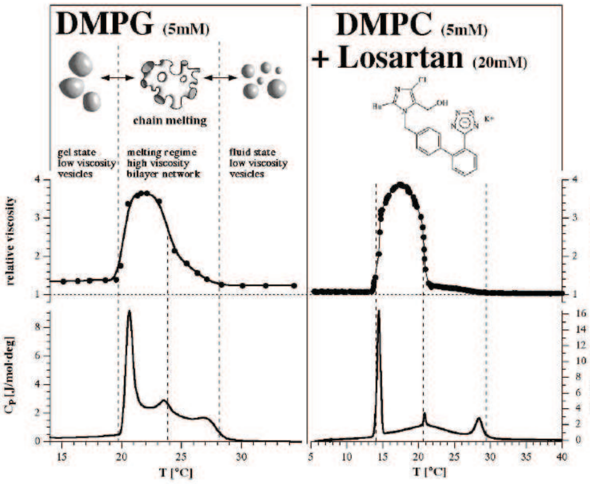

Figure 1.5: (left) Heat capacity profile of DMPG dispersion at low ionic strength (20 mM NaCl). The increase in viscosity coincide with the complex melting behaviour. (right) Heat capacity and viscosity profile of analog experiment with DMPC adding Losartan, showing a similar behaviour as the pure DMPG dispersion. (From [24])

In recent years a model assuming a perforated lamellae was proposed, trying to explain the transparency of dispersions in the phase transition by visible light passing through the holes without any scattering event or with the rims of the holes functioning as scattering centers [25] [26]. Reviewing the available literature early calorimetric experiments and freeze-fracture electron microscopy were published by Epand *et al.* [27]. The study compared the influence of salt on the phase transition of DMPG, dimyristoylphosphatidylserine (DMPS) and dimyristoylphosphatidic acid (DMPA). At high ionic strength (0.5 M NaCl) all three lipids show a cooperative melting, that changes at low ionic strength for DMPG and DMPS. Whereas the ionic strength does not seem to have an influence on DMPA dispersions, the properties of DMPG dispersions changes, suggesting the formation of a hydrophilic surface with high curvature. A more detailed calorimetric study on the influence of salt on the transition of 1'-DMPG and the corresponding sn-3' stereoisomer was performed [28], showing a shift of the transition peak towards higher temperatures with increasing the salt concentrations. Use of light scattering and electron spin resonance (ESR) spectroscopy, together with measurements of the conductivity and the refractive index, revealed a different charge states on the surface of the bilayer and different molecular weights for the particles in and outside of the transition [22]. These changes were explained by vesicle disaggregation upon entering the phase transition and re-aggregation at the end of the transition. Results from x-ray scattering studies suggested the existence of an intermediate phase exists, between the onset and offset of the phase transition [29]. The observed decrease in scattering intensity in the intermediate phase is explained by the authors as interference of scattering units. It is as likely that the contrast between the bilayer and the surrounding medium decreases, e.g. due to swelling of the membrane. A study focussing on the concentration-dependent phenomena was published one year later. As a main result it was stated that the existance of the intermediate phase seems to depend on the concentration of lipid [30]. With lowering the lipid concentration the onset of the phase transition is shifted towards lower temperatures. The shape of the curve remains, until the concentration of DMPG drops below a concentration of 0.5 mM, leading to a narrowing of the transition region and an increase of the transition temperature. For 0.01 mM the main transition peak is shifted towards a temperature over 40 ° C. Following this study new ESR, light and x-ray scattering experiments were performed, excluding vesicle fusion in the course of the transition [31]. Lately a perforation on a mesoscopic scale was suggested, allowing visible light to pass through the defects. This model should explain the viscous and optical properties of the lipid in the intermediate phase [25]. Alakoskela et al. excluded the formation of a network and dense aggregates [32], supporting the formation of a perforated lamellae in a recent publication [33].

The plausibility of all models and the comparability of the results will be reconsidered in the results and the discussion section.

1.4 Interaction of membrane active-compounds with model membrane systems

Apart from studying pure lipid dispersions interesting charge-driven effects can be observed upon the interaction of membrane-active compounds with model systems.

1.4.1 Membrane-active compounds

As diverse as the chemical composition of structural lipids is the number of compounds interacting with the membrane in a specific or unspecific fashion, examples are drugs and peptides [34]. Quite common are studies on pore-forming peptides with antimicrobial or tranfection activity or natural compounds as the honey bee venom mellitin [35], magainin, a peptide found in the skin of the frog *Xenopus laevis* [36] or alamethicin [37] a peptide produced by the fungus *Trichoderma viride*. Less pronounced effects on the bilayer level are observed for a class of drugs called sartans. An example is the compound Losartan upon interaction with zwitterionic lipids. At high drug concentrations the anionic drug with 1,2-dimyristoyl-sn-glycero-3-phosphocholine (systematic name: 1,2-ditetradecanoyl-sn-glycero-3-phosphocholine, DMPC) dispersions the calorimetric profiles and viscous behaviour similar to the one of DMPG at low ionic strength, as shown in Figure 1.5 [24]. Losartan is an antagonist for the peptide hormone Angiotensin II (Ang II), the key player of the Renin-Angiotensin-System (RAS).

1.4.2 Renin-Angiotensin systeme

The renin-angiotensin system plays a critical role in circulatory homeostasis. Part of this system is the peptide hormon Angiotensin II (Ang II), a potent vasoconstrictor that aids in the blood pressure regulation, as well as in body fluid balance maintenance. Ang II derives from the precursor angiotensinogen, through enzymatic reaction catalyzed by renin and the angiotensin converting enzyme (ACE). On the heart, acting in both endocrine and paracrine fashions Ang II regulates contractility, remodelling, growth, apoptosis, and reduces cell coupling and conduction velocity in cardiac muscles. Ang II has two major receptor subtypes, the Ang II type 1 receptor (AT_1-receptor) and the Ang II type 2 receptor (AT_2-receptor). Although both types of receptors were found in cardiac muscle cells, only AT1-receptor was found to mediate classical cardiovascular functions like blood pressure elevation, vasoconstriction, aldosterone release and renal absorption of water and sodium. From a patho-physiological point of view, like in renal diseases or hypertension, changes in the renin angiotensin system occurred. Hypertension can be treated by β-blockers, inhibiting the conversion of angiotensinogen to angiotension I, or by specific inhibition of the AT_1-receptor by an Ang II antagonist like Losartan and its active derivate E-3174. By selectively blocking the Ang II binding site on the AT_1-receptor the vasoconstrictor and aldosterone-secreting effects are inhibited, leading to a decrease in the blood pressure, the sodium retension and the stroke volume.

1.4.3 Angiotensin II, Losartan and E-3174

The drug Losartan, available as COZAAR ® containing Losartan potassium, is a reversible, competitive antagonist at the AT_1-receptor, administered orally to people suffering from hypertension. Losartan is a 4-chloro-5-hydroxymethylimidazole derivate metabolized in rats, monkeys and humans. More potent than Losartan itself is the carboxylic acid derivate E-3174 inhibiting the AT_1-receptor in a reversible non-competitive manner. *In vivo* the conversion of Losartan to E-3179 and finally E-3174 is catalyzed by cytochrome P_{450} enzymes,

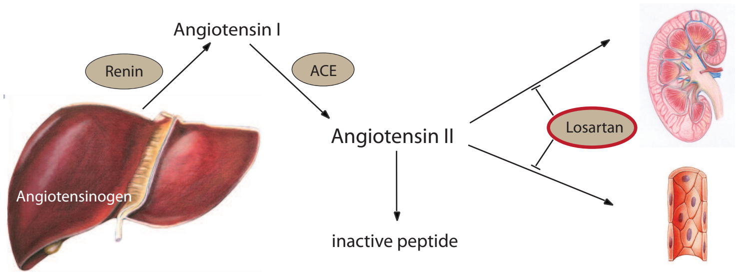

Figure 1.6: Ang II derives as a precursor (angiotensinogen) from the liver and gets cleaved by the proteases Renin and the Angiotensin converting enzyme (ACE) into its active form Ang II. The peptide hormone acts on receptors in the kidney and in blood vessels. Losartan is a potent Ang II antagonist, inhibiting its blood-regulating function.

requiring NADPH and molecular oxgen (Figure 1.7) [38]. Apart from binding to the membrane protein receptors AT_1 and AT_2 the three compounds Ang II, Losartan and E-3174 are interacting with model membranes. Theodoropoulou et al. studied the molecular basis of the interaction of Losartan with membranes, using DSC and ESR [39]. For DMPC dispersion mimicking the cell membrane, they observed, with increased concentration of Losartan, a thermodynamic behavior typical for the analog charged lipid DMPG. Ang II also adopts a well-defined structure in a phospholipid environment, as studied by Carpenter et al. using NMR [40].

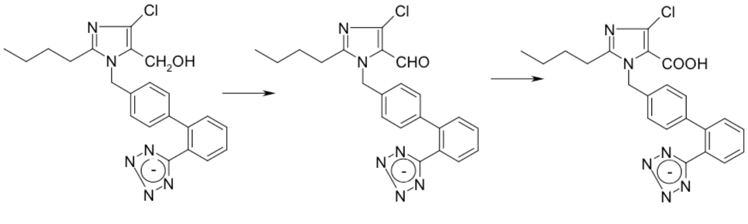

Losartan E-3179 E-3174

Figure 1.7: Transformation of Losartan to E-3174. *In vivo* this reaction is catalysed by cytochrome P_{450} enzymes.

For E-3174 the interaction with DPPC, as studied with DSC, is similar to the one observed with Losartan [41], even thought the broadening and the shift of the transition peak is occuring at lower concentrations of the compound. A plausible mechanism of action is the insertion and diffusion of Losartan and E-3174 respectively through membrane bilayers and the adjacent diffusion and docking into the AT_1-receptor [41].

1.5 Motivation and thesis outline

Dealing with model membranes means dealing with soft condensed matter, characterized by its weak intermolecular energies. One can imagine that small changes in the hydration and the hydrophic environment, the molecular shape and size, the van der Waals and electrostatic interaction as well as cooperative and entropic effects, can have a major impact on this systems.

Considering short-chain phospholipids like DMPG the high charge density on the surface is leading to the described quite unusual effects. By comparing now this charged lipid system under variation of ionic strength, pH and the influence of shear with an analog zwitterionic lipid, the changes, especially in the structure, and the underlying driving forces should be elucidated. This is important as the majority of literature provides information about zwitterionic systems, reflecting the urgent need for a better understanding of charged systems. Method-wise this challenge will be addressed by studying DMPG dispersions under various conditions, using a number of scattering techniques with focus on small angle neutron scattering (SANS).

Of course, a number of theories about the structural changes occurring in DMPG dispersions at low ionic strength exist. The main drawback comparing the available results is lying in the diversity of sample compositions and treatments, together with the influence arising from some experimental techniques itself, the use of labels and data interpretation. This obstacle will be met by a consistent sample preparation, allowing to perform the majority of experiments with a standard sample, preferring experimental techniques not requiring the use of external labels or a sample preparation that is having a strong influence on the sample. The collected results will be discussed with respect to the current theories, trying to evolve a new comprehensive model about the structural changes and the associated driving forces.

A second way to study the effect of charge on model membranes is revealing the impact of membrane-acitve compounds. Choosing substances with different number and types of charges it is crucial to understand how this interaction is occurying on a molecular level, if it is depending on the concentration of the individual compound and if the effect is changing by changing the phase state of the lipids. Studying the interaction of Losartan, E-3174 and Ang II with model membranes it is interesting to elucidate the interaction of the compounds with the membrane and to understand the different binding mechanisms. For this particular set of substances, the results will be compared to *in vivo* studies, trying to explain their different biological function.

In the next chapter the theory for scattering at a lattice and from independent particles will be established, pointing out the advantages using neutrons over x-rays and light scattering to derive structural information about vesicles and the local structure of the bilayer. In Chapter 3 the used materials, buffers and sample preparations are listed, followed by a description of the used methods. Results of the experiments are split in two chapters, Chapter 4 for studies on DMPG and Chapter 5 for studies on membrane-active compounds. In the following chapters a general conclusion and finally an outlook is given. Suppliers for chemicals, the background of the data fitting are given in the Appendices.

Chapter 2

Theory

Different scattering and diffraction techniques can be applied to study membrane models and their interaction with membrane-active compounds. To understand the experimental strategy and the to be able to interpret the data, necessary theory is introduced in this chapter, grouped into diffraction from three-dimensional periodic structure and independent particle scattering recorded at small scattering angles.

This chapter is not aiming for a mathematically complete description of the relevant theory, but an impression about the background and the necessary assumptions and generalizations, giving an impression about the shape and structural changes of the particles that can be addressed.

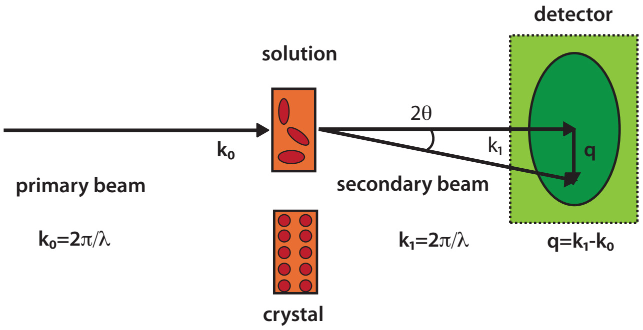

Figure 2.1: Schematic representation of a scattering or diffraction experiment (adopted from [42]). Depending on the sample, whether it is a solution or a crystal, scattering or diffraction can be observed.

In the most simplest way the setup of a scattering or diffraction experiment can be imagined as sketched in Figure 2.1. An incident or primary beam is approaching a sample and parts of the beam are interacting with the atoms in the sample. For such a setup the scattering vector q can be defined as

$$q = 2|\mathbf{k_0}|sin\theta = \frac{4\pi}{\lambda}sin\theta \tag{2.0.1}$$

with $k_0 = |\mathbf{k}_0|$ the wavevector of a monochromatic plane wave illuminating the object. In the case of elastic scattering k_0 is equal to the wavevector of the scattered wave k_1. For every position on the detector and the according scattering vector q an intensity is measured. The pattern recorded on the detector is depending on the type of sample. In case of ordered atoms or molecules, like in a crystal diffraction occurs, resulting in distinct reflections on the detector. For a random oriented set of atoms or molecules scattering occurs, reflected by a rather uniform scattering intensity distribution.

2.1 Scattering from independent particles

The modern theory of solution scattering is based on the work of Zernike and Prins [43] using the Fourier integral theorem to calculate the radial distribution function of molecules around each individual molecule from the collected diffraction pattern. Since then the theory was further developed with respect to solution scattering from polymers and biological macromolecules as published by Glatter, Svergun, Koch [44][42][45].

Here the initial relation of Zernike and Prins will be derived starting from the vector representation of a solution scattering experiment as sketched in Figure 2.1. To be able to interpret the data and understand the experimental strategy for SAS experiments of biological systems the concept of contrast variation, the Guinier approximation and the distance distribution function are introduced.

2.1.1 Small angle scattering of isotropic systems

Assuming the same experimental setup as used for introducing the diffraction theory, sketched in 2.1 and the same definition of the scattering vector q the amplitude of a wave scattered by each atom is described by its scattering length, f.
For hard x-rays interacting with electrons the atomic scattering length is $f_x = N_e\, r_0$ where N_e is the number of electrons and $r_0 = 2.82 \cdot 10^{-13}$ cm is the Thomson radius. The atomic scattering length does not depend on the wavelength unless the photon energy is close to the absorption edge of the atom. Neutrons interact with the nuclear potential and with the spin and the neutron scattering length consists of two terms $f_n = f_p + f_s$. The last term bears structural information only if the neutron spins in the incident beam and the nuclear spins in the object are oriented [46], otherwise the spin scattering yields only a flat incoherent background [42].

For a system of N identical particles with a scattering length f(q) the intensity can be written as

$$I(q) = \sum_{i=1}^{N}\sum_{j=1}^{N} f_i(q)\ f_j\ (q)\ exp\ [i\ q(\mathbf{r}_i - \mathbf{r}_j)] \tag{2.1.2}$$

r_i and r_j are the particle coordinates.

Separating the terms with i=j and averaging over all particles gives

$$\langle I(q)\rangle = \left\langle \sum_{i=1}^{N} f_i^2(q) \right\rangle + \left\langle \sum_{i\neq j}\sum_{i\neq j} f_i(q) f_j(q)\ cos(q\ \mathbf{r}_{ij}) \right\rangle \tag{2.1.3}$$

$$= \bar{N}\left\langle f^2(q)\right\rangle + \langle f(q)\rangle^2 \left\langle \sum_{i\neq j}\sum_{i\neq j} cos(q\ \mathbf{r}_{ij}) \right\rangle \tag{2.1.4}$$

$\langle\ \rangle$ indicate the spherical average, $\mathbf{r}_{ij} = \mid \mathbf{r}_i - \mathbf{r}_j \mid$. $\bar{N}$, the mean value of N is used, as the number of the scattering centers is fluctuating. To be able to calculate the mean value of the sum in equation 2.1.3 the introduction of a probability function is helpful. p_{ij} is the probability to find a particle in the volume dv_i pointing along the vector $\mathbf{r}_i$ and simultanously a particle in dv_j, pointing along the vector $\mathbf{r}_j$. Averaging $cos(q\ \mathbf{r})$ over all orientations gives

$$\langle cos(q\ \mathbf{r})\rangle = \int_0^{\pi} cos\ [q\ r\ cos(\varphi)]\frac{sin(\varphi)}{2}d\varphi = \frac{sin(q\ r)}{qr} \tag{2.1.5}$$

φ is the angle between the vectors $\mathbf{q}$ and $\mathbf{r}$, while $sin(\varphi)\ d\varphi/2$ represents the probability of the angle lying inside the interval $(\varphi, \varphi + d\varphi)$. This leads to

$$\left\langle \sum_{i\neq j}\sum_{i\neq j} cos(q\ \mathbf{r}_{ij}) \right\rangle = \int\int_{V_0} \frac{sin(qr_{ij})}{qr_{ij}} p_{ij}\ dv_i\ dv_j \tag{2.1.6}$$

with V_0 the irradiated volume of the sample.

Using the normalized function

$$P(r) = P_{ij} = \frac{p_{ij}}{v_1^2} \tag{2.1.7}$$

instead of p_{ij}, with $v_1 = V_0/\bar{N}$ as the mean volume per particle.

By substituting $P(r) = 1 - [1 - P(r)]$ one can write

$$\begin{aligned}\langle I(q)\rangle = \bar{N}\left\langle f^2(q)\right\rangle + \langle f(q)\rangle^2 \int\int_{V_0} \frac{sin(q\ \mathbf{r}_{ij})}{q\ \mathbf{r}_{ij}}\frac{dv_i}{v_1}\frac{dv_j}{v_1} \\ - \langle f(q)\rangle^2 \int\int_{V_0} [1 - P(\mathbf{r}_{ij}]\frac{sin(q\ \mathbf{r}_{ij})}{q\ \mathbf{r}_{ij}}\frac{dv_i}{v_1}\frac{dv_j}{v_1}\end{aligned} \tag{2.1.8}$$

The first integrals on the right corresponds to the scattering of a particle with volume V_0 and constant density. This term is negligible for scattering vectors with $q > 2\pi/D_0$ with $D_0 \approx V^{1/3}$ as it can not be determined experimentally due to the presence of the direct beam [47]. In case of the normalization of $P(\mathbf{r}_{ij})$ this function tends towards unity and r_{ij} towards infinity, hence on can write for the second integral

$$\begin{aligned}&\int_{V_0} \frac{dv_j}{v_1} \int_{V_0} [1 - P(\mathbf{r}_{ij})] \frac{sin(q\ \mathbf{r}_{ij})}{q\ \mathbf{r}_{ij}} \frac{dv_i}{v_1} \\ &\approx \bar{N} \int_0^\infty [1 - P(\mathbf{r})] \frac{sin(q\ \mathbf{r})}{q\ \mathbf{r}} \frac{4\pi r^2}{v_1} dr\end{aligned} \tag{2.1.9}$$

with the first integral equal to $V_0 v_1$ and spherical coordinates are used in the second one. For all scattering vectors $q > 2\pi/D_0$ the scattering intensity is then

$$I(q) = \bar{N} \left\{ \left\langle f^2(q) \right\rangle - \frac{\langle f(q) \rangle^2}{v_1} \int_0^\infty [1 - P(\mathbf{r})] \frac{sin(q\mathbf{r})}{q\mathbf{r}} 4\pi r^2 dr \right\} \tag{2.1.10}$$

For a spherical symmetric scattering amplitude it can be assumend that $\left\langle f^2(q) \right\rangle = \langle f(q) \rangle^2$ and the scattering intensity can be rewritten as

$$\langle I(q) \rangle = \bar{N} \left\langle F^2(q) \right\rangle \left\{ 1 - \frac{1}{v_1} \int_0^\infty [1 - P(r)] \frac{sin\ qr}{qr}\ 4\pi r^2 dr \right\} \tag{2.1.11}$$

This equation derived by Zernike and Prins [43] gives the averaged scattering intensity of the system (I(q)) and of the particle (F^2(q)). The second part of the equation depends on the statistical distribution P(r) and the volume v_1 per particle. In the case of concentrated systems and interparticle interference P(r) is also dependent on v_1 and using P(r,v_1) equation 2.1.11 can be rephrased to

$$\langle I(q) \rangle = \bar{N} \left\langle F^2(q) \right\rangle - \langle F(q) \rangle^2 \frac{\bar{N}^2}{V} \int_0^\infty [1 - P(r, v_1)] \frac{sin\ qr}{qr}\ 4\pi r^2 dr \tag{2.1.12}$$

The first term is proportional to N, giving the independent scattering from the particles, called the form factor and the second, proportional to N^2, reflects the interference of particles and is referred to as structure factor. A more simple representation of equation 2.1.12 is often found in literature, written as

$$I(q) \propto F(q)(S(q))^2 \tag{2.1.13}$$

with F the form factor (FF) and S the structure factor (SF).

One should bare in mind that this equation only holds for spherical, monodisperse particles or lamellae. Within certain limits it can be used for polydisperse, elongated particles [48].

2.2 Monodisperse and polydisperse particles

For very dilute systems only independent particle scattering occurs. If the system only contains identical particles, it is monodisperse, the particle structure can be studied. Is the size of the particles varying, means polydisperse, it is the size distribution function that is aimed for.

2.2.1 Monodisperse particles

Considering a system of identical particles with a sample volume much greater than the volume of the particle. The scattering intensity is proportional to the number of particles, giving raise to information about the shape and the inner structure of the particle. The spherical average of the three-dimensional intensity is referred to as the Debye fromula [49]

$$I(q) = \int_V \int \rho(\mathbf{r_1})\rho(\mathbf{r_2}) \frac{sin\ (qr_{12})}{qr_{12}} d\mathbf{r}_1\ d\mathbf{r}_2 \tag{2.2.14}$$

An alternative representation of this relation is to describe the scattering intensity as the Fourier Image of the Patterson function $H(\mathbf{r})$ [50]

$$I(q) =< \int_V H(\mathbf{r})\ cos(\mathbf{qr}) d\mathbf{r} >= 4\pi \int_0^\infty \gamma(\mathbf{r}) \frac{sin\ qr}{qr}\ r^2 dr \tag{2.2.15}$$

with

$$\gamma(r) =< \rho(\mathbf{r}) \times \rho(-\mathbf{r}) >= \frac{1}{4\pi} \int_0^{4\pi} H(\mathbf{r})\ d\omega = \frac{1}{4\pi} \int_0^\infty I(s) \frac{sin\ qr}{qr}\ q^2 dq \tag{2.2.16}$$

ω is the solid angle in real space. This so called correlation function can be used get a first inside into the particle features.

One information that can be extracted from the scattering data with minimal a priori information is the radius of gyration R_g, first calculated by Gunier in 1939 [51]. To calculate it the McLaurin series

$$\frac{sin(qr)}{qr} = 1 - \frac{(qr)^2}{6} + \frac{(qr)^4}{120} - ... \tag{2.2.17}$$

is substituted in equation (2.2.15), restricted to the first two terms. (Further reading about the Taylor series and the use of the McLaurin series for functions centered at zero can be find in the book of Abramowitz and Stegun [52].)
In the vincinity of $q = 0$ this leads to

$$I(q) = I(0)\ exp\ (-q^2 R_g \frac{2}{3}) \tag{2.2.18}$$

with

$$I(0) = 4\pi \int_0^D \gamma(r)\ r^2 dr \tag{2.2.19}$$

resulting in

$$R_g^2 = \frac{\int_0^D \gamma(r)\ r^4 dr}{2 \int_0^D \gamma(r)\ r^2 dr} \tag{2.2.20}$$

To withdraw informations about the structure of the particle equation (2.2.17) must be substituted into equation (2.2.14), leading to

$$I(0) = |\int_V \rho(\mathbf{r})\ d\mathbf{r}\ |^2 \tag{2.2.21}$$

representing the squared total scattering length of the particle, then

$$R_g^2 = \frac{\int_V \int \rho(\mathbf{r_1})\rho(\mathbf{r_2})\ |\mathbf{r_1} - \mathbf{r_2}|^2\ d\mathbf{r_1} d\mathbf{r_2}}{\int_V \int \rho(\mathbf{r_1})\ \rho(\mathbf{r_1})\ d\mathbf{r_2}\ d\mathbf{r_2}} \tag{2.2.22}$$

is the square of the radius of gyration. These parameters can be evaluated by fitting a straight line to the SAS curve plotted as ln(I(q)) over q^2, called the Guinier fit. The radius of gyration R_g is given by the slope of the fitted line and this approximation is valid for $qR_g < 1$. The equivalent radius of the particle is given with

$$R_g = \sqrt{\frac{3}{5}} = 0.775\ R_{particle}. \tag{2.2.23}$$

I(0) can be determined by extrapolating to zero angle and represents the total particle scattering length. In general for comparison of data collected and to perform the Guinier fits in particular the scattering intensity needs to be determined on an absolute scale. For experiments using X-rays as source this calibration is done by using secondary standards [53] and for neutrons the incoherent scattering of water is used [54].

2.2.2 Polydisperse particles

For polydisperse systems, $\left\langle f^2(\mathbf{q})\right\rangle$ has to be considered as the average contribution of the scattering intensity of the individual particles. Assuming only negligible interactions between the particles and describing the particle by a certain effective size R

$$I(q) = \int_0^\infty i_0(qR)m^2(R)D_N(R)dR \tag{2.2.24}$$

with the form factor i_0(qR) averaged over all orientations and normalized to unity at q=0 particle scattering, m(R) connects the chosen effective size with the full scattering length of a particle, D_N(R) is a size distribution function. The invariants introduced for the monodisperse system will describe a particle in the system averaged over the distribution D_N(R). In this case the radius of gyration is given by the z-average

$$\left\langle R_g^2\right\rangle_z = \frac{\int_0^\infty R_g^2(R)m^2(R)D_N(R)dR}{\int_0^\infty m^2(r)D_N(R)dR} \tag{2.2.25}$$

For solid spheres with Rg^2 = 3 R^2 /5 and m(R)= 4 πR^3 /3 the radius of gyration is given by

$$\left\langle R_g^2\right\rangle_z = \frac{3\left\langle R^8\right\rangle}{5\left\langle R^6\right\rangle} \tag{2.2.26}$$

with

$$\left\langle R^k\right\rangle = \int_0^\infty D_N(R)R^k dR \tag{2.2.27}$$

If the form factor is known the most important the evaluation of the size distribution function is the major task. Therefore it is necessary to solve equation (2.2.25). Only in a limited number of cases it is possible to solve it analytically [55][56]. For the majority of systems numerical methods are applied [57][58].

2.3 Concept of contrast variation

The theory so far did focus on the scattering of a particle, without considering the matrix the particles are dispersed in. In the best case this matrix is featureless and does not contribute to the scattering intensity of the particle of interest.

Considering an ensemble of particles in an uniform matrix, the matrix scattering can be subtracted, yielding the excess scattering length density that is used to determine the SAS intensity

$$\rho(\mathbf{r}) = \rho_p(\mathbf{r}) - \rho_s \qquad (2.3.28)$$

with $\rho_p(\mathbf{r})$ as the particle density and ρ_s as the matrix density.

In practice, speaking about lipid dispersions and dispersed biological macromolecules one has to consider the scattering of the used solvent. Hence two data sets need to be collected, one of solvent together with the particle of interest and one with the solvent only. To isolate the scattering from the particle the data set of the pure solvent needs to be subtracted.

X-rays are interacting with the electrons surrounding each atom. The scattering of a material is depending on the electron density, hence it is scaling with the number of the electrons in the shell of the atoms. For biological samples in H_2O the abundant elements and the number of electrons are similar, specially for lipids, with a high content of hydrogens only a small contrast arises. The scattering is dominated by the scattering of the water molecules and the careful subtraction is a crucial step.

Neutrons are directly interacting with the nucleus and the scattering density is depending on the isotope. Studying protonated biological material in H_2O one is facing similar problems with SANS as with SAXS, but this problems can be overcome applying the concept of contrast variation.

2.3.1 Contrast variation in neutron scattering

For SANS the concept of contrast variation as described by Knoll and Ibel together with coworkers [59][60][61] makes use of the different coherent scattering length of deuterium and hydrogen atoms. Relevant is the excess scattering length of the particle

$$b_e = b_p - \rho_s V_p \qquad (2.3.29)$$

b_p is the total particle scattering length and V_p is the particle volume that is not accessible by the solvent and ρ_s is the matrix density, again. The particle scattering length is depending on the chemical composition of the particle and can be derived by summation of all scattering lengths for the elements with respect to the molecular formula. The coherent scattering length densities for the most abundant elements in biological material are listed in Table 2.1.

The scattering length values are determined experimentally for the individual isotopes [62]. Exchange of H against D can be achieved in different ways. The easiest scenario is to exchange the solvent from H_2O to D_2O or use a deuterated sample dispersed in H_2O, giving rise to an enhanced contrast between the molecules of interest and the solvent. Depending

Table 2.1: Values for the bound coherent scattering length of the elements abundant in the molecules studied. For neutrons the coherent scattering length b (coh b) is given in fm (= $1 \cdot 10^{-15}$ m) and for x-rays (coh xs) in barn (with 1 barn = $1 \cdot 10^{-24}$ cm^{-2}).

atom / isotope	coh b (fm)	coh xs (barn)
^{1}H	-3.7406	1.7583
^{2}H (D)	6.671	5.592
C	6.6460	5.551
N	9.36	11.01
O	5.803	4.232
Na	3.63	1.66
P	5.13	3.312
Cl	9.5770	11.5257

on the problem under investigation it can be handy to exchange only parts of the hydrogens against deuterium. This applies for studies on multi-domain and multi-subunit proteins, where only single domains and subunits can be deuterated or hydrogenated. The same principle is relevant for studying membranes, as the hydrogen isotopes in the headgroup or the tail can be exchanged. If the sample contains different chemical species, like for studying the interaction of lipid bilayers with membrane-active compounds, it is suitable to alter the contrast.

2.4 Distance distribution function

Based on equation (2.3.28) the Fourier transform of the excess scattering length density can be written as integration over the particle volume

$$A(q) = \int_V \Delta\rho(\mathbf{r}) exp(iq\mathbf{r}) d\mathbf{r}. \tag{2.4.30}$$

The amplitude A can not be measured directly, only the scattering intensity

$$I(q) = A(q)A^*(q), \tag{2.4.31}$$

which is proportional to the number of scattered photons or neutrons in a given direction q.

From equation (2.4.30) the spherical averaged particle intensity can be derived by Fourier transformation

$$I(q) = \langle A(\mathbf{q})A^*(\mathbf{q})\rangle_\Omega = \Big\langle \int_V \int_V \Delta\rho(\mathbf{r})\Delta\rho(\mathbf{r}')exp\{i\mathbf{q}(\mathbf{r}-\mathbf{r}\prime)\}d\mathbf{r}d\mathbf{r}'\Big\rangle_\Omega \tag{2.4.32}$$

Assuming

$$I(q) = 4\pi \int_0^{D_{max}} r^2\gamma(r)\frac{sinqr}{qr}dr \tag{2.4.33}$$

with

$$\gamma(r) = \Big\langle \int \Delta\rho(\mathbf{u})\Delta\rho(\mathbf{u}+\mathbf{r})d\mathbf{u}\Big\rangle_\omega \tag{2.4.34}$$

the spherical averaged autocorrelation function. This function becomes zero for distances exceeding the particle diameter $\mathrm{D_{max}}$.

$$p(r) = r^2\gamma(r) \tag{2.4.35}$$

represents the distribution of distances between volume elements inside the particle weighted by the excess density distribution. This distribution can be computed by the inverse transformation.

$$p(r) = \frac{r^2}{2\pi^2}\int_0^\infty q^2 I(q)\frac{sinqr}{qr}dr \tag{2.4.36}$$

The behaviour of the scattering intensity at very small (q $\rightarrow 0$) and very large (q $\rightarrow \infty$) of the scattering vector is related to the overall particle parameters and the particle anisometry.

2.4.1 Comparison of distance distribution function and scattering intensity

The scattering intensity I(q) and the distance distribution function p(r) contain the same information, one in real and one in reciprocal space. A visual inspection of typical scattering patterns and the corresponding distance distribution functions of geometrical bodies leads to the traces displayed in Figure 2.2. The curves are based on particles with the same maximum size. In the top panel the scattering intensities are displayed in the bottom panel the corresponding distance distribution functions are plotted.

As the distance distribution functions look more intuitive the features of the individual geometrical bodies are discussed based on them. Solid spheres (red curves) display a

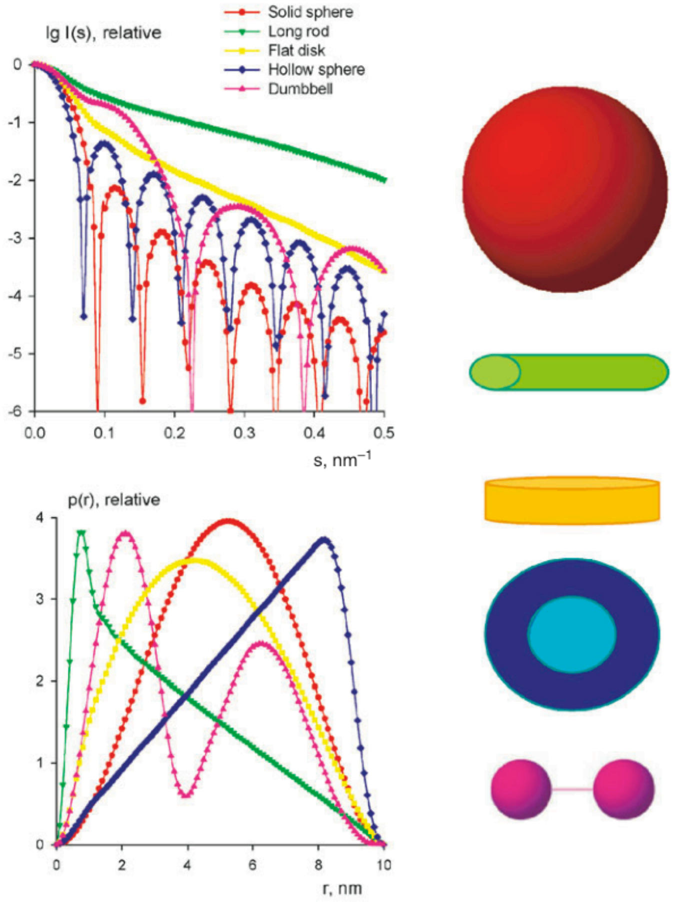

Figure 2.2: Scattering intensities and distance distribution functions of geometrical bodies (from[42]). The maximum dimension of all particles is equal, leading to one value for the maximum scattering intensity at the minimum scattering vector.

bell-shaped p(r) function with a maximum at small distances corresponding to the radius of the cross-section. Disc-like particles display a broader maximum (yellow curves), shifted to distances smaller than $D_{max}/2$. In the case of a hollow sphere, indicated in blue, the maximum gets shifted towards distances larger than $D_{max}/2$.

For asymmetrical particles, like to connected spheres (pink curves) two maxima result in the p(r) function. The first maximum corresponds to the intrasubunit distance and the second one results from the separation between the subunits. From the scattering patterns it becomes obvious that spherically symmetric objects show distinct minima. The more anisometric a particle the featureless the scattering curve and slower the decay of the scattering intensity.

2.5 Diffraction from three-dimensional lattices

The spreading out of waves passing small openings or the apparent bending of waves around small obstacles is called diffraction. Lynchpin in describing scattering from a three-dimensional lattice is the Bragg equation, initially derived from x-ray diffraction experiments on crystals by Bragg [63], [64] the equation is equally true for experiments using neutrons or electrons as sources of radiation.

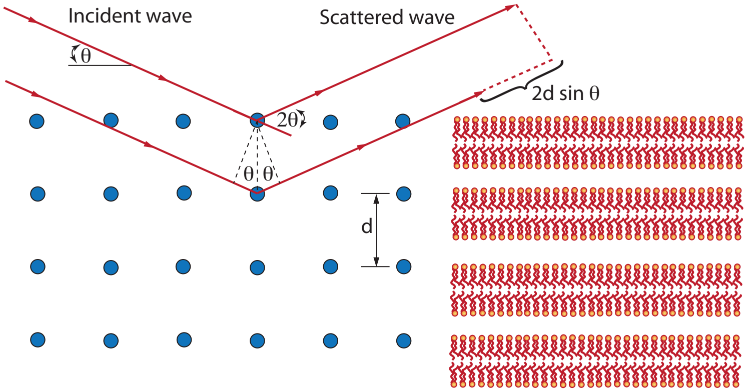

Figure 2.3: Schematic representation of Bragg scattering. To obtain constructive interference, the path difference between the two incident and the scattered waves, which is 2dsin θ, has to be a multiple of the wavelength λ. For this case, the Bragg law then gives the relation between interplanar distance d and diffraction angle θ.

In a typical diffraction experiment the incident beam is not only interacting with a single atom, but with an array of atoms aligned on a lattice. Upon interaction of the primary waves the atoms function as sources of secondary radiation with the same frequency and wavelength as the incident waves. For every possible direction of diffraction one can imagine superimposed parallel planes that reflect some of the incident waves. Each parallel plane can be assumed as a partially transparent mirror. The distance between the planes is given by Braggs law

$$d = \frac{\lambda}{2\ sin\ \theta} \tag{2.5.1}$$

d is the spacing between the reflecting planes or Bragg planes, λ is the wavelength and θ the diffraction angle as sketched in Figure 2.3. The reflected waves build the scattered or reflected beam as a result of the interference between the waves coming from various atoms. In the case of a regular spaced lattice the interference is constructive under fulfilling the Laue conditions, that can be reduced to the Bragg equation.

For a solid crystal the scattered waves interfere in a constructive fashion, if the path length is an integer multiple of the wavelength and the path difference between two scattered waves is given by $2d\ sin\theta$.

The relative position of diffraction peaks can be understand by imagining a reciprocal lattice. Every point on this lattice corresponds to a set of lattice planes in real space. The direction of the vectors in the reciprocal lattice corresponds to the normal of the lattice planes in real space. The magnitude of the vector in the reciprocal space is given in reciprocal length with respect to the real value and also reciprocal to the spacing of the lattice planes in real space. Knowing the real cystal cell parameter, the arrangement of the lattice planes and the wavelength of radiation the reciprocal lattice can be calculated. In turn, from knowing the dimensions in the reciprocal lattice, together again with the wavelength the parameters in real space can be derived. Rotating the crystal will hence not only turn the real lattice, but also the reciprocal one. This fact is used to get a hold on the scattering intensity providing information about the atomic structure of the crystal and not only about the d-spacing. A geometrical description referred to as the Ewald construction, encompassing Bragg's Law and the Laue equations is often used to derive the scattering intensity [65]. The advantage of this description, is the possibility to calculate which Bragg peaks will be measurable if the orientation of the crystal with respect to the incident beam is known. Details about the construction applied on diffraction experiments of bilayers and their interaction is given by Blaurock [66].

Chapter 3

Materials and Methods

This chapter will provide an overview about the used materials, the sample preparation and the applied methods. The materials and sample preparation section is split, treating the preparation of the DMPG samples and the sample with Ang II, Losartan and E-3174 separately. The detailed protocols for the preparation of the buffers are given in Appendix A and suppliers for chemicals are listed in Appendix B.

In the methods section the different experimental techniques and the general setups are explained. For some methods, like neutron diffraction and fluorescence microscopy special sample preparations are necessary and will be described together with the method.

3.1 Materials and sample preparation

3.1.1 DMPG samples

Crucial for the studies of the structural changes in DMPG dispersions is a consistent sample preparation making the results from different experimental techniques comparable. Especially for the scattering experiments a balance between an ideal diluted sample and enough material to be able to perform the experiments in a reasonable time must be found.
Experiments were performed at different sodium chloride concentrations and under variation of the pH. For experiments at low ionic strength a standard buffer containing 10 mM 4-(2-hydroxyethyl)-1-piperazineethanesulfonic acid (HEPES) as buffering substance and 10 mM NaCl with the pH adjusted at 7.6 was used. To see effects under variation of the ionic strength, buffers with 10 mM HEPES, 20 mM, 40 mM, 50 mM, 80 mM, 100 mM, 150 mM, 200 mM and 500 mM were prepared.
The buffers used to maintain a certain pH contained different buffering substances. For

pH 4 and 5, citric acid was used, 2-(N-morpholino)ethanesulfonic acid (MES) for pH 6 and HEPES for pH 7 and 8, 3-{[tris(hydroxymethyl)methyl]amino} propanesulfonic acid (TAPS) for pH 9 and sodium bicarbonate for pH 10 and 11. The ionic strength was changed according to the different experiments, if not stated different the salt content was 10 mM. The preparation protocols are listed in Appendix A, in Table A.1, respectively.

In general the buffers was mixed with the dry lipid powder and the dispersion was mixed thoroughly and vortexed to ensure an evenly distribution of the formed micelles and vesicles in the solution. For some experiments the dispersion was used as it is, for other unilamellar vesicles were desired. The procedure is described below.

3.1.2 Samples with Ang II, Losartan and E-3174

The three membrane-active compounds studied are, Angiotensin II (amino acid sequence: Asp-Arg-Val-Tyr-Ile-His-Pro-Phe), the drug Losartan ((2-butyl-4-chloro-1-{ [2'- (1H-tetrazol-5-yl) biphenyl-4-yl] methyl} -1H-imidazol-5-yl) methanol) and the active compound E-3174 ((2-butyl-4-chloro-1-{[2'-(1H-tetrazol-5-yl)biphenyl-4-yl]methyl} -1H-imidazol-5-yl) carboxylic acid). All compounds were used in the same molar concentration and lipid:compound ratio, to be able to directly compare the results. The substances were dissolved in a buffer containing 10 mM HEPES, 100 mM NaCl with the pH adjusted to 7.6. Depending on the experiments performed fully protonated 1,2-dimyristoyl-sn-glycero-3-phosphocholine (systematic name: 1,2-ditetradecanoyl-sn-glycero-3-phosphocholine, DMPC) or chain deuterated DMPC (1,2-dimyristoyl(d54)-sn-glycero-3-phosphocholine, d54-DMPC) was used. As described for the DMPG samples for some experiments the unprocessed dispersion is used, for others unilamellar vesicles or supported, oriented bilayer stacks are needed.

3.1.3 Sample preparation with heavy water

For the experiments using neutrons as source of radiation heavy water was used as a solvent. Important is to note in heavy water the deuterium is slightly stronger bound to the oxygen, than the proton in water and hence less self-ionization occurs. When adjusting the pH, respectively the pD of a buffer the conversion pD = 0.929 pH meter reading + 0.42 is applied [67].

3.1.4 Unilamellar vesicle preparation

For a number of experiments unilamellar vesicles were used. Vesicles of different sizes can be produced by extrusion as described by Berger [68]. The lipid dispersion is immersed in the different buffers to the desired final concentration required for the individual experiments, leading to the spontaneous formation of multilamellar vesicles (MLVs). The temperature of the dispersion should be kept above the temperature of the phase transition and, after vortexing, unilamellar extruded vesicles were produced using an Avanti Mini Extruder (Avanti Polar Lipids, Alabaster, AL) [69] and an Isopore ^{TM} polycarbonate filter (Millipore, Billerica, MA, USA) of 0.1 μm pore size. As extruded ULVs are generally contaminated with pauci lamellar vesicles (PLVs) a small vesicle size was used to maximize the amount of ULVs [70]. The MLVs were extruded an odd number of passes to avoid contamination of the sample by large and multilamellar vesicles, which might not have passed through the filter.

3.2 Methods

3.2.1 Experiments with neutrons

A number of neutron sources is available in and outside Europe providing access to external users. A good overwiev about the existing sources and instrumentation is given in reference [71] and references therein. As the sources, guides, instruments and ancillary equipment is changed and updated regularly a general introduction to the used instruments is given and recently published descriptions of the individual setups are given. The individual instruments and sources are mentioned in the according result section.

3.2.2 Neutron sources and guides

There are two general ways to produce a neutron beam, either by using a reactor [72] or a spallation source [73][74] with a solid [75] or a liquid [76] target. Independent from the source, the neutrons are transferred from the source to the actual beam line in neutron guides, special metal multilayers, using the principle of total reflection [77][78][79][80].

3.2.3 Contrast variation

As mentioned in the theory chapter the concept of contrast variation is a strong tool making profit of the different scattering length of different isotopes, specially protons and deuterons. The concept will be used in two ways throughout the experiments described here. In the experiments with DMPG the solvent of the buffer will be exchanged from H_2O to D_2O. This will yield an enhanced contrast between the membrane and the surrounding medium.

For the experiments with the membrane-acitve compounds two strategies were followed. Similar to the experiments with DMPG protonated lipids in D_2O buffer is used.

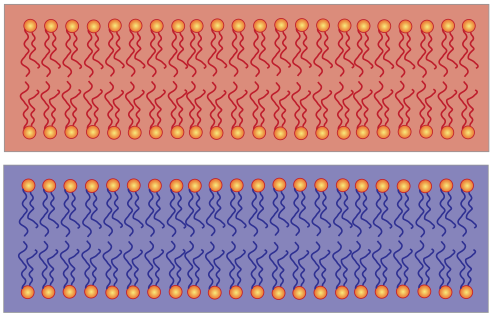

Figure 3.1: Illustration of contrast variation. By exchanging the H_2O of the buffer by D_2O or chemical groups leads to change in the contrast. left: protonated membrane in H_2O. right: lipids with deuterated acyl chains in D_2O.

Additional studies were deducted using chain-deuterated lipids in heavy water. The advantage of this approach is that only the headgroup and the interacting compounds are protonated. The membrane-active compounds in the buffer are to small to contribute to the scattering signal, except from the background. Changes in the headgroup region can be assigned to the binding of the molecule of interest.

3.2.4 Small angle neutron scattering (SANS)

SANS is a powerful technique to learn about the properties and structural changes occurring in a variety of materials, including biological samples, polymers [81], geological specimens [82], superconducters [83], carbon nanotubes [84] and samples of interest in food science [85].

Basically all biological macromolecules and the interaction among them can be studied by SANS. Single proteins and complexes [86, 42] as well as polysaccharides, like cyclodextrins [87] and their interaction are studied [88]. In the past decades a variety of studies was dealing with lipids, their phases [89, 90] and the interaction with other classes of molecules. Bacterial membranes were used as sources [91], but the majority of studies used synthetic lipids as model system [92][93][94].

Specially due to the application of the contrast variation method [60] a variety of questions can be addressed using SANS. Model membranes and lipid mesophases [90][95], the bilayer thickness and the interface area were studied [96][97], as well as the multilammelarity, structure and hydration of different lipid systems [98][99]. Of interest was the changes introduced upon mixing different lipids [59] as well as bilayer thickness responding to steorls [100] [101][102] and the resulting domains and rafts [103][104].

Most recently SANS was applied to study the influence of influence of pressure on membranes [105], to learn more about the flip-flop of lipids using time resolved SANS [106] and to get a better insight into the water distribution across curved bilayers [107]. The interaction of peptides and membranes was studied in combination with studies on cytotoxicity, like in the case of mellitin [108] and the development of new antimicrobial drugs [109][110].

3.2.5 Small angle neutron scattering - Basic setup

For small angle neutron scattering (SANS) a beam with a narrow wavelength distribution is desired, achieved with a velocity selector. This spinning turbine can be tuned allowing neutrons with the right speed, hence the desired wavelength to pass. Second criterium for good data quality, after a narrow wavelength distribution is a well collimated beam.
The collimator is a vacuum vessel in which the divergency of the neutrons is adjusted by a system of apertures and neutron guide segments.The optimum with respect to resolution and intensity is obtained if both apertures (one aperture directly in front of the sample) determining the divergency of the beam are at the same distance as the sample from detector one.
The neutrons get elasticaly scattered by the sample, commonly filled in Hellma cuvettes (Hellma, Müllheim, Germany), as used in photospectrometers. The sample holders are generally custom-made for the individual instrument, allowing to change and monitor the temperature and other parameters, like pressure, if necessary. Depending on the instrument the compartment with the sample holder can be evacuated. Neutrons scattered by the sample are entering the several meter long flight tube, another vacuum vessel and finally hit a ^{3}He-filled two-dimensional detector. The direct beam is blocked by a beam stop avoiding damage of the detector. A schematic representation of a SANS spectrometer can be found in Figure 3.2.

After readout from the detector the rawdata is corrected for the detector efficiency, radially averaged and integrated. After absolute scaling of the intensity, an absorption correction and subtraction of the background, models can be fitted to the data to get an inside into the features of the samples.

It is possible to collect data in an angular range between about 0.3 ° and 6 °, depending on used wavelength allowing to study structures from 1 nm up to several 100 nm. To achieve an optimal result in a minimum time the sample detector distance and accordingly the length of the collimator path is changed. For a short sample-detector distance, resolving the high q-vector range, more neutrons hit the detector and a good signal-to-noise ratio is achieved in a shorter time, than for a long sample-detector distance, providing the low q-vector range. The measurement time or the count rate is adjusted, making the data quality

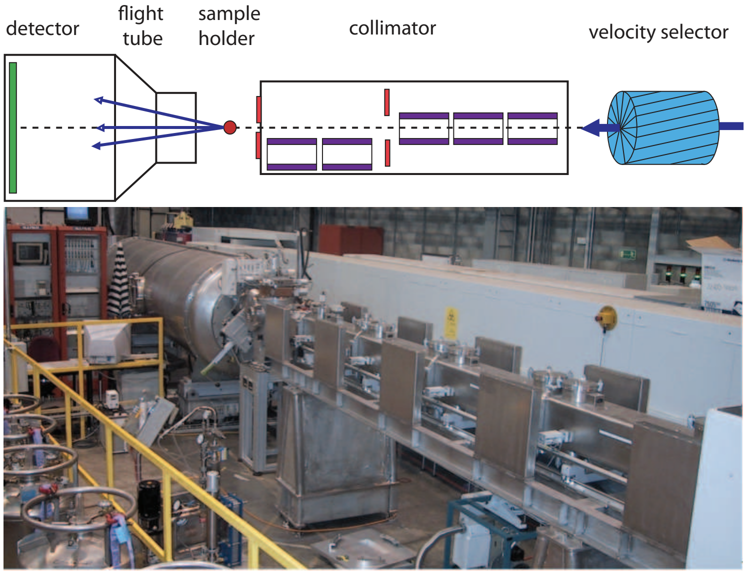

Figure 3.2: top: Schematic representation of a SANS camera. Neutrons are entering from the right, pass the velocity selector and enter the collimator. After interaction with the sample the scattered neutrons enter the flight tube and hit the detector. bottom: picture of the SANS.-II camera at PSI.

comparable for the datasets that are merging them to one data set in the end. All the initial corrections and the data reduction steps are performed using software packages provided by the beamline scientist of the individual instruments and sources. At the Geesthacht Neutron Facility (GeNF) the software package Sandra [111], at the Paul Scherrer Institute(PSI) BerSANS [112] was used. In addition self-written Matlab scripts were used to reduce the data from PSI and QtiPlot at the Jülich Center for Neutron Science (JCNS) hosted by the FRM-2.

3.2.6 Ultra small angle neutron scattering

To be able to study particles with sizes up in the μm range ultra small angle neutron scattering (USANS) can be performed. Different setups allow to collect data in the desired low q-range. One possibility is building an instrument with a Bonse-Hart geometry as described by Drews et al. [113]. It can be more convenient to use an existing SANS instrument inserting refractive lenses performing experiments at long wavelength. For the illumination of large sample volumes, with areas of about 5 mm, aspherical lenses need to be used, as explained by Frielinghaus *et al.* [114], giving the relevant background.

USANS is applied in materials research [115] to characterize substances as monolithic porous glasses [116], polyvinyl alcohols [117] and complex fluids as polymer solutions, block copolymers and surfactants.

The experiment described here was performed on the KWS-2 spectrometer at JCNS/FRM-2 using the lenses as described [114]. A sample-detector distance of 8 m was chosen and a

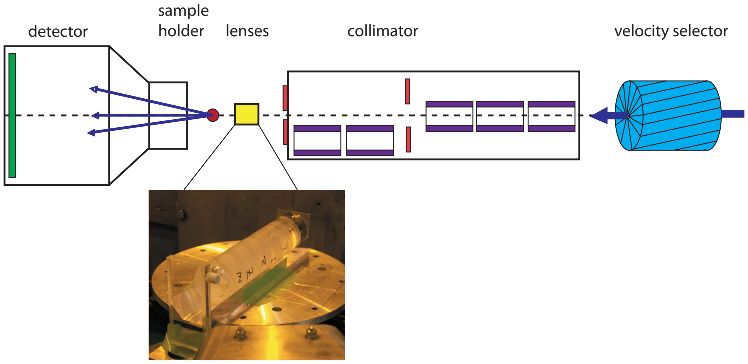

Figure 3.3: Schematic representation of a USANS setup. The layout of the SANS setup is same as described above, differing in the inserted lenses as shown in the picture.

wavelength of 11 Å . The data processing was performed as described for the data derived for the standard SANS data and used to perform a Guinier fit.

3.2.7 Rheo-SANS

Small angle measurements can be used to characterize structural changes occurring under the influence of shear, requiring a special sample environment. A number of polymers, colloids and detergents are undergoing structural transitions under the influence of shear. This includes changes from a planar lamellar structure to the formation of multilamellar vesicles [118][119], the rearrangement of immersed particles [120][121], leading to shear thinning and thickening effects, relating the macroscopic flow properties to the microscopic structure [122].

Common is the use of Couette cells, consisting of a rotating cup and a stating pendulum, leaving a gap between them, where the sample gets poured. Pendulums with different diameters allow to change the gap width and together with the rotation speed of the cup an appropriate shear can be applied on the sample. The cells are made out of materials that are rather transparent to neutrons, like sapphire or niob. To ensure a constant sample volume and concentration vapour barriers were constructed, crucial for the reproducibility of the data [123][124].

Measurements can be performed in two configuration, in radial and in tangential mode, as sketched in Figure 3.4. Viewed from the top, in radial mode, the beam is passing the cell in the middle at the thickest point, passing the sample two times. In tangential mode the beam is passing the sample at the side of the cell. A typical distance between the cup and the and the pendulum is 1 mm, making it necessary to narrow the beam in tangential mode. Additionally the determination of the absorption is not as straight forward as in the standard SANS. The beam in tangential mode is not passing through a cubic sample volume but more with a trapezoidal shape, making it necessary to simulate the absorption [124].

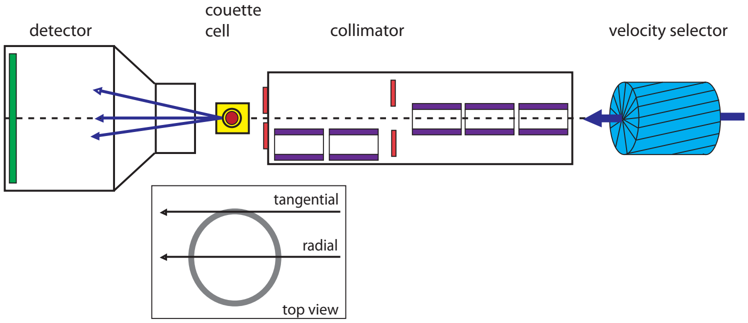

Figure 3.4: Rheo-SANS setup with a Couette cell containing the sample. This cell is containing of a rotating cup and a static pendulum. Measurements can be performed in radial and tangential mode.

3.2.8 Neutron Diffraction

As already described for SANS, a well collimated beam with a narrow wavelength distribution is essential for a good data quality. Hence the beam is passing a monochromator and in this case in addition a nitrogen cooled Beryllium filter ([125], and references therein) before passing the collimator.

The sample chamber is consisting of a goniometer holding the sample and allowing a precise adjustment. To be able to control the humidity the sample is covered by an aluminium can. At the bottom of the chamber teflon holders are placed holding the hydration buffer. After hitting the sample the scattered neutrons will be detected by an area detector. Aim of the experiment is to collect as many orders of diffraction as possible. Therefor it is necessary to change the angle between the incident and the scattered beam with respect to the sample and measure in two or three different configurations depending on the sample quality.

The sample chamber is consisting of a goniometer holding the sample and allowing a precise adjustment. To be able to control the humidity the sample is covered by an aluminium can. At the bottom of the chamber teflon holders are placed holding the hydration buffer. To control the humidity in the chamber different salts are added to the rehydration buffer.

Sample preparation

For the neutron diffraction experiments oriented bilayer stacks are used as samples. For the sample preparation two possible starting points exist. The lipids can be dissolved in organic solvent first, or the samples can be prepared from aqueous dispersions. For details see the protocol section in Appendix A.

Diffraction experiments were performed to study the interaction of Ang II with d54-DMPC. To

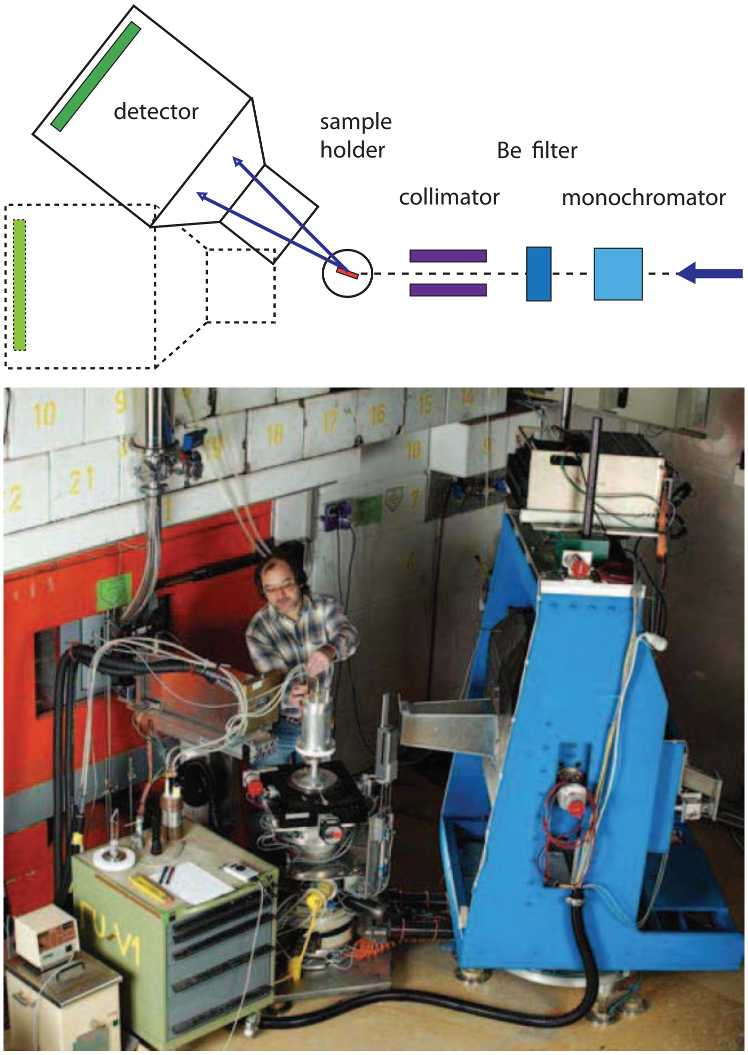

Figure 3.5: Setup of a neutron diffractometer. Similar to the setup of a SANS instrument it consists of a monochromator and a Beryllium filter for selection of the right wavelength. After passing a collimator the neutrons hit the sample, deposited on a quartz or silicium wafer and get finally recorded on an area detector. In the bottom a picture of the cold neutron diffractometer V1 at BENSC is shown.

avoid artifacts from the organic solvents, the samples were prepared starting from aqueous dispersions. 10 mg lipid was immersed in buffer (10 mM HEPES, 100 mM NaCl, pH 7.6) containing Ang II in different concentrations with final peptide to lipid ratios of 1:10 and 1:50. The resulting dispersion was sonicated at a temperature above the phase transition until the sample becomes transparent. To align the bilayers the sample was transferred to a silicium wafer and slowly dried. The alignment of the bilayers was improved by tempering the sample at a temperature above the phase transition in a vapour-saturated atmosphere over night. Prior to the measurements the wafer is transfered to the sample can. To control the humidity K_2SO_4 is added to the bottom to the chamber to allow a constant hydration of about 98%. The hydration equilibrium is reached after about six hours. Experiments are performed at different contrasts, in pure H_2O, in an equal mixture of H_2O and D_2O, and finally D_2O with 8 % H_2O. To change the contrast the hydration medium is changed to a different contrast and the sample is again incubated at least for six hours prior to the next measurement.

3.2.9 Small angle x-ray scattering (SAXS)

Small angle x-ray scattering (SAXS), similar to SANS, allows to study particles from the nm range close to atomic resolution, suitable to study proteins in solution [126][127] and derive low resolution structural information. Studying membranes SAXS is frequently applied, aiming for investigating morphological changes [128][129][130] or determining the bilayer thickness [96]. In some cases it is useful to use neutrons and x-rays as radiation and combine the complementary information yielding a more complete picture of the studied system [90][131]. One thing should be stressed here, there is a clear difference between diffraction and small angle scattering studies. The majority of SAXS studies published on membrane model systems are not SAS studies in its sheer sense, but more diffraction experiments in the small scattering angle regime. SAS studying independent particles requires an ideal diluted, isotropic sample of non-interacting particles. The requirements of the sample are often not fulfilled, demonstrated by the appearance of Bragg peaks. The SAXS experiments performed here are aiming to fulfill all the criteria of an ideal diluted sample, allowing to study only the FF, without the influence of SFs. The relevance of the difference between SAS and diffraction experiments at low angles will be further discussed in the results part.

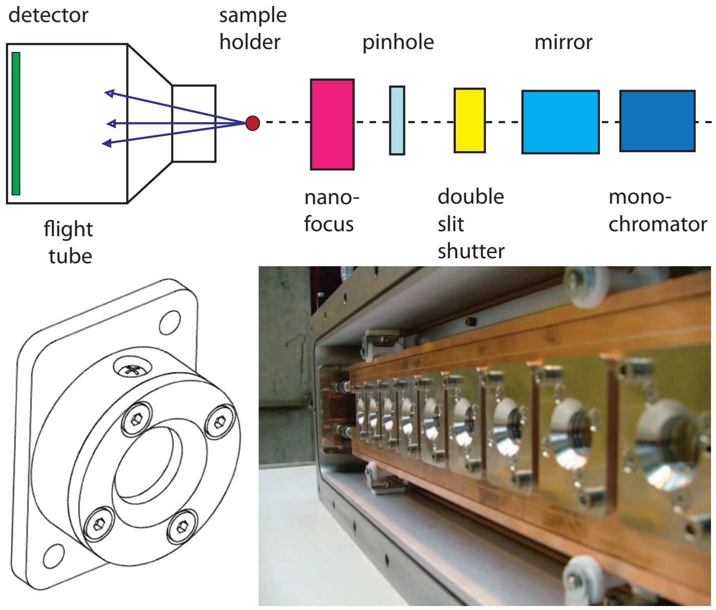

Figure 3.6: Schematic setup of a SAXS camera with the typical building blocks, a monochromator and a mirror to tune the energy, a shutter between the optical and the experimental hutch. The beam is focussed by a pinhole and a nanofocussing device before hitting the sample and entering the flight tube to finally hit the detector. A picture of the sample holder and a drawing of the used cuvettes is shown below.

Experimental setup

The data shown in the result chapters was collected on the cSAXS / X12SA beamline at the Swiss Light Source (SLS) located at the PSI. Experiments were performed short after the commissioning, facing the lack of a suitable sample environment at that time. It was necessary to find a suitable sample holder and design a set of cuvettes capable for the use at a synchrotron beamline. This obstacle was met by the use of a vacuum sample holder normally used at the SANS-1 instrument at PSI and redesigning cuvettes, using a special type of thin borosilicate glass that absorbs a minimum of x-rays.

The building parts of SAXS spectrometer are similar to the one of a SANS spectrometer, even though some differences need to be mentioned. The wavelength and the according energy is selected by a silicium monochromator and a bendable mirror, chosen to be 18 keV with an energy resolution Δ E/E less than 0.02% in the particular experiment. After passing a shutter between the optical and the experimental hutch, the beam gets focussed by a pinhole and a nanofocussing devise, adjusting the beamsize to 100 μm^2. The cuvettes with the samples were placed in a temperature controlled sample changer (MFU) used at the SANS-1 spectrometer, regulationg the temperature with an external heating circulator (F25-ME, Julabo, Seelbach, Germany) in one degree steps. After interacting with the sample the beam enters an evacuated flight tube and finally hits the Pilatus 2M pixel detector [132]. A new type of x-ray detector, using a two-dimensional hybrid pixel array operated in single-photon counting mode. Hybrid pixel that feature single photon counting, comprises a preamplifier, a comparator and a counter. The preamplifier enforces the charge generated in the sensor by the incoming x-ray. The comparator produces a digital signal if the incoming charge exceeds a predefined threshold and thus, together with the counter, one obtains a complete digital storage and read-out of the number of detected x-rays per pixel without any read-out noise or dark current.

Radiation damage is a severe problem at synchrotrons with a high photon flux [133]. Therefore it is necessary to reduce the exposure time as much as possible to ensure that a set of data, including all temperature steps, can be measured with one sample. The measurement time per temperature point was chosen with 100 ms.

3.2.10 Static and dynamic light scattering

Light scattering from solutions is originated by the spatial and temporal fluctuations of the refractive index in the scattering medium. The intensity of scattered light depends on the wavelength of the incident light, the size and shape of the particles as well as their optical properties, and the angle of observation. Experiments can be performed in two ways, as static light scattering (SLS), varying the angle of observation and as dynamic light scattering (DLS), observing the fluctuation over time. Electromagnetic radiation, as light, directed towards a sample causes the electrons surrounding the nucleus of the different atoms to oscillate about their equilibrium position, creating an oscillating dipole. This dipole works as an antenna that re-emits radiation of the same frequency as that of the stimulating radiation, called elastic scattering as there is no loss of energy in the process. Light scattering is limited to studies on diluted systems, where only single scattering events occur. In samples where multiple scattering occurs, this problem can be overcome by cross-correlation techniques [134].

Static light scattering (SLS)

In a static light scattering experiment the intensity of the scattered light (I_s) is measured at different angles θ, with respect to the incident beam, see Figure 3.7. If the scattering particles are small compared to the wavelength of radiation the Rayleigh ratio R_θ can be determined.

$$R_\theta = \frac{I_s\, r^2}{I_0\, (1 + cos^2\theta)} \tag{3.2.1}$$

with r the distance between the scattering point and the detector, I_0 is the intensity of the primary beam and I_s the intensity of the scattered beam. For large particles, where the particle dimensions equal the wavelength of the radiation the Debye scattering theory is applied.

Due to the large particle size the distance between the scattering centers has the same magnitude as the wavelength of the radiation, hence there will be interference by the waves scattered at different parts of the same particles. Accordingly in the expression for the relation between the incident and the scattered intensity an interparticle scattering term needs to be included [135]

$$R_\theta = \frac{I_s\, r^2\, P_{light}(\theta)}{I_0\, (1 + cos^2\theta)} \tag{3.2.2}$$

with $P_{light}(\theta)$ is the form factor taking into the account interferences between two scattering points on one particle. At high angles of observation the form factor depends on the nature and shape of the scattering particle. For SLS the scattering angle is converted into the scattering vector q. The equation is given below.

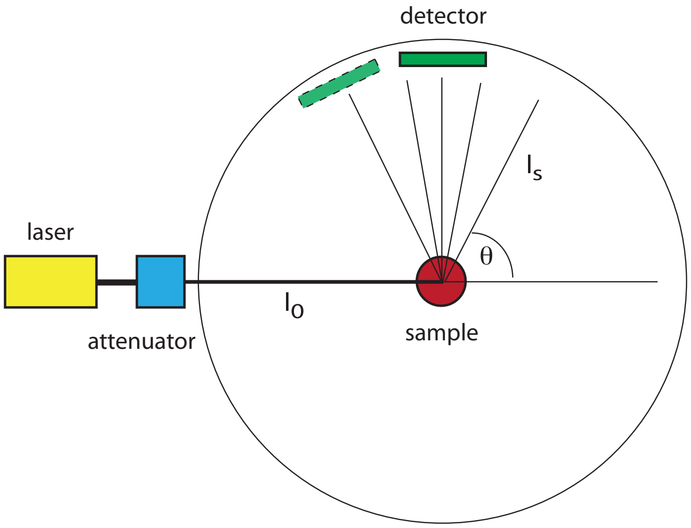

Figure 3.7: Basic setup of a light scattering devise, suitable for dynamic and static light scattering experiments. For the SLS experiments the angle of detection is varied. The DLS experiments are performed at a 90 ° angle between the incident and the scattered beam.

Dynamic light scattering (DLS)

In dynamic light scattering (DLS) measurements, the variation of the scattering intensity over time is studied, caused by the random motion of the particles in solution. This diffusion of the molecules from or to the detector, together with their oscillating electrons, generates a Doppler effect. Accordingly the observed frequency of a moving transmitting source shifts to higher or lower frequencies depending on its velocity and the direction relative to the detector [136]. As a consequence the scattered intensity fluctuates around an average value. The intensities are measured at short time intervals Δt in microseconds to milliseconds for long periods of time t, normally in the range of seconds. These experiments are repeated many times, to improve the signal to noise ratio. Based on this data the autocorrelation function can be determined [136] used to finally determine the hydrodynamic radius of the particle.

$$R_h = \frac{k_B T}{6\pi\eta\Gamma} q^2 \tag{3.2.3}$$

with

$$q = \frac{4\pi n sin(\frac{\theta}{2})}{\lambda} \tag{3.2.4}$$

n- refractive index, λ-wavelength, θ-scattering angle, k_B-Boltzmann's constant, η-solvent viscosity, Γ-average decay rate.

For non-uniform, polydisperse particles the CONTIN algorithm is used, calculating a scattering curve based on the assumed distribution of the decay rates and compares the curves to the experimental data. The solutions given are subject to two constraints. Unreasonable solutions are rejected and the principle of parsimony, in which the simplest, smoothest and least detailed solution is less likely to be wrong [137][135][138].

Experimental setup

An ALV-5000 Multiple Tau Digital Correlator (ALV GmbH, Langen, Germany) together with a HeNe-Laser at a wavelength of 632.8 nm was used for the DLS and SLS experiments. The temperature was controlled with an external heating circulator (F25-ME, Julabo, Seelbach, Germany). For aqueous solutions a refractive index of 1.3320 and a viscosity of 0.890001 cp is assumed (1 cp = 1 centipoise = 0.001 g $cm^{-1}s^{-1}$). Before the individual samples can be studied a toluene standard was measured to correct for signals caused by the instrumental setup and impurities in the sample chamber. For the DLS experiments at an angle of 90 ° between incident and scattered beam was used. Data from SLS experiments were measured in the angular range between 25 ° and 140 ° with step width of down to 0.1 ° between the individual data points.

3.2.11 Differential Scanning Calorimetry (DSC)

Differential scanning calorimetry (DSC) is a versatile tool in life science allowing to study the thermotropic properties of a variety of materials and model systems [139]. For biological molecules the samples cover proteins, lipids, DNA and RNA showing their interaction with each other and with small molecules, functioning as ligands. Especially for the study of membrane properties and changes calorimetric techniques are a vital tool [140]. A number of studies are published for pure lipid dispersion, binary and ternary mixtures or extracts of biological membranes [141][142][143][144]. DSC is also applied to study drug-lipid interactions as shown for vinorelbine [145], malatonin [146] and the calcium-dependent antibiotic daptomycin [147]. The main work performed with peptide-lipid interaction focusses on synthetic peptides and peptides with antimicrobial properties, examples are aurein, citropin and maculatin [148], maganin [36], PGLa [149] and other cell penetrating peptides [35].

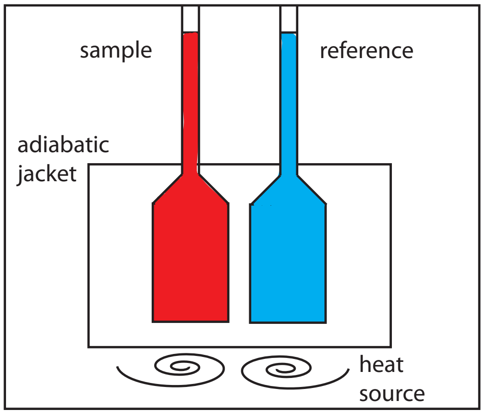

Figure 3.8: A DSC consists of a sample and reference chamber in an adiabatic jacket. The cells can be heated or cooled keeping the temperature difference between the cells zero.

All measurement were performed on a high sensitivity differential scanning calorimeter (Microcal VP-DSC, Northampton, MA, USA), with a cell volume of 0.51 ml [150]. The instrument consist of two cells surrounded by an adiabatic jacket. One cell is filled with the sample and the other cell with the reference, which is either water or the buffer used for the sample preparation. The temperature of the cells is changed with a constant scan rate, keeping the temperature difference between the two cells equal to zero. Process absorbing or releasing heat, require a different power to heat or cool the two cells. The method relies on measuring the power necessary to establish the same temperature between the sample and the reference chamber, heated or cooled with the same rate. Focussing on a short time interval Δ t one gets for the heat difference Δ Q

$$\Delta Q = \int_{t}^{t+\Delta t} \Delta P \; dt \approx \Delta P \Delta t \tag{3.2.5}$$

that can be used to determine the heat capacity c_p and finally the change in enthalpy H

$$\left(\frac{dH}{dT}\right)_p = \Delta c_p = \left(\frac{\partial Q}{\partial T}\right)_p \approx \frac{\Delta Q}{\Delta T} \approx \frac{\Delta P}{\frac{\Delta T}{\Delta t}} \tag{3.2.6}$$

with Δ T/ Δ t the scan rate.

For the experiments studying the phase transition in DMPG and in DMPC dispersion under the influence of Ang II, E-3174 and Losartan the reference cell was filled with pure water and a scan rate of 5 ° C/h was used. A slow scan rate is always recommended for studying cooperative transitions occurring in a narrow temperature window to avoid hysteresis effects influencing the results. Hysteresis and the reversibility of processes can be controlled by performing subsequent upscans and downscans, comparing the position of the melting peak. At least two sets of calorimetric scans were performed for each sample to test reproducibility. Data evaluation was performed using a macro running with Igor Pro (WaveMetrics Inc., Portland, USA). The raw data was normalized by the lipid concentration and the base line was substracted. The phase transition temperatures were taken at peak values of the heat capacity, c_p, and the calorimetric enthalpy Δ H was calculated by integrating the peak areas. In addition the position and area under the pre-transition peak and the upper phase boundary (UPB) was determined, where possible.

3.2.12 Rheology

The viscosity of a material, defined as its response to a shear, can be studied by rheology. The used rotational rheometer (Low Shear 30 Sinus, Contraves, Switzerland) consists of a rotating cup that is filled with the sample. For the measurement a pendulum gets lowered into the sample, giving a constant distance between the pendulum and the cup. The shear applied to the sample can be varied by choosing different pendulums, changing the gab width between the cup and the pendulum. In addition, the rotation rate of the cup can be changed. Independent from the type of rheometer the shear rate is depending on the speed of the cup and the gab width and is given in Hertz (Hz, sec^{-1}). The viscosity is now detected as the degree the pendulum gets moved out of its resting position with respect to the rotation rate of the cup. Depending on the effect of shear on the sample the speed of the pendulum is changed to different degrees. Studies can be performed at different temperatures, controlled by an external water bath that is cooling and heating the sample. The recorded data is compared to data of water, yielding the relative viscosity.

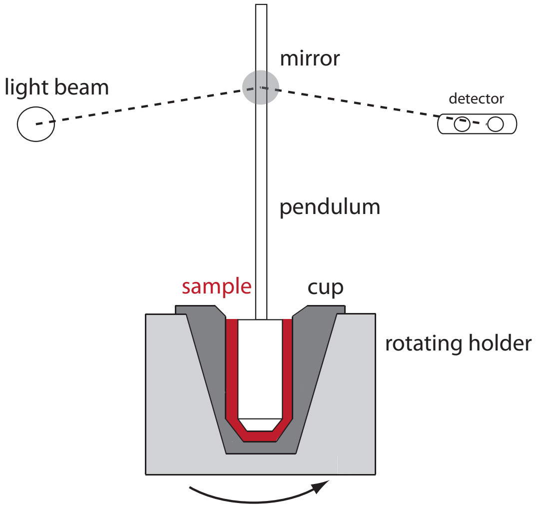

Figure 3.9: Drawing of a rheometer. The basic parts are a rotating cup and a static pendulum. Placing the pendulum in the cup leaves a gap for the sample. With rotation of the cup the pendulum gets moved out of its resting position, recorded by a detector.

3.2.13 Confocal fluorescence microscopy

Apart from the variety of scattering techniques confocal laser scanning microscopy was applied to study the structural changes in DMPG samples containing fluorescent dyes. In this type of microscopy a laser beam with a wavelength able to excite a fluorescent chromophore is focussed by an objective into a small focal volume. The focal plane can be chosen close to the surface or with a certain depth in the studied specimen. The reflected or back-scattered laser beam together with the photons emitted from the chromophores is traveling back on the same path as the incoming laser beam, passing a beamsplitter and filters. Selected wavelengths get detected by photodetection devises [151][152]. The method allows to perform an optical sectioning and a three-dimensional reconstitution of the recorded picture.

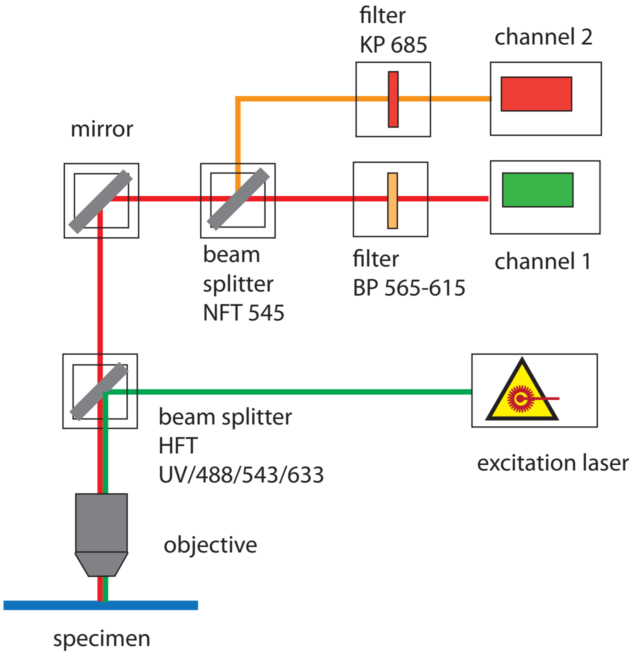

Figure 3.10: Light path of the confocal microscope, showing the building blocks of the instrument. The light from the excitation laser is passing a beam splitter and the objective hitting the specimen. Emitted fluorescent light is passing the beam splitter again, a mirror and gets detected in different channels.

Sample preparation

Different fluorescent dyes were chosen to label the DMPG vesicles. The chromophores were either bound to the headgroup, as in the case of 1,1'-dioctadecyl-3,3,3',3'-tetramethyl-indocarbocyanine perchlorate (DiI-C_{18}), N-(6-tetramethylrhodaminethiocarbamoyl) - 1,2-dihexadecanoyl-sn-glycero-3-phosphoethanolamine, triethylammonium salt (TriTC-DHPE), 1,2-dimyristoyl-sn-glycero-3-phosphoethanolamine-N- (7-nitro-2-1,3 -benzoxadiazol-4-yl) (ammonium salt) (NBD-head) or to the acyl chain as with 1-myristoyl-2- {12-[(7-nitro-2-1,3-benzo-xadiazol-4-yl) amino] lauroyl }-sn-glycero-3- [phospho-rac- (1-glycerol)] (ammonium salt) (NBD-chain). The use of different labels should minimize the likelihood that the dyes have an influence on the observed results. For all dyes a dye:lipid ratio of 1:500 was used. To ensure an equal distribution of the labels in the membrane the dyes and the lipids are dissolved in organic solvents. The solvent was evaporated under a nitrogen stream and the lipid film dried in a vacuum bell. Shortly before the experiments, the film gets hydrated with the appropriate buffer. To ensure a homogeneous mixing the sample gets thoroughly mixed and finally transferred to the sample chamber. After the experiments DSC scans were performed with the sample, to ensure that the phase behaviour is not changing, except from a shift in the transition temperature. The detailed protocol is given in Appendix A.

Experimental setup

Depending on the used dyes the laser wavelength, filters and beamsplitters need to adjusted. A scheme of the light pass with the used filters is sketched in Figure 3.10. Pictures were acquired using a LSM 510 Meta (Zeiss, Jena, Germany) using a HeNe Laser with a wavelength of 534 nm. The light is reflected at a first beam splitter (HFT UV/488/543/633) and focus on the sample by a objective with a 40 x magnification. The emitted longer wavelength light emitted by the fluorescent chromophores is passing the objective again, being transparent for this longer wavelengths. A mirror is reflecting the light before it reaches the second beam splitter (NFT 545), guiding the the fluorescent light through a band pass filter (BP 565-615) detected by channel 1. The light reflected at the second beam splitter is passing a short pass filter (KP 685) detected by channel 2 allowing to detect the scattered laser light.

Chapter 4

Structural changes in DMPG dispersions

4.1 Results

4.1.1 Differential scanning calorimetry (DSC)

Calorimetric experiments were performed to investigate the influence of pH on DMPG dispersions. The recorded traces for the pH range between 3 and 11 are shown in Figure 4.1. On the left the complete traces are shown, on the right a cutout of the lower half of the left figure is shown. All samples were prepared with the same amount of lipid (5 mM) and 10 mM NaCl in the buffer. Peaks are shifted horizontally for better visibility. Especially in the left panel the complex melting behaviour is evident. Traces recorded between pH 6 and 11 show a similar melting behaviour. A pre-transition peak is present for pH 1 down to pH 8 at around 7 ° C. The position is shifted upon lowering the pH from 10 ° C, to 11 ° C and finally 16 ° C for pH 7 to 5. For the two lowest pHs no pre-transition is recorded at all. The variation of the pH is also having an impact on the main transition. Focussing on the experiments performed at high pH, between 11 and 5, the main transition peak consists of three peaks, a main peak at the onset of the transition, one small peak in the middle and one small peak directly before the offset of the peak with the heat capacity going back to the baseline level. For the low pH range (pH 3 to pH 5) the overall profile of the main transition peaks starts to change and gets shifted towards higher temperatures. Instead of the broad peak as observed for the samples with the higher pH, the peak narrows and span around 4 ° C. Data sets derived for the low pH samples were hard to reproduce. Upscans and subsequent downscans didn't reveal the same profile. The first upscan is shown here.

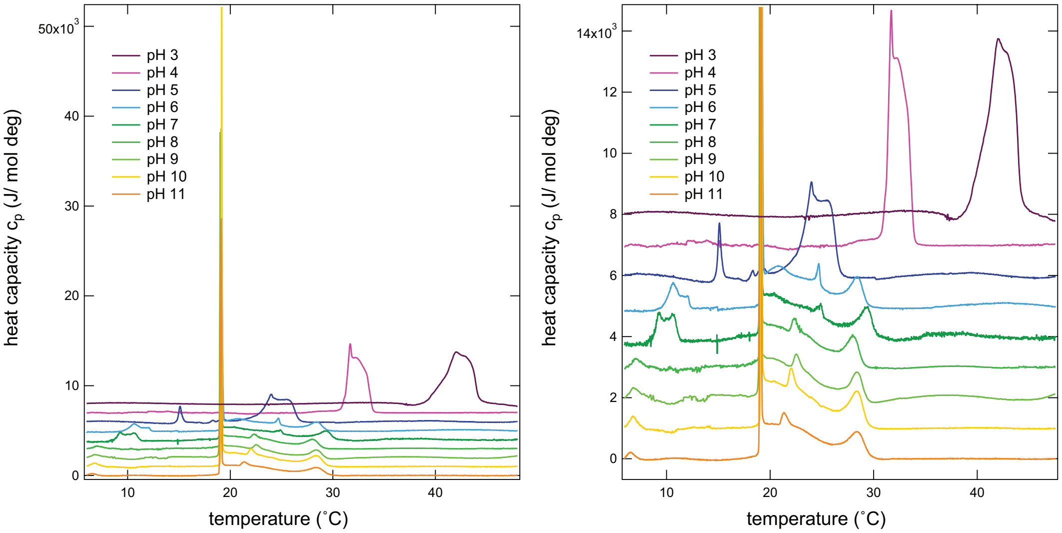

Figure 4.1: (left) DSC thermograms of DMPG samples performed in a pH range of 3 to 11. (right) cutout of the lower half of the left panel. All traces are shifted for better visibility.

The DSC experiments were performed to trace the influence of charge on the transition. Approaching the value of the dissociation constant K_a, or better its common logarithm pK_a, the protonation state of the phosphoric acid is changing. For a pH larger than 6 the phosphate group is deprotonated yielding the same melting behaviour for all samples. With pH this behaviour changes and protons from the buffer associate to the charged carboxylgroup, leading to a change in the melting profile. Upon further lowering of the pH the dissociation of the headgroup from the glycerol backbone may occur, explaining the occurrence of different traces of subsequent up and down scans.

4.1.2 Rheology

Analog to the DSC experiments, rheology studies were performed under the same conditions. The pH was again varied between 3 and 11. The results are given in Figure 4.2 in the lower panel. All datasets reveal an increase in the viscosity for a certain temperature window. For samples with pH between 11 and down to 6 the onset of the increased viscosity is around 20 ° C with an offset around 26 ° C. The two samples with the lowest pH show an elevated viscosity between 26 ° C and 32 ° C for pH 4 and 38 ° C and 45 ° C for pH 3.

The particular changes in the viscosity occur in the same temperature window as the main phase transition, revealing a close correlation between the DSC and the viscous experiments, as seen in Figure 4.2 comparing the top and the bottom panel.

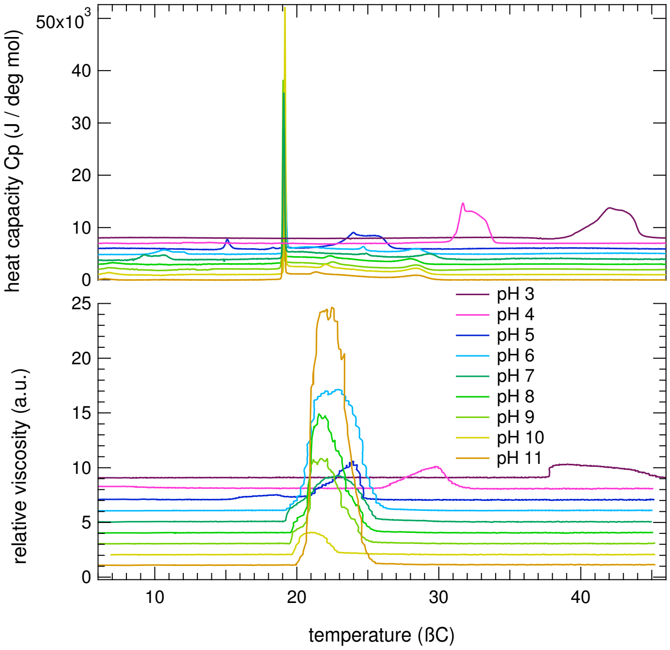

Figure 4.2: (top) DSC thermograms of DMPG dispersions at different pH values between 3 and 11. (bottom) results from the rheology measurements of the same samples as the DSC experiments. Datasets of pH 10 to 3 are shifted upwards for better visability.

The coincidence of the complex melting behaviour and the change in viscosity together with the optical changes occurring in the same temperature window suggests that the same driving forces are responsible for all effects. Changes in the viscosity and the optical properties are likely to be caused by morphological rearrangements. This hypothesis will be addressed by presenting results from light scattering experiments.

4.1.3 Dynamic and static light scattering (DLS & SLS)

A first structural characterization of the samples was performed using dynamic and static light scattering. The collected calorimetric and rheological data was used to chose the temperature points necessary to get an overview about the structural changes collecting data in the fluid and the gel phase as well as in the phase transition.

All DLS experiments were performed in one-degree steps between 15 ° C and 35 ° C. The salt concentration was varied between 10 mM and 150 mM, studying changes in the scattering intensity and the hydrodynamic radius using extruded vesicles passed through a filter with a pore size of 100 nm. The results are shown in Figure 4.3.

One first glimpse it is obvious that the hydrodynamic radius of the DMPG sample with the lowest ionic strength is on average larger compared to the samples with the higher ionic strength. The same is true for the light scattering intensity. The two curves for dispersions with 50 mM and 150 mM NaCl show a sharp decay in the scattering intensity at the temper-

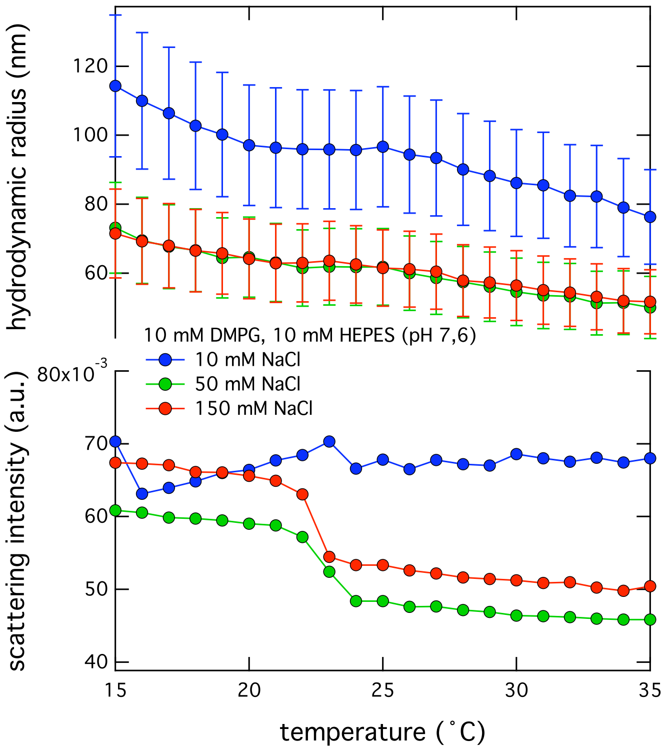

Figure 4.3: DLS data of unilamellar DMPG vesicles prepared with 10 mM, 50 mM or 150 mM NaCl. In the top panel the hydrodynamic radius is shown and the scattering intensity in the lower one, monitored over temperature. The bares are indicating the errors for the hydrodynamic radius, caused by the polydispersity of the vesicles.

ature of the phase transition. In contrast the sample with a buffer of low ionic strength shows no significant decay in the scattering intensity. The hydrodynamic radius of DMPC vesicles prepared with the same buffer as the DMPG vesicles with 10 mM NaCl appear more than 20 nm smaller, with a similar decay of the radius with increasing temperature (Figure 4.3). In general the hydrodynamic radius is decreasing with increasing temperature.

As described in the materials and methods section light scattering intensity is depending on fluctuations in the refractive index. Heating of the sample increases the thermal fluctuations and with that the fluctuations in the refractive index, as a result the vesicles appear smaller for higher temperatures. In general the calculated hydrodynamic radius is larger than the actual particle radius, as water molecules from the solvent interact with the charges on the vesicle surface, forming a hydration shell. Increasing the temperature leads to a reduction of the thickness of the hydration shell. The calculation of the hydrodynamic radius is in addition taking into account the solvent viscosity. Due to the high charge density on the surface of the DMPG more dipoles are introduced in the surrounding water molecules, leading to a thicker hydration shell contributing to the hydrodynamic radius.

If one is correcting the viscosity in the data sets for DMPG at low ionic strength, the profile for the scattering intensity and the hydrodynamic radius is changing dramatically (see Fig-

Figure 4.4: Comparison of hydrodynamic radius and scattering intensity for DMPG vesicles at low ionic strength with and without correcting for the change in viscosity. In purple the hydrodynamic radius of DMPC vesicles is plotted. The bares are indicating the errors for the hydrodynamic radius, caused by the polydispersity of the vesicles.

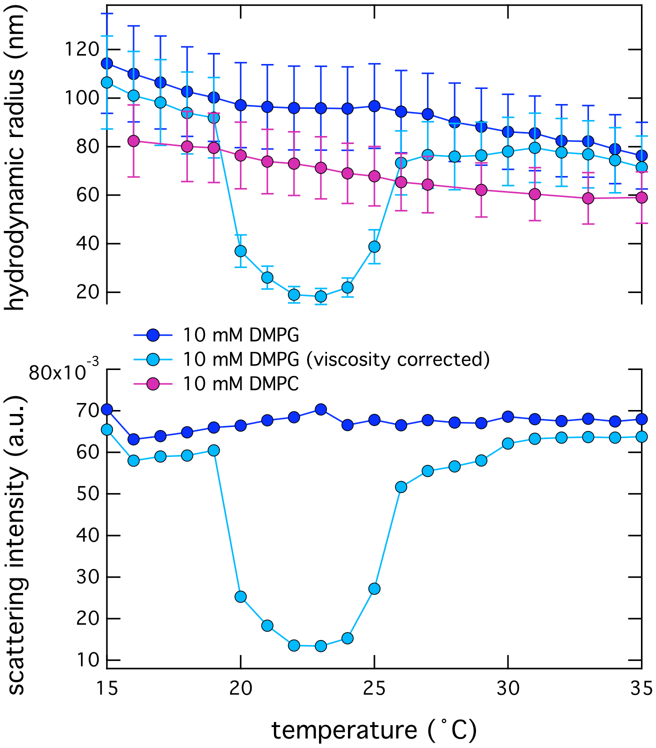

ure 4.4). For the scattering intensity a steep decrease in the scattering intensity is resulting, due to the increased viscosity in the region of the phase transition. Focussing on the new values for the hydrodynamic radius, they drop according to the scattering intensity in the phase transition region. As extruded vesicles were used a diameter of 100 nm is expected. Correcting for the change in viscosity yields much smaller diameters for the vesicles in the phase transition. The decrease in the scattering intensity after the correction of the viscosity is in good agreement with the observation made with bare eyes. The missing decay in the data before correction of the viscosity may be a result of interaction of the particles, most likely in the hydrogen bonding network surrounding the vesicles. The relevance of this finding will be discussed together with the neutron scattering results.

Static light scattering was applied to get a first idea about the structure scattering particles. At high scattering angles, in reverse a small scattering vector q, the slope of the scattering intensity decay is largely depending on the particle shape. Experiments were performed for different lipid concentrations. DMPG concentrations of 10 mM caused multiple scattering events reflected by a rather constant scattering intensity over the whole q-range. Diluted samples with a DMPG concentrations of 2 mM provided a decay in the low q-vector range with a slope close to -2 indicating as expected a hollow spherical particle (see Figure 4.5).

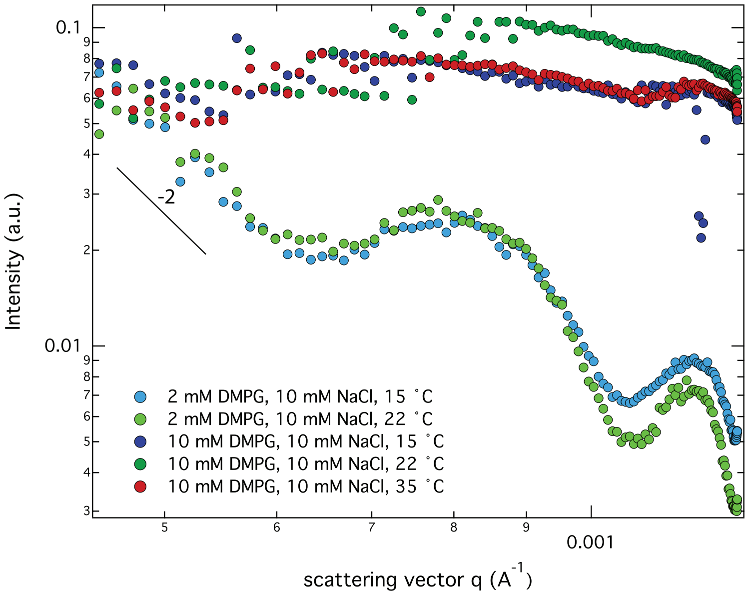

Figure 4.5: SLS results, showing the decay of the scattering intensity in dependence of the scattering vector. For DMPG concentrations of 10 mM multiple scattering was observed. Dilution to 2 mM DMPG yield information about the shape of the particle, likely to be a sphere.

Now a more detailed inspection of the morphological changes is performed, by applying small angle scattering using x-rays and neutrons.

4.1.4 Small angle x-ray scattering (SAXS)

SAXS experiments performed on the cSAXS/X12SA beamline at the Swiss Light Source aimed for a more detailed view on the integrity of the bilayer and structural changes in the overall particle shape. A constant DMPG concentration of 10 mM was used, varying the temperature between 15 ° C and 34 ° C. The NaCl concentration was varied between 10 mM and 500 mM. All samples were extruded with a filter of 100 nM pore size, yielding unilamellar vesicles. Data was collected from upscans heating the samples from 15 ° C to 34 ° C, followed by a downscan, cooling the sample down to 15 ° C, again. The high photon flux of the synchrotron, the exposure time was chosen as 150 milliseconds, to take into account the possibility of radiation damage. Prior to the data presented here studies with longer exposure times were performed and subsequently compared, to exclude relevant radiation damage.

Data collected from samples with NaCl concentrations of 10 mM, 20 mM, 40mM, 80 mM, 100 mM, 200 mM and 500 mM at temperatures of 15 ° C and 34 ° C showed a scattering decrease in the low q-range and a correlation peak between 0.2 Å $^{-1}$ and 0.9 Å $^{-1}$ (data shown in Figure 4.6 and 4.7). The width of this bilayer correlation peak corresponds to the thickness of the bilayer, the height to the contrast between the lipids and the buffer. For all studied salt concentrations, the development of the minimum at the onset of the correlation peak at 0.2 Å $^{-1}$ is depending on the phase state. In the gel phase this minimum is

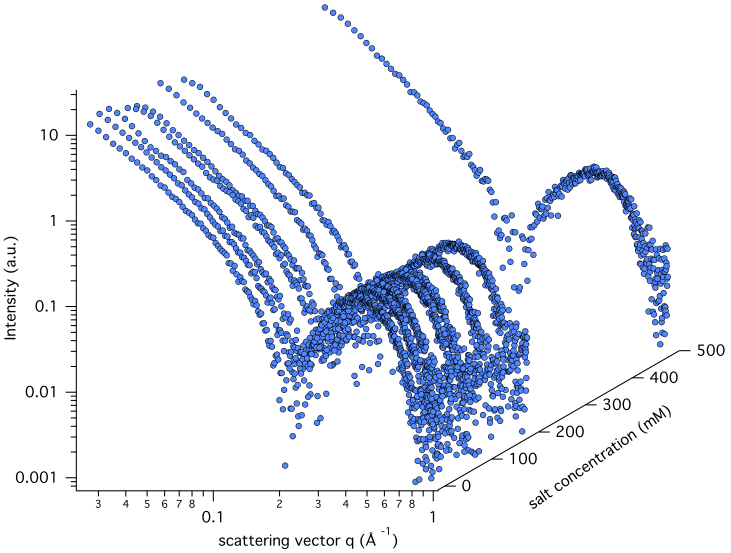

Figure 4.6: SAXS data for DMPG dispersions at 15 ° C varying the ionic strength between 10 mM and 500 mM.

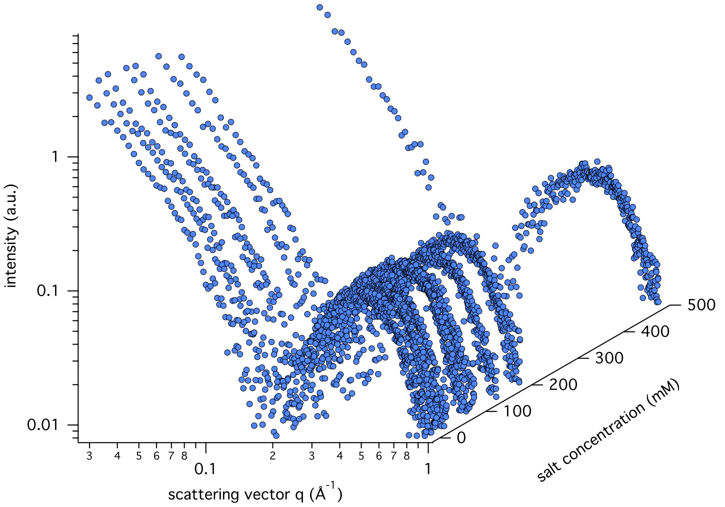

Figure 4.7: SAXS data for DMPG dispersions at 35 ° C varying the ionic strength between 10 mM and 500 mM.

less pronounced compared to the fluid phase. Interesting is now to inspect data collected for samples at the temperature of the phase transition. The low q-range is providing information about the bilayer and the shape of the particle. A slope of -2 as introduced in the theory section is corresponding to a hollow sphere, like a vesicle. Changes in the slope hence indicate a change in the shape or a change in the fluctuation range of the bilayer. The changes can be distinguished under comparison of the maximum scattering intensity at the lowest q-vector. If a change in the slope in the low q-range is occurring, but the total scattering intensity is staying constant, the shape of the particle is changing. Is the maximum of the intensity dropping the degree of fluctuations in the bilayer is altered.

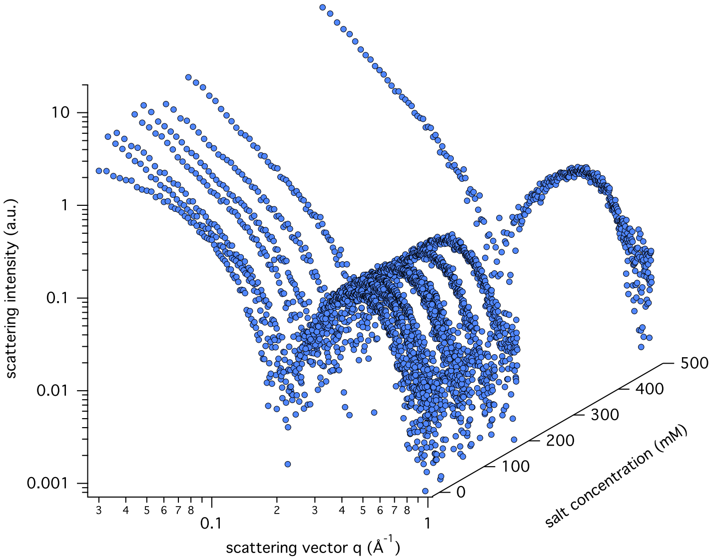

Figure 4.8: SAXS data for DMPG dispersions at 22 ° C varying the ionic strength between 10 mM and 500 mM. The data was recorded upon heating of the sample.

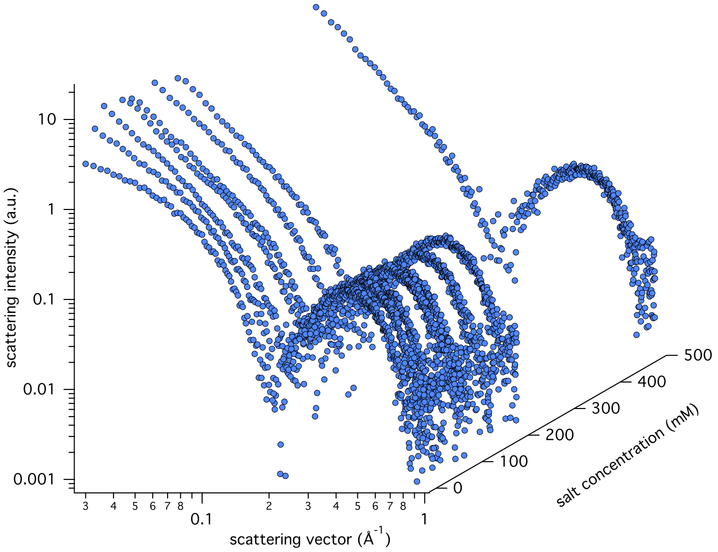

Figure 4.9: SAXS data for DMPG dispersions at 22 ° C varying the ionic strength between 10 mM and 500 mM. The data was recorded upon cooling of the sample.

Taking a closer look at the samples collected at 22 ° C, inspecting results from an upscan and a subsequent downscan as shown in Figure 4.8 and 4.9, respectively, the curves are close to identical, indicating that the phenomenon occurring in the phase transition is reversible and does not change upon passing the sample through the phase transition. The most obvious difference between the sample with 10 mM NaCl and the higher ionic strengths is the slope of the curve at low q-values. The steepness of the slope is correlated to the salt concentrations, the higher the salt concentration the more negative the slope. The bilayer correlation peak is not changing upon variation of the salt concentration.

Comparing the data of the samples inside and outside of the transition it can be ascertained, that the observed changes in the correlation peak resulted from the melting of the acyl chains. Remarkable is the change in slope at low q-vectors, that can be traced over the change in salt concentration.

Figure 4.10: SAXS data for DMPG dispersions with 10 mM NaCl plotted for an upscan, measuring data in the temperature range between 15 ° C and 34 ° C.

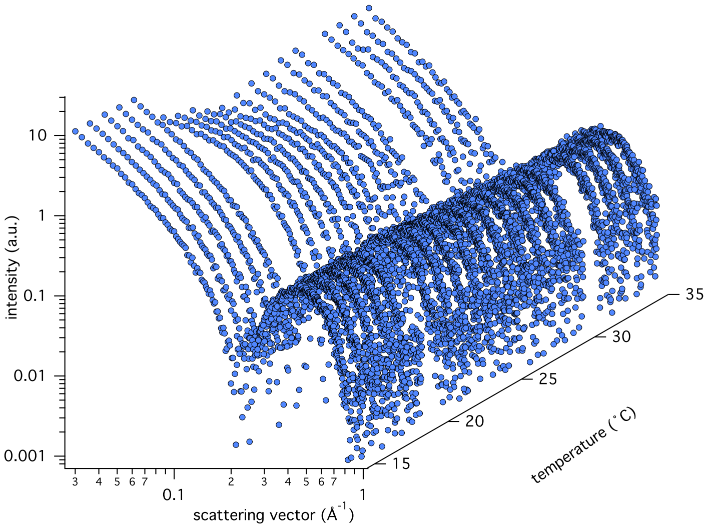

Plotting the data from upscan and downscan of the sample containing 10 mM salt the changes in slope at low q-vectors becomes again visible, as shown in Figure 4.10 and 4.11. The bilayer correlation peak is again rather constant over the whole temperature range. Concentrating on changes in the slope occurring in the upscan it can be seen that with entering the temperature window of the phase transition at 20 ° C the slope starts to increase. The maximum is reached around 24 ° C, followed by a subsequent decrease reaching a plateau level around 28 ° C. For the equivalent downscan a similar behaviour results. The same increase in slope is occurring. The position of onset, maximum and the offset of the slope-change is shifted towards lower temperatures, likely to be caused by to fast measurement and hysteresis. The observed changes are likely to be caused by a higher degree of undulation in the bilayer closely associated to the phase transition.

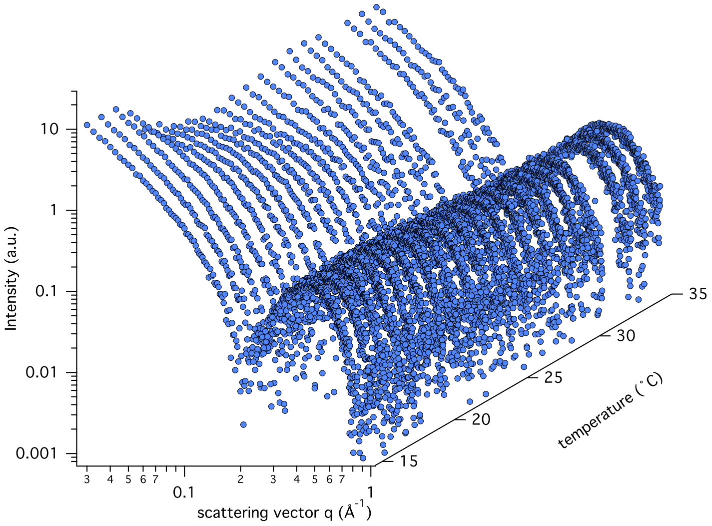

Figure 4.11: SAXS data for DMPG dispersions with 10 mM NaCl plotted for an downscan, measuring data in the temperature range between 15 ° C and 34 ° C.

This change in slope is an unique feature for DMPG at low ionic strength. At high ionic strength (500 mM) the change in slope can not be observed (see Figure 4.12). Here the slope in the q-range stays constant and only a small drop in the scattering intensity can be observed. This is caused by the phase transition, in particular the melting of the chains, causing a decrease in the scattering intensity as a result of the smaller vesicle size.

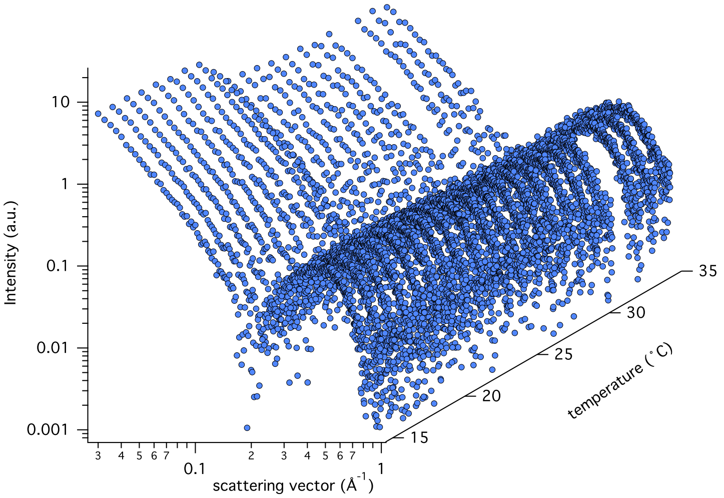

Figure 4.12: SAXS data for DMPG dispersions with 500 mM NaCl plotted for an upscan, measuring data in the temperature range between 15 ° C and 34 ° C.

Summing up the results from the SAXS experiments it can be concluded that the bilayer thickness and contrast between the lipid bilayer and the buffer is constant for all temperatures and salt concentrations. No differences between upscans and downscans could be detected. Changes in the bilayer thickness are result of the chain melting and observed for all lipids. The changes in the slope in the low q-vector range could only be observed for low ionic strength and in the temperature window of the phase transition. This behaviour is a reversible process, observed in the upscan and downscan. As the maximum of the scattering intensity got decreased upon increase of the slope at low q-vectors, a change in the degree of spacial fluctuation on the bilayer level is indicated.

This results are now compared to data from SANS studies, extending the q-range to measuring down to about 0.004 Å $^{-1}$, using the concept of contrast variation enhance the constrast between the lipid bilayer and the solvent.

4.1.5 Small angle neutron scattering (SANS)

Standard SANS experiments were performed on the SANS-1 instrument at the Geesthacht Neutron Facility (GeNF) at the FRG-1 reactor. 10 mM DMPG were mixed with buffers containing 10 mM, 50 mM, 150 mM or 500 mM NaCl, using heavy water as solvent. Unilamellar vesicles were produced by filter extrusion. To be able to study effects introduced by the phase transition the individual samples were studied in the gel phase (15 ° C), in the transition region (22 ° C) and in the fluid phase (35 ° C). Data was collected for different sample to detector distances and after general corrections, averaging and radial integration, combined to yielding a scattering curve covering the complete accessible q-range. The results as presented in Figure 4.13, showing the scattering curves grouped for the different temperature points.

The scattering curve for the samples containing 50 mM, 150 mM and 500 mM are close to identical for all temperatures. At 22 ° C the slope of the sample with the lowest ionic strength is comparable to the data from the corresponding SAXS experiment. This is indicating that the bilayer undulations can also be observed in SANS experiments. At 35 ° C the slope of the scattering curve is changing from -2 close to -4. This decline is characteristic for a densely packed spherical particle. In this case, due to the lack of Bragg peaks, the presence of multilamellar vesicles with uncorrelated bilayers is most likely. The evidence for the bilayer undulations in the phase transition region are further explored with Rheo-SANS

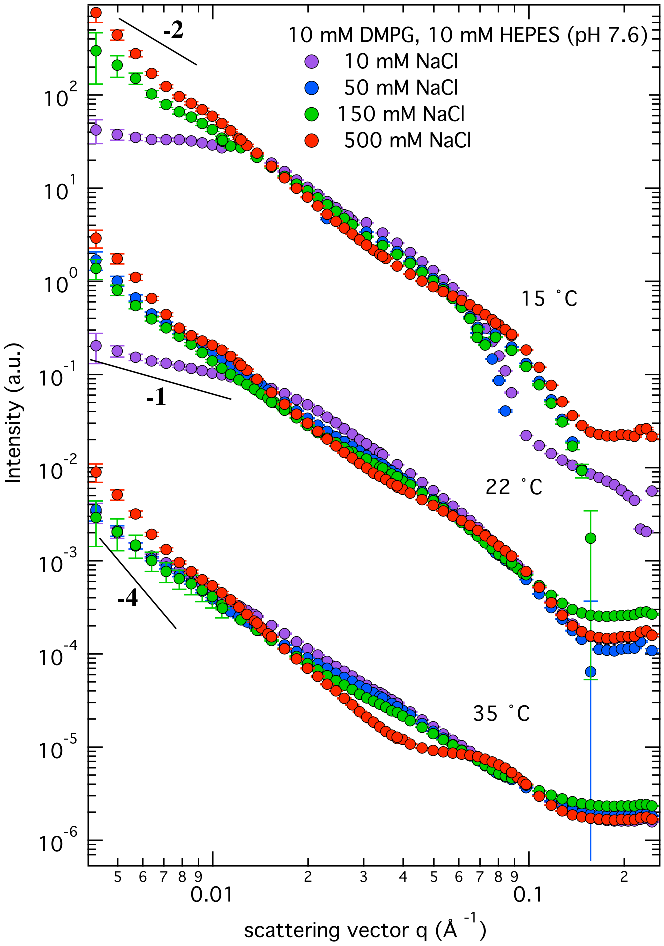

Figure 4.13: Results from SANS experiments performed on unilamellar extruded vesicles at different ionic strength(10 mM, 50 mM, 150 mM, 500 mM) for three different temperatures, deriving data from lipids in the gel phase (15 ° C), the transition region (22 ° C) and the fluid phase (35 ° C). Plots are shifted for better visibility.

4.1.6 Ultra small angle neutron scattering (USANS)

In a standard SANS experiment the average radius of the vesicle could not be determined, as the size of the particle exceeds the accessible q-range. USANS is a versatile tool to study particle sizes up to the μm range. The principle data reduction for USANS data is similar to the one for standard SANS experiments, but due to the high divergence of the neutrons reaching the detector only the upper half of the detector is used to do a radial averaging and integration step.

USANS data were collected on the KWS-2 instrument at JCNS/FRM-2. The raw data of the USANS experiment performed at 22 ° C is shown in Figure 4.14 on the left and the reduced data is shown on the right (black dots). Due to the long exposure time it was only possible to perform one experiment of this type. To determine the radius of the particles immersed in the buffer a Guinier fit is done, as introduced in the theory chapter. Guinier fits are performed by fitting a straight line to the data points in the low q-range in a $\log_{10}I(q)$ vs

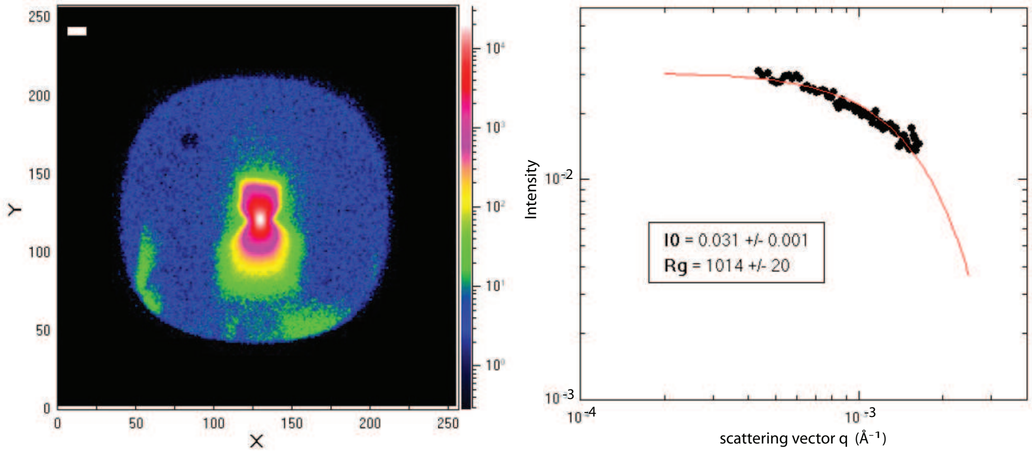

Figure 4.14: (left) raw data of the USANS experiment, showing the distribution of the scattering intensity over the detector. (right) Guinier fit of the integrated and averaged data set, giving a Guinier radius of 1014 Å .

q^2 representation. The fit, indicated by a red line in Figure 4.14 on the right side, yields a radius of gyration of 1014 Å ± 20 Å corresponding to a real particle radius of 1308 Å .

Figure 4.15: Combination of USANS and SANS data collected from DMPG samples in a buffer with 10 mM NaCl, measured at 22 ° C.

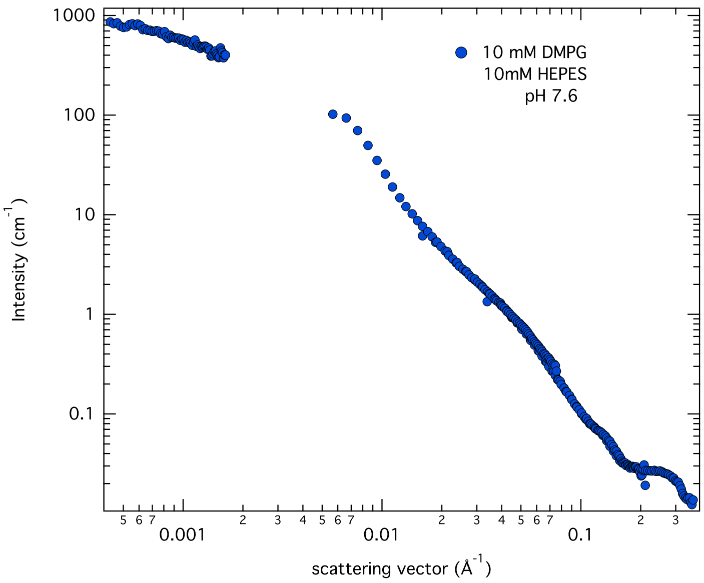

Absolute scaling of the USANS data and plotting together with conventional SANS data collected on the same sample would give one coherent curve. The gap in the data as shown in Figure 4.15 is a result of the lack of a 20 m configuration at the used spectrometer.

4.1.7 Rheo-SANS

Special for DMPG dispersions at low ionic strength is the increased viscosity in the region of the main phase transition. Replacing an cuvette by a Couette cell the structure and changes induced under shear can be studied. The experiments were performed twice, ones at the KWS-2 beamline at JCNS/FRM-2 using a sapphire cell and a low shear rate of about 1 Hz and second on the NG7 instrument of the Center for Neutron Research at NIST using a cell as described by Porcar et al. [124] at a shear rate of 100 Hz. The shear rates given are independent of the instrument, allowing a direct comparision of the measurement. The experiments at KWS-2 were performed for a standard sample containing 10 mM DMPG and 10 mM NaCl in the buffer and one containing 200 mM NaCl in the buffer. The results were compared to static measurements at 22 ° C in the same sample environment.

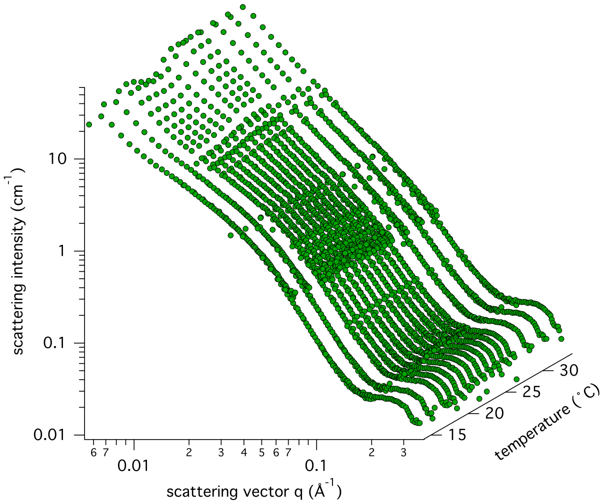

Figure 4.16: Rheo-SANS data collected at temperatures between 15 ° C and 34 ° C of DMPG samples at low ionic strength (10 mM NaCl). Shear rate 1 Hz.

The results from the measurements performed at high and low ionic strength vary in different features. The overall slope of the curves is varying for the two salt conditions. At low ionic strength the slope in the low q-ranges is below -2 indicating that the shape of the particle is most likely an elongated unilamellar vesicle. In contrast, for the sample at high ionic strength, the slope in the low q-range is close to -4, typical for a densely packed particle. In the high q-range a peak around 0.1 $Å^{-1}$ rises, speaking for a dense packing of lamellae. Most likely the multilamellar vesicles in the samples got squeezed together and the bilayers came closely together leading to the emergence of this Bragg peak in the high q-range.

Another important feature in the data collected at low ionic strength are the changes in the bilayer undulation during the phase transition. As one sample was used throughout the experiment, the overall scattering intensity should be constant during the whole data

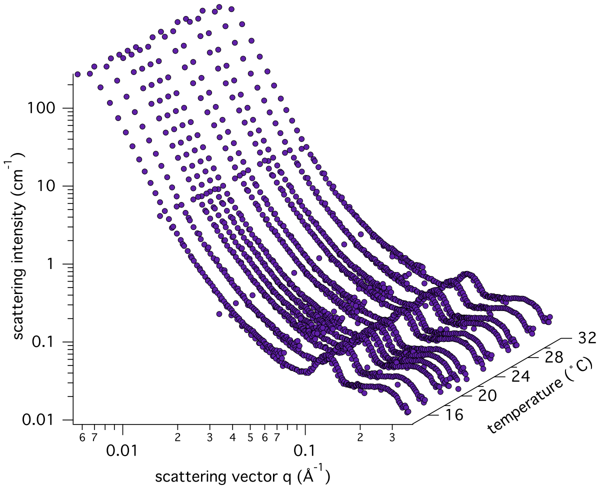

Figure 4.17: Rheo-SANS data collected at temperatures between 15 ° C and 34 ° C of DMPG samples at high ionic strength (200 mM NaCl). Shear rate 1 Hz.

collection. For the experiments performed with the sample containing 200 mM salt this is true, but not for the studies at low ionic strength. Here the scattering intensity drops in the temperature range corresponding to the region of the main transition.

A more detailed data analysis was performed fitting the form factor of a cylinder with a core-shell cross section, including the a polydispersity parameter to vary the core-thickness. The particular formulas are given in Appendix C. Results for three temperature points (15 ° C, 22 ° C, 35 ° C) are listed in Table 4.1.

Table 4.1: Results from the fit of the Rheo-SANS data of DMPG at low ionic strength using the FF for a polydisperse coreshell cylinder, collected at a shear rate of 1 Hz. The parameters are the mean core radius (radius), the radial polydispersity (polydis.), the core length, the radial shell thickness (shell thick), the face shell thickness (face thick), the scattering length density for the core and the solvent (SLD c & s) and the scattering length density of the shell (SLD shell).

temperature	15°C	22°C	35°C
radius (Å)	218.30 ± 0.06	227.05 ± 0.05	234 ± 0.05
polydis. (σ)	0.35 ± 1.0 $\cdot 10^{-5}$	0.33 ±9.0 $\cdot$ 10^{-5}	0.32 ± 8.0$\cdot$ 10^{-5}
core length (Å)	2953.81 ± 0.25	3032.47 ± 0.24	3026.06 ± 0.23
shell thick (Å)	33.99 ± 0.023	34 ± 0.02	32 ± 0.02
face thick (Å)	33.99 ± 0.17	33.99 ± 0.16	34 ± 0.15
SLD c & s (Å $^{-2}$)	6.36 $\cdot$ 10^{-6}	6.36 $\cdot$ 10^{-6}	6.36 $\cdot$ 10^{-6}
SLD shell (Å $^{-2}$)	7.89$\cdot$ 10^{-7}± 7.4 $\cdot$ 10^{-8}	1.3 $\cdot$ 10^{-7}± 3.1 $\cdot$ 10^{-8}	1.19 $\cdot$ 10^{-7} ± 1.9 $\cdot$ 10^{-8}

The FF allows to vary a number of parameters. Four parameters define the spacial dimensions of the cylinder, including the mean core radius (Å) giving the inner diameter, the core length (Å) giving the inner length, the radial thickness (Å) giving the lamellae thickness and the face shell thickness (Å) representing the thickness of the lamellae at the thin end of the cylinder. In addition the scattering length density (SLD) of the core, the shell and the solvent is given. The SLD of solvent and core is fixed to the value of heavy water. The size distribution of the particles was taken into account by introducing a parameter allowing for a certain degree of radial polydispersity (σ). The fits revealed a basically constant thickness of the lipid bilayer, length of the particle and also a rather constant degree of polydispersity. Changes occurred in the core radius increasing with temperature. This effect is triggered by the melting of the acyl chains and the increased volume the molten chains fill, compared to the lipids in the crystalline phase. The SLD is slightly decreasing with increasing temperature, that may indicate that the amount of heavy water molecules in the membrane, mainly in the headgroup region, is changing.

Repeating the Rheo-SANS experiments with a higher shear rate, reveals a dependence of the degree of the fluctuations with the shear rate.

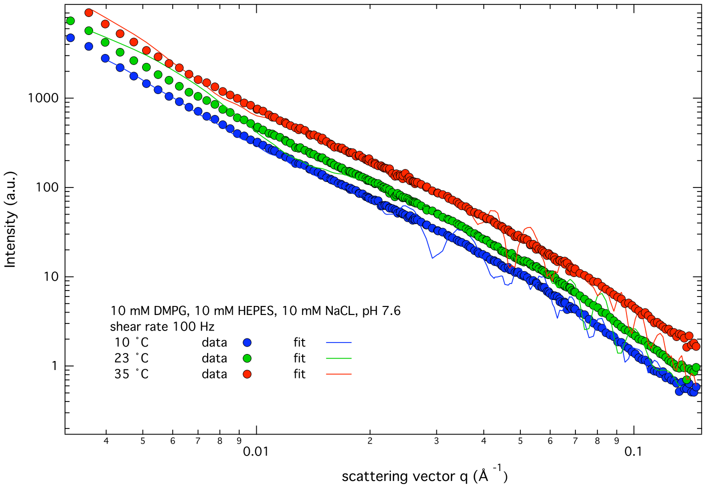

Figure 4.18: Rheo-SANS data collected of temperatures at 15 ° C, 23 ° C and 34 ° C of DMPG samples at low ionic strength (10 mM NaCl). Shear rate 100 Hz. Curves are shifted for better visibility.

At a shear rate of 100 Hz the change in slope as observed for the low shear rate is no longer visible (Figure 4.18). Comparing data from DMPG samples at low ionic strength collected at 15 ° C, 23 ° C and 35 ° C shows no difference in the slope of the curves. The traces are identical and are only shifted in the diagram to provide better visibility.

A detailed data analysis fitting the same FF as described above yields the data listed in Table 4.2. The parameter defining the spacial dimensions of the particle changed with temperature. At 15 ° C the radius was fitted with 174.63 Å ± 0.85 Å , dropping to 149.63 Å ± 0.40 Å and increasing to 218.67 Å ± 055 Å at 35 ° C, concurrently the length of the cylinder has the tendency to drop, same is true for the radial polydispersity. The thickness of the bilayer at the long side and the cap of the cylinder is constant for the lipids in the gel phase, with increasing temperature a small difference between the thickness of the bilayer at the two positions. The thickness at the cap is 4 Å larger than at the long side of the cylinder. This is reasonable as the force deforming the bilayer is more pronounced on the long side of the bilayer than at the cap. The SLD of the core and the solvent was again fixed to the literature value of heavy water. In contrast the SLD of the shell did change from $3.60 \cdot 10^{-7}$ Å $^{-2} \pm 2.9 \cdot 10^{-8}$ Å $^{-2}$ over $5.82 \cdot 10^{-7}$Å $^{-2} \pm\ 2.7 \cdot 10^{-8}$ Å $^{-2}$ to $2.19 \cdot 10^{-7}$ Å $^{-2} \pm 6.5 \cdot 10^{-8}$ Å $^{-2}$. The variations in the fit at the high q-range are a result of the different resolution of the fit and the data.

Table 4.2: Results from the fit of the Rheo-SANS data of DMPG at low ionic strength using the FF for a polydisperse coreshell cylinder, collected at a shear rate of 100 Hz. The parameters are the mean core radius (radius), the radial polydispersity (polydis.), the core length, the radial shell thickness (shell thick), the face shell thickness (face thick), the scattering length density for the core and the solvent (SLD c & s) and the scattering length density of the shell (SLD shell).

temperature	15 °C	22 °C	35 °C
radius (Å)	174.63 ± 0.85	149.63 ± 0.40	218.67 ± 055
polydis. (σ)	$0.60 \pm 1.0 \cdot 10^{-5}$	$0.36 \pm 1.0 \cdot 10^{-5}$	$0.4 \pm 8.0 \cdot 10^{-5}$
core length (Å)	3340.41 ± 1.69	3033.87 ± 2.73	3025.68 ± 1.77
shell thick (Å)	36 ± 0.24	32 ± 0.17	32 ± 0.18
face thick (Å)	36 ± 0.85	36 ± 1.53	36 ±1.02
SLD c & s (Å $^{-2}$)	$6.36 \cdot 10^{-6}$	$6.36 \cdot 10^{-6}$	$6.36 \cdot 10^{-6}$
SLD shell (Å $^{-2}$)	$3.60 \cdot 10^{-7} \pm 2.9 \cdot 10^{-8}$	$5.82 \cdot 10^{-7} \pm 2.7 \cdot 10^{-8}$	$2.19 \cdot 10^{-7} \pm 6.5 \cdot 10^{-8}$

Whereas the Rheo-SANS at low shear rates still allowed to study the fluctuations in the bilayer, the high shear rate diminishes this phenomenon. Here another effect can be traced. In the phase transition upon the coexistance of lipids in the gel phase and the fluid phase, the membrane becomes very deformable, pronounced in the data by a drop in the radius of the cylinder. In addition the amount of water able to bind to the headgroup has increased reflected by an increase in the SLD of the shell.

With a last experimental technique, confocal fluorescence microscopy, changes in the morphology should be addressed in a nanometer scale.

4.1.8 Confocal fluorescence microscopy

Complementary to the scattering experiments confocal fluorescence microscopy was performed. Pictures were acquired for vesicles incubated at 20 ° C with the membranes labelled with Di-C_{18}, NBD-head or NBD-chain recording changes in the vesicles over time. Vesicles prepared with a buffer of low ionic strength and high ionic strength were studied in parallel. The vesicles formed in the buffer with low ionic strength were on average 5 μm in diameter. The first picture was taken about 20 min after the preparation, defined as starting point. Further recording were taken after 13 min, 37 min, 48 min, 88 min, 187 min and

195 min, as shown in Figure 4.19. The vesicles appear as bright dots in the first recordings. Over time more and more individual bilayer become visible and onion like structures appear. Buds of vesicles occur, indicating that fission of multilamellar vesicles is yielding unilamellar vesicles. The pictures taken after 3 hours after the sample preparation shows a relevant fraction of unilamellar vesicles, some still attached to each other. Pictures taken from the samples with 500 mM salt in the buffer revealed a different behaviour. The vesicles appeared much smaller and randomly distributed in the beginning. Observed over time the vesicles tend to aggregate (Figure 4.20).

A second set of confocal microscopy experiments was performed varying the temperature of the sample. To proof the reproducibility and the influence of the lipid phase state, vesicles were passed through the phase transition, recording pictures at 15 ° C, 22 ° C and 35 ° C. A selection of the images recorded is given in Figure 4.21. In the upper row samples were prepared with buffers of low ionic strength, in the lower row samples were prepared with high ionic strength buffer. At low ionic strength the emergence of large unilamellar vesicles was observed. In the region of the phase transition the fluorescence dyes are not equally distributed anymore, indicating that domain formation occurred. For the samples in high ionic strength buffer, the collected images are similar to the one collected in the earlier experiments. Mainly small vesicles form, appearing as bright spots in the pictures.

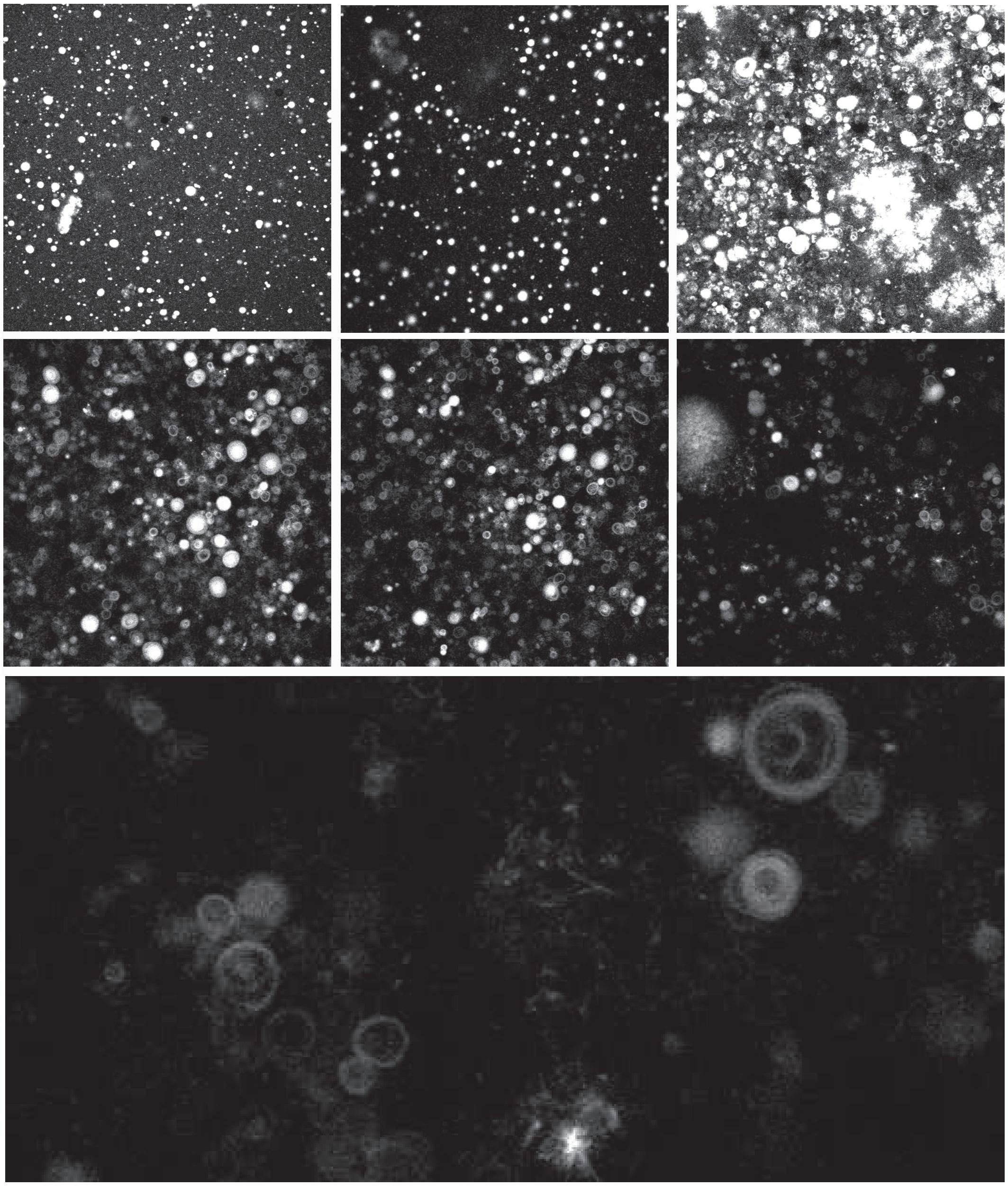

Figure 4.19: Result from confocal fluorescence microscopy of DMPG vesicles in buffer with low ionic strength at 20 ° C. Pictures were taken at 13 min, 37 min, 48 min, 88 min, 187 min and 195 min after sample preparation. All images are displayed with the same resolution, except the last one, that is magnified. The diameter of the large vesicles is around 5 μm.

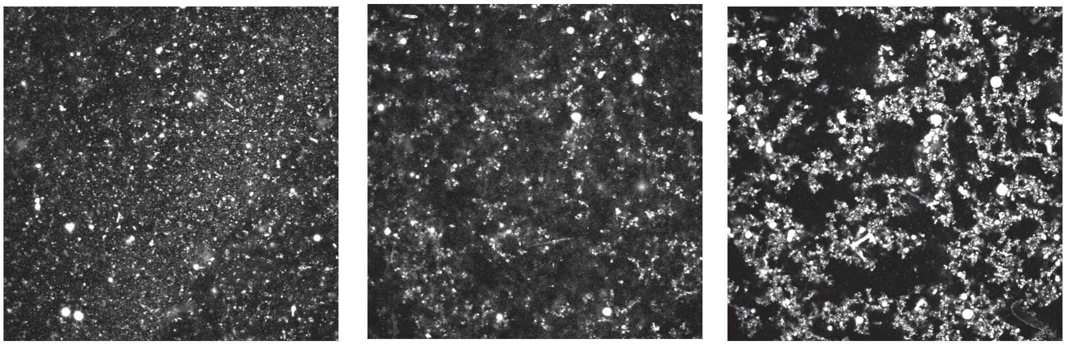

Figure 4.20: Result from confocal fluorescence microscopy of DMPG vesicles in buffer with high ionic strength at 20 ° C. Pictures were taken at directly after the sample preparation, 19 min and 24 min thereafter.

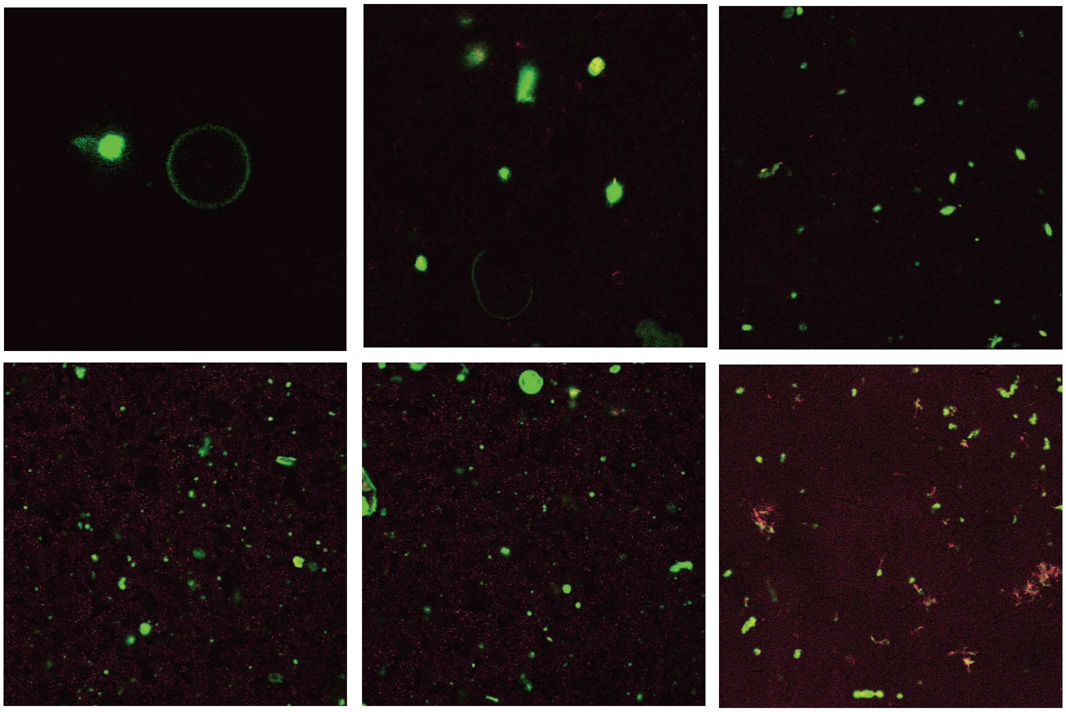

Figure 4.21: Images of confocal fluorescence microscopy performed for samples with low ionic strength buffer (top) and high ionic strength buffer (bottom) at three temperatures, 15 ° C (left), 22 ° C (middle), 35 ° C (right).

4.2 Conclusion

DSC experiments revealed a connection between the charge density on the membrane surface and the complex melting behaviour. Neutralisation of the charges by protonation of the phosphate group or by shielding the charge, adding sodium ions to the buffer, the broad transition peak is narrowing [153][23]. The measured increased viscosity is also depending on the amount of effective charges. The morphological changes addressed by light scattering yielded first evidence for the presence of vesicles in the phase transition. Correcting for the changes in the relative viscosity over temperature led to rather unreasonable small vesicle diameters, coinciding with the temperature window of the phase transition. Comparing the USANS data with the DLS results reveals a discrepancy between the radius calculated from the two methods. For the hydrodynamic radii based on DLS an experimental error of about 20 % can be assumed and apart from a different source of radiation and wavelength, are the USANS results independent of the changes in viscosity. The calculation of the hydrodynamic radius from light scattering data is not only depending on the viscosity, but also taking into account changes in the refractive index. Static light scattering performed with dispersions containing 10 mM DMPG showed multiple scattering events. Comparison to similar data for DMPC shows less pronounced multiple scattering. This result is pointing towards a change in the water environment, most likely an increased number of hydrogen bonds is forming.

Changes in the particle morphology and the bilayer integrity are investigated by SAXS and SANS. Varying the temperature and the ionic strength the integrity of the membrane bilayer persists under all conditions. In SAXS experiments the bilayer correlation peak was only changing as a result of the chain melting, accompanied by a slight decrease in the scattering intensity, due to the decrease of the vesicle diameter. At low ionic strength extensive bilayer fluctuations are recorded for temperatures in the transition region, vanishing with increasing amounts of salt. SANS data revealed the same behaviour. Comparison of data from DMPG and DMPC samples, leads to the conclusion that the extensive undulations of the bilayers are more pronounced in low salt DMPG samples. The fluctuations observed are represented by a drop in the maximum scattering intensity. Going back to Figure 2.2, all scattering curves have the same maximum scattering intensity for the lowest q-values. The data shown was calculated for geometrical bodies with the same maximal dimension. The scattering intensity is proportional to the radius^4. A change in the radius, or the maximum dimension for the non spherical particles, would lead to a dramatic change in the maximum scattering intensity. Inspecting the data collected with SANS and SAXS a clear tendency for reduced intensity for samples with low ionic strength is observed. If the intensity drop is interpreted as a change in the particle geometry, the change in slope could indicate the presence of a cylinder. This can be excluded, as the change in the maximum diameter would increase the intensity dramatically, leaving the increase in scattering intensity to be caused by spacial fluctuations. The effect is caused, by changes in the flexibility of the bilayer. Undulations in the bilayer and small changes in the particle shape lead to a smearing of the scattering signal. The timescale of the scattering event is suitable to trace this changes, but the averaging over all scattering events leads consequently to an averaging over all the different detected morphologies. This unsharpness of the structure is reflected by a decrease in the scattering intensity. The degree of fluctuations and the influence of shear stress was studied by Rheo-SANS. Altering the shear rate and with that the force taking effect on the membrane, yields information about the vesicle morphology and the flexibility of the membrane. For low shear rates, the vesicles get deformed to a cylindrical shape. The fluctuations are still detectable. Increasing the shear rate does not allow to detect the fluctuations any more, but is bearing an increased softness of the particle in the phase transition, reflected by a cylinder with a smaller radius as detected outside of the transition.

Confocal fluorescence microscopy finally revealed the spontaneous emergence of large vesicles in the μm range, tending to build unilamellar vesicles, by undergoing fission events, especially in the temperature regime of the phase transition.

Summing up the results from the methods applied the following can be assumed:

- The bilayer stays intact under all conditions.
- Fluctuations, in the sense of bilayer undulations, are occurring predominantly in the phase transition and only for conditions of low ionic strength.
- The influence of shear is causing a deformation of the vesicles to a cylindrical shape. For high shear rates, the fluctuations of the membrane can no longer be detected, but the increased deformability of the vesicle in the phase transition still remains.

The results are now discussed in context with the theories described in literature.

4.3 Discussion

Recapitulating the models for the morphology in the phase transition for low ionic strength, described in the introduction, in general three models can be distinguished:

1. reversible vesicle aggregation and disaggregation
   This theory was proposed by Riske et al. based on the decreased light scattering

intensity in the region of the phase transition [22].

2. sponge phase
   Investigating the thermodynamic changes in the phase transition enhanced bending elasticity and solvent associated effects lead to the conclusion that the overall morphology is changing, proposing a sponge phase as a likely explanation [153][23].

3. perforated lamellae
   This most recent theory tries to explain the optical and viscous properties of the vesicles in the phase transition by the presence of perforations in the bilayer [26]. Experimental evidence for this phenomenon was found in the SAXS experiments performed with a rather high lipid content [25][26][154].

The relevance of the individual models will now be discussed in context with the results presented above.

The proposal of vesicle aggregation was based on SLS and DLS data [22], calculating a net attraction for vesicles below the phase transition and an attraction above the transition temperature. Studying DMPG dispersions, in particular at low ionic strength, proposing changes in the morphology is only relevant if the applied method is not relying or influenced by changes in the viscosity and the refractive index. For light scattering both criteria are not fulfilled. SLS and DLS are based on recording changes in the refractive index, depending on the shape and size of the particle studied. Good practice is studying very diluted systems without interaction of the particles [155][156]. For turbid solution special cross-correlation techniques can be applied during data collection [134]. Neglecting this principles one runs the risk to collect ill-defined scattering intensities. As shown in Figure 4.3 the decay of the scattering intensity upon changing the temperature is depending on the salt content of the sample. At low ionic strength no remarkable drop in the scattering intensity is recorded, even though the sample turns from turbid to transparent and becomes more viscous. As long as this changes in viscous properties and the optical appearance can not be explained the interpretation of light scattering data maybe misleading. It is advised to use the data together with studies on the viscosity to learn about changes. Statements about the size and shape of the particles in the phase transition should be made from methods that are independent from the viscosity of the solution and changes in the refractive index, like small angle scattering using x-ray or neutrons.

This methods are applied here to check for the possibility of the formation of a sponge phase. Extended network phases are known to occur in lipid dispersions and in polymer solutions. Induced by temperature changes or under the influence of shear [157][158][159][119] morphological changes are often coinciding with changes in the optical properties. The formation of such a phase requires fusion upon entering the phase transition, fission to form vesicles again leaving the transition. Sponge phases are characterized by long-range correlations of bilayers leading to characteristic Bragg peaks. As no evidence for fusion events or even network structures was found, the occurrence of this type of long-range three-dimensional structure is not likely. It should be mentioned that the authors suggesting the sponge phase did not only aim to propose a particular structure but stressed, that a structural change is necessary, to explain the calorimetric profiles[23].

Rather recently a number of publications explaining the particular broad transition peaks and the changes in viscosity, optical density and conductivity by proposing a perforated lamellar phase (L_p) [154]. Initially proposed by Riske et al. [25] studying DMPG dispersions with a concentration of 50 mM , the authors suggested curvature defects induced by changes in the vesicle topology. Imagining the defects as fissures, edges with high curvature are formed. Background for this theory is the vanishing contrast between the membrane and the solvent observed in phase contrast microscopy and SAXS experiment at lipid concentrations higher than 50 mM. The later revealed Bragg peaks reflecting a structure with a repeat distance of 400 Å [26]. The position of this peak is depending on the lipid content. The higher the lipid concentration the shorter the measured repeat distance [154]. This peak is not visible for diluted samples (10 mM DMPG) as shown above. The question is now, do these perforations exist at all or is there an alternative way to explain the Bragg peak. If the emergence of the peak is caused by fissures or perforations in the membrane and their presence is limited to the temperature window of the phase transition a change in the bilayer correlation peak needs to be present. The thickness of the bilayer is not affected, but the contrast needs to change, due to the water filling the perforations. Neither in the work of the authors proposing the perforation nor in the results presented here is giving evidence for such phenomena.

There is an alternative explanation for the peak. For high lipid concentrations it can no longer be assured that the vesicles are purely unilamellar. It is more likely that several vesicles are wrapped around each other building a loosely packed onion like structure. With increasing lipid concentrations the number of shells is increasing and the distance between the individual layers is decreasing. Condition for the appearance of the observed Bragg peak is a regular distance between the layers. Remembering the results of the confocal fluorescence microscopy the large vesicles observed in the phase transition at low ionic strength showed the tendency to form unilamellar vesicles. Inside of the transition the electrostatic repulsion between the bilayer appear much stronger than outside of the transition. If the effective charge close to the bilayer is increasing in the transition the structure of the surrounding water may be affected. The formation of long-range hydrogen bonding networks may be induced. The electrostatic repulsion induced by both bilayer leaflets is maximizing the distance between two bilayers. For an onion like structure the spacing between the bilayers can become close to equal giving rise to diffraction peaks. This hypothesis is in good agreement with sharpness of the peak. Approaching the transition, the peaks are rather broad, in the transition they appear sharper.

The key to understanding the changes in the optical and viscous properties is bridging the bilayer undulations and the induced changes in the water environment to the lipid phase transition. A good approximation for the morphology in the phase transition is the comparison to a hydrogel, as previously proposed [23]. This mostly complex mixtures of amphiphilic molecules, water and cosurfactants like various alcohols, display the same properties as DMPG in the phase transition. Examples are thermosensitive hydrogels, changing the viscosity in a defined temperature regime [160][161][162]. Different to the DMPG dispersions, hydrogels are transparent for all temperatures and undergo a different type of transition. Quaternized chitosan together with polyethylenglycol (PEG) for example is used as thermosensitive hydrogels for drug delivery. The observed gelation process upon rising the temperature is a result of an increase in the internal energy, breaking the hydrogen bonds between the water and the chitosan chains [160]. The movement of free water molecules increased the entropy in the system, and in order to decrease the entropy change, hydrophobic chitosan side chains tend to aggregate. The PEG is needed to facilitate aggregation inducing the gelation.

For the case of DMPG the transparency and the change in the viscosity may also be related to changes in the water environment. The high charge density on the surface of the bilayer may be responsible for the induction of a long-ranging hydrogen bond network, structuring the water molecules in the solution. Upon heating of the sample and leaving the transition region, the hydrogen bonding network is destroyed by the increased amount of thermal fluctuations. Still open is the connection between the structural changes and the changes in the water environment. The scattering methods applied here are only suitable to give qualitative information about the bilayer undulations. Only indirect information about the water environment can be derived.

4.4 Outlook

To follow up on the results presented here a number of further studies are advised to get a more detailed view of undulations and the changes in the water environment. Sticking to the set of methods introduced here, it would be reasonable to perform further SANS and Rheo-SANS experiments varying the amount of heavy water in the buffer. It is known that heavy water in high concentrations is toxic for higher eukaryotes and changes physiological function in a variety of organisms [163][164]. This is returned to the different binding affinity of protons and deuterons to oxygen. The different binding constant is influencing the formation of hydrogen bonding networks.

For more quantitative information about the bilayer undulations and the mobility of water in the proximity of the bilayer surface the use of inelastic neutron scattering techniques is advised. Neutron spin echo spectroscopy for example can be applied to study undulations in model membranes [165][166][167]. Main drawback for basically all inelastic scattering techniques is the sample preparation. Whereas the SANS and SAXS experiments could be performed on vesicles immersed in an aqueous solution, the inelastic methods require an planar aligned bilayer. Most common is the use of supported, oriented bilayer stacks, identical to the preparation used for neutron diffraction experiments. For DMPG samples at low ionic strength, the preparation of the bilayer stacks is not as straight forward as for analog zwitterionic lipids and the sample quality may not be sufficient for inelastic scattering experiments. One could consider experiments on a single supported bilayer even though this would lead to a weak scattering signal and difficult data interpretation.

Chapter 5

Structural changes introduced upon interaction with membrane-active compounds

5.1 Membrane-active compounds

5.1.1 Results from experiments with Angiotensin II

Differential scanning calorimetry (DSC)

To get a first idea about the interaction of Ang II with DMPC, DSC was used, studying Ang:DMPC ratios of 1:5, 1:10, 1:50 and 1:100, compared to pure lipid dispersions. In Table 5.1 the resulting scans are listed and in Figure 5.1 the corresponding thermotropic traces are shown. The table comprises the values for the peak temperatures of the pretransition (peak_{pre}) and main transition ($\text{peak}_{\text{main}}$). In addition the enthalpy was calculated by integration of the area under the main transition peak and the pretransition peak. Another indicator for changes in the phase behavior is the upper phase boundary, representing the temperature where half of the lipids are in the gel state and the other half is in the fluid state [11].

For pure DMPC a sharp main transition peak just below 24 ° C and in addition a pre-transition around 14 ° C is expected. The measurement yields a temperature of 23.6 ° C for the main transition and 13.8 ° C for the pre-transition. Accordingly the enthalpy for the main transition was calculated as 6.55 kJ/mol and as 1.37 kJ/mol for the pre-transition.

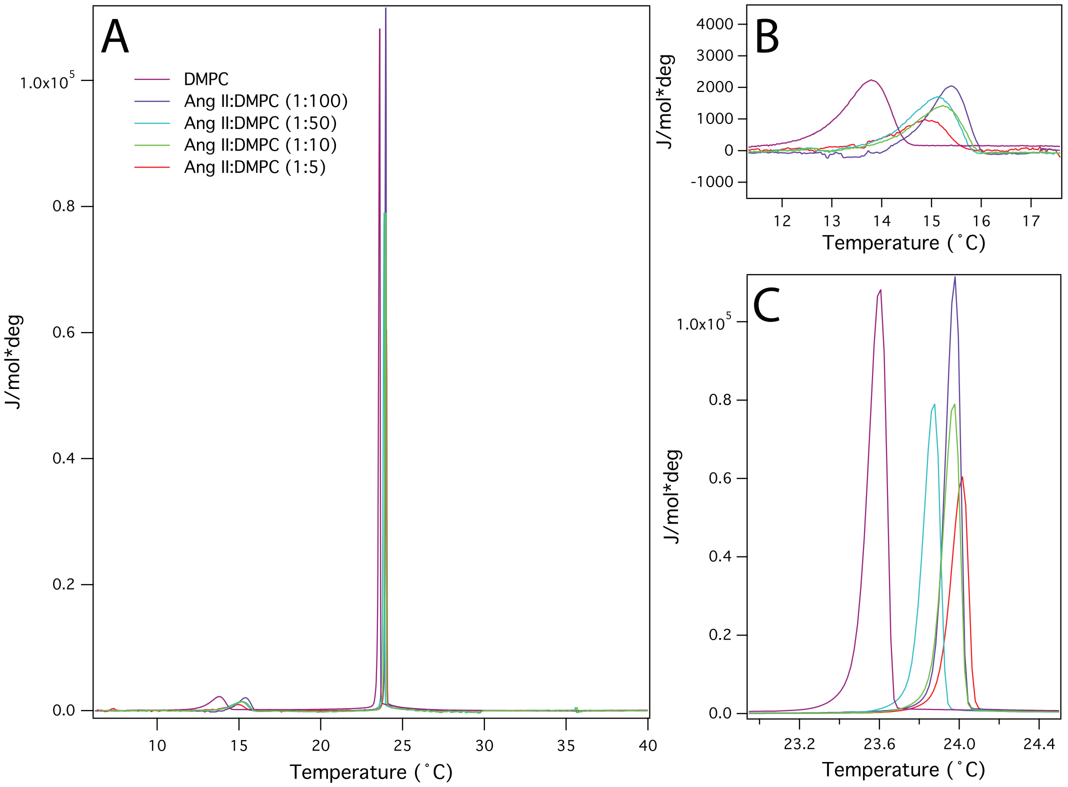

Figure 5.1: Calorimetric traces for DMPC traces upon interaction with different temperatures of Ang II. The complete profile is displayed in panel A, a cutout of the pre-transition is given in panel B and of the main transition in panel C.

Table 5.1: Enthalpy and peak temperature of the main transition ($\text{peak}_{\text{main}}$) and pre-transition ($\text{peak}_{\text{pre}}$), as well as the upper phase boundary (UPB) for pure DMPC dispersions and DMPC mixed with Ang II in the peptide: lipid ratios 1:100, 1:50, 1:10, 1:5. The enthalpy C_p is given in J/mol · deg for the main transition ($\text{Enthalpy}_{\text{main}}$) and the pretransition ($\text{Enthalpy}_{\text{pre}}$).

sample	DMPC	1:100	1:50	1:10	1:5
$\text{Enthalpy}_{\text{main}}$	6.55 ± 0.91	8.04 ± 1.22	8.81 ± 1.23	9.60 ± 1.34	10.36 ± 1.45
$\text{Enthalpy}_{\text{pre}}$	1.37 ± 0.19	1.44 ± 0.20	1.64 ± 0.23	1.85 ± 0.25	1.76 ± 0.24
$\text{peak}_{\text{main}}$ (°C)	23.6	24.0	24.0	24.0	24.0
peak_{pre} (°C)	13.8	15.2	15.3	15.1	15.1
UPB (°C)	23.6	24.0	24.0	24.1	24.1

With increasing concentrations of Ang II the peak temperature gets shifted towards higher temperatures and the enthalpy increases. For the main transition the enthalpy increases constantly with increasing concentrations of the peptide. The initial addition of the peptide leads to an increase in enthalpy by about 1.5 kJ/mol. For the higher concentrations a smaller increase in the enthalpy of the main transition can be observed. For the next lower ratio the enthalpy is increasing by about 600 J/mol.

The enthalpy of the pre-transition changes also with the addition of the peptide. At the highest lipid:peptide ratio (1:100) an increase of 72 J/mol was calculated. For the lipid peptide ratio of 1:50 the enthalpy raises more than 200 J/mol. Finally for the peptide:lipid ratio of 1:10 the enthalpy increases again by about 200 J/mol compared to the previous ratio. For the highest concentration of the peptide and a ratio of peptide to lipid of 1:5 the enthalpy of the pre-transition drops slightly compared to the next lower peptide concentration.

Studying the temperature change induced by the peptide, again the temperature of the main transition and for the pre-transition can be compared for pure DMPC and samples containing Ang II in addition. The temperature of the main transition is shifted between 0.4 ° C and 0.6 ° C as a response to Ang II binding. Comparing the temperature of the pure DMPC sample and after addition of peptide with a peptide:lipid ratio of 1:100 an increase in the transition temperature of 0.4 ° C is observed. For the higher peptide concentrations only a small further increase of the temperature can be seen. A similar result yields the analysis of the pre-transition temperature. The temperature raises by 1.3 ° C for the addition of the peptide at the lowest concentration and by around 0.2 ° C for the next higher peptide concentration. For the higher peptide concentrations the result is different. The temperature always stays above 15 ° C. Another indicator for changes occurring at the membrane is the upper phase boundary, the temperature where an equal number of lipids are in the fluid state and in the gel state. The upper phase boundary (UPB) for pure DMPC was calculated as 23.64 ° C and it raises by 0.42 ° C for the two lowest peptide concentrations. For the two higher concentrations the temperature raises by 0.46 ° C.

As the pre-transition temperature is more sensitive to changes at the membrane surface a change in the pre-transition temperature points towards an interaction of the peptide with the membrane surface. Upon molecules interacting not only with the surface, but at the interface region or in the hydrophobic region the pre-transiton will vanish completely. In the present experiment the pre-transition remains visible in the data and gets shifted towards higher temperatures by more than 1 ° C. The peak broadens and the enthalpy increases.

The enthalpy of the main transition is also increasing except for the highest peptide concentration. This non-linear increase in the enthalpy supports a weak binding and interaction with the surface of the bilayer. With decreasing lipid:peptide ratio a saturation level is reached, where no further peptide molecules bind to the surface.

Dynamic light scattering

The dynamic light scattering was applied as to get a first insight into the structural changes occurring in the vesicles upon addition of the peptide, using the same Ang II:DMPC ratios as for DSC, with the results shown in Figure 5.2 and Tabelle 5.2.

Table 5.2: Hydrodynamic radii from dynamic light scattering experiments for pure DMPC dispersions and lipid peptide mixtures with different ratio, shown for temperatures between 35 ° C and 5 ° C.

temperature	hydrodynamic radius (nm) for Ang II: DMPC ratios of				
(°C)	(1:100)	(1:50)	(1:10)	(1:5)	DMPC
35	59.0 ± 4.5	56.7 ± 4.5	57.3 ± 4.2	52.7 ± 4.2	53.1 ± 4.7
33	58.7 ± 4.5	56.4 ± 4.6	58.7 ± 4.2	53.5 ± 4.1	52.4 ± 4.6
31	60.4 ± 4.6	58.1 ± 4.8	60.5 ± 4.3	54.6± 4.3	54.4 ± 4.8
29	62.1 ± 4.7	59.7 ± 4.9	62.1 ± 4.4	56.2± 4.5	56.5 ± 4.9
27	64.3 ± 4.9	61.9 ± 5.0	62.5 ± 4.5	56.9 ± 4.6	57.6 ± 5.1
26	65.4 ± 5.0	62.8 ± 5.1	64.3 ± 4.7	59.0 ± 4.7	59.0 ± 5.2
25	67.8 ± 5.2	65.2 ± 5.3	67.1 ± 4.7	59.6 ± 4.8	60.1 ± 5.4
24	69.0 ± 5.3	66.3 ± 5.5	68.9 ± 4.9	61.2 ± 4.9	62.1 ± 5.5
23	71.2 ± 5.4	68.5 ± 5.5	68.8 ± 5.0	62.5 ± 5.0	63.2 ± 5.7
22	72.9 ± 5.6	70.1 ± 5.7	72.3 ± 5.1	63.9 ± 5.1	64.4 ± 5.8
21	73.8 ± 5.6	71.0 ± 5.8	72.6 ± 5.2	65.5 ± 5.2	65.0 ± 5.9
20	76.3 ± 5.8	73.4 ± 6.0	75.7 ± 5.3	66.5 ± 5.5	69.1 ± 6.1
19	79.4 ± 6.1	76.4 ± 6.1	76.1 ± 5.2	65.9 ± 5.4	67.5 ± 6.3
18	80.0 ± 6.1	76.9 ± 6.2	78.6 ± 5.4	68.2 ± 5.6	70.0 ± 6.4
16	82.3 ± 6.3	79.1 ± 6.4	80.7 ± 5.5	68.8 ± 5.5	69.9 ± 6.5
14	85.2 ± 6.5	82.0 ± 6.4	81.1 ± 5.8	72.5 ± 5.9	74.0 ± 6.8
12	88.1 ± 6.7	84.8 ± 6.6	82.8 ± 5.8	73.1 ± 6.0	75.6 ± 7.0
10	88.4 ± 6.8	85.0 ± 6.9	86.7 ± 6.0	75.5 ± 6.1	76.7 ± 7.0
8	93.2 ± 7.1	89.7 ± 6.9	87.2 ± 6.1	76.7 ± 6.3	79.4 ± 7.4
6	93.3 ± 7.1	89.7 ± 7.3	91.3 ± 6.3	79.5 ± 6.5	81.3 ± 7.4
5		92.6 ± 7.4	82.1 ± 6.5	84.1 ± 6.7	

The main information gained from light scattering experiments is the hydrodynamic radius. Temperature was varied in one degree steps between 5 ° C and 35 ° C. For the experiments extruded vesicles were used and the buffer contained the peptide in the same concentrations as used for DSC. The addition of the peptide is mainly leading to an increased hydrodynamic radius. Initially a hydrodynamic radius about 60 nm was measured for DMPC above the phase transition. Lowering the temperature leads to a gradual increase in the hydrodynamic radius. Below the phase transition the radius reaches around 90 nm. The difference in radius can be explained due to the decreased mobility of the particles at low temperatures and the difference in radius caused by the phase transition.

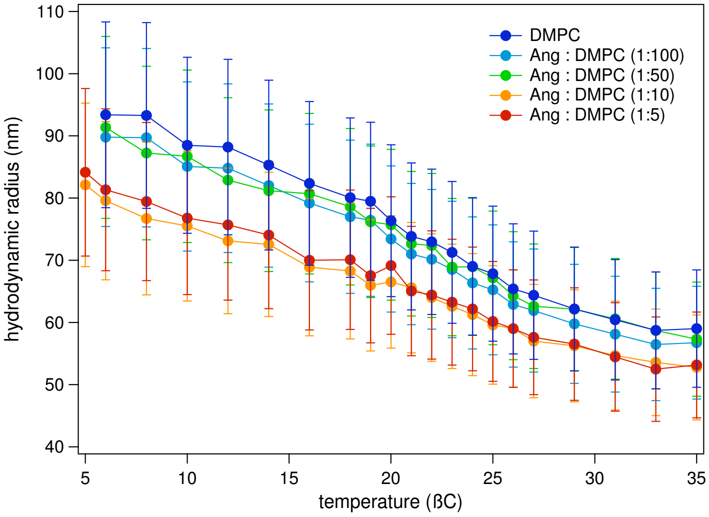

Figure 5.2: Dynamic light scattering data showing the hydrodynamic radii calculated for temperatures between 5 ° C and 35 ° C. The bars indicate the error, resulting from the polydispersity of the vesicles. The line between the data points is added to provide better visibility

Small angle neutron scattering

To get an insight into the structural changes occurring on the membrane level SANS was applied, using the SANS-I instrument at GeNF. To make sure that only single particle form factors are measured a diluted dispersion was used, containing 10 mM lipid. The dispersion was extruded to avoid aggregation and periodic packing of bilayers that may give rise to Bragg peaks. All samples were measured with respect to the different lipid phases at 15 ° C, 22 ° C and 35 ° C.

After general corrections, averaging and integration of the data, a detailed data analysis was performed using the separated form factor (SFF) approach [168]. Two form factors (FFs) were combined, leading to the possibility to describe the vesicle and the structure of the lamellae at the same time. In detail the first FF describes the tail length and the thickness of the head group and the corresponding scattering length densities (SLDs), respectively. The second FF is used to describe the overall structure of the vesicle, taking into account the vesicle size, the bilayer thickness and the polydispersity of the vesicle. For all experiments chain deuterated DMPC (d54-DMPC) was used, having the advantage of a large SLD contrast difference existing between the head group and the acyl chains. A penetration of the peptide into the hydrophobic core would become visible instantly in the data. The results are displayed in Figure 5.3 and in the Tables 5.3 for the different temperatures.

At first the data from the pure d54-DMPC samples were fitted, starting with the data set where the lipids are in the fluid state as only limited literature is available for the gel, respectively ripple phase. For d54-DMPC in the fluid phase literature values were taken were possible or the values for DPPC were used taking into account the difference in tail

Table 5.3: Small angle neutron scattering fit results. Parameters for the particles dimensions and the SLDs are given.

temp (°C)	sample	d54-DMPC	1:100	1:50	1:10
15	tail length (Å)	16.3 ± 0.32	16.3 ± 0.32	16.3 ± 0.32	16.3 ± 0.32
	headgroup thickness (Å)	4 ± 0.06	4.2 ± 0.06	5.0 ± 0.06	7.5 ± 0.08
	SLD tails (Å $^{-2}$)	$7.25 \cdot 10^{-6}$	$7.2 \cdot 10^{-6}$	$7.15 \cdot 10^{-6}$	$7.1 \cdot 10^{-6}$
	SLD headgroup (Å $^{-2}$)	$1.1 \cdot 10^{-6} \pm 0.01 \cdot 10^{-6}$	$1.1 \cdot 10^{-6} \pm 0.01 \cdot 10^{-6}$	$1.9 \cdot 10^{-6} \pm 0.01 \cdot 10^{-6}$	$3.3 \cdot 10^{-6} \pm 0.03 \cdot 10^{-6}$
	SLD solvent (Å $^{-2}$)	$6.36 \cdot 10^{-6}$	$6.36 \cdot 10^{-6}$	$6.36 \cdot 10^{-6}$	$6.36 \cdot 10^{-6}$
	background (cm $^{-1}$)	0.009	0.003	0.002	0.001
	average core radius (Å)	740	780	820	880
	average shell thickness (Å)	40.8	40.6	43	41
	overall polydispersity	1 ± 0.03	0.90 ± 0.01	0.96 ± 0.02	1 ± 0.02
	SLD core and solvent (Å $^{-2}$)	$6.36 \cdot 10^{-6}$	$6.36 \cdot 10^{-6}$	$6.36 \cdot 10^{-6}$	$6.36 \cdot 10^{-6}$
	SLD shell (Å $^{-2}$)	$4.78 \cdot 10^{-6}$	$4.78 \cdot 10^{-6}$	$4.78 \cdot 10^{-6}$	$4.78 \cdot 10^{-6}$
22	tail length (Å)	15 ± 0.3	14.5 ± 0.28	14.2 ± 0.28	13.6 ± 0.26
	headgroup thickness (Å)	4.99 ± 0.19	6.09 ± 0.17	7.75 ± 0.14	7.89 ± 0.11
	SLD tails (Å $^{-2}$)	$7.2 \cdot 10^{-6}$	$7.2 \cdot 10^{-6}$	$7.15 \cdot 10^{-6}$	$7.15 \cdot 10^{-6}$
	SLD headgroup (Å $^{-2}$)	$1.45 \cdot 10^{-6} \pm 0.12 \cdot 10^{-6}$	$1.6 \cdot 10^{-6} \pm 0.1 \cdot 10^{-6}$	$2.35 \cdot 10^{-6} \pm 0.007 \cdot 10^{-6}$	$2.6 \cdot 10^{-6} \pm 0.1 \cdot 10^{-6}$
	SLD solvent (Å $^{-2}$)	$6.36 \cdot 10^{-6}$	$6.36 \cdot 10^{-6}$	$6.36 \cdot 10^{-6}$	$6.36 \cdot 10^{-6}$
	background (cm^{-1})	0.009	0.003	0.002	0.004
	average core radius (Å)	750	740	750	740
	average shell thickness (Å)	41	43	45	42
	overall polydispersity	0.78 ± 0.01	0.76 ± 0.01	0.83 ±0.02	1 ± 0.02
	SLD core and solvent (Å $^{-2}$)	$6.36 \cdot 10^{-6}$	$6.36 \cdot 10^{-6}$	$6.36 \cdot 10^{-6}$	$6.36 \cdot 10^{-6}$
	SLD shell (Å $^{-2}$)	$4.78 \cdot 10^{-6}$	$4.78 \cdot 10^{-6}$	$4.78 \cdot 10^{-6}$	$4.78 \cdot 10^{-6}$
35	tail length (Å)	13.75 ± 0.06	13.52 ± 0.25	13.4 ± 0.26	13.0 ± 0.26
	headgroup thickness (Å)	5.24 ± 0.17	5.73 ± 0.18	6.65 ± 0.19	7.58 ± 0.15
	SLD tails (Å $^{-2}$)	$7.2 \cdot 10^{-6}$	$7.2 \cdot 10^{-6}$	$7.1 \cdot 10^{-6}$	$7.0 \cdot 10^{-6}$
	SLD headgroup (Å $^{-2}$)	$1.2 \cdot 10^{-6} \pm 0.1 \cdot 10^{-6}$	$1.2 \cdot 10^{-6} \pm 0.1 \cdot 10^{-6}$	$1.5 \cdot 10^{-6} \pm 0.1 \cdot 10^{-6}$	$2.98 \cdot 10^{-6} \pm 0.006 \cdot 10^{-6}$
	SLD solvent (Å $^{-2}$)	$6.36 \cdot 10^{-6}$	$6.36 \cdot 10^{-6}$	$6.36 \cdot 10^{-6}$	$6.36 \cdot 10^{-6}$
	background (cm^{-1})	0.009	0.003	0.007	0.004
	average core radius (Å)	510	520	540	560
	average shell thickness (Å)	38	39	41	41
	overall polydispersity	0.93 ± 0.02	0.84 ± 0.02	0.86 ± 0.01	0.88 ±0.02
	SLD core and solvent (Å $^{-2}$)	$6.36 \cdot 10^{-6}$	$6.36 \cdot 10^{-6}$	$6.36 \cdot 10^{-6}$	$6.36 \cdot 10^{-6}$
	SLD shell (Å $^{-2}$)	$4.78 \cdot 10^{-6}$	$4.78 \cdot 10^{-6}$	$4.78 \cdot 10^{-6}$	$4.78 \cdot 10^{-6}$

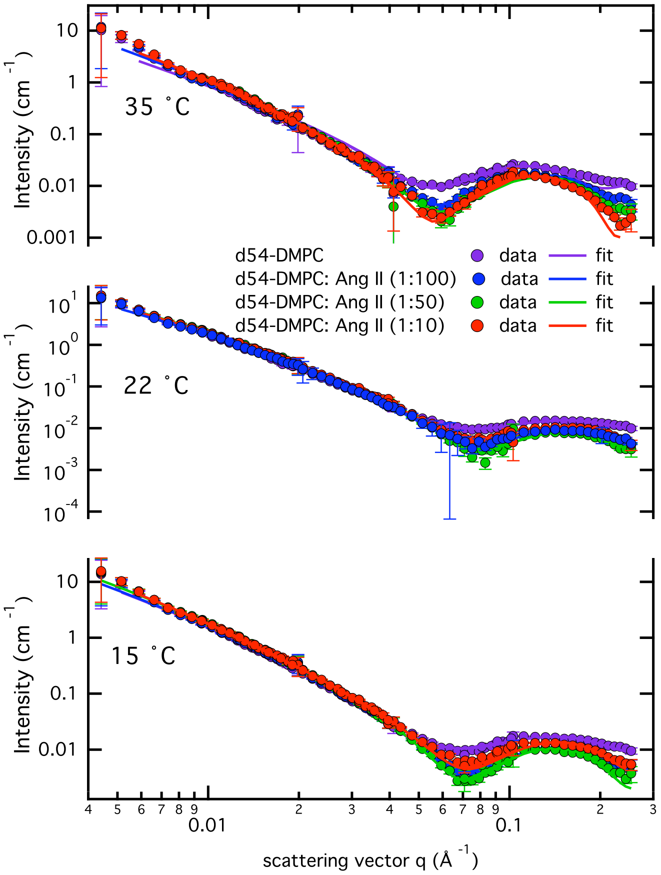

Figure 5.3: Small angle scattering data and according fits. Data is shown for experiments on pure d54-DMPC and mixtures of peptide and lipid of 1:100, 1:50, 1:10 and 1:5. The lines indicate the fits performed for the individual data sets.

length [94], [92], [169]. Based on this initial data, a fit to the experimental data became possible. For d54-DMPC in the fluid phase the tail length was fitted to 13.75 Å ± 0.06 Å with a SLD of $7.2 \cdot 10^{-6}$ Å $^{-2}$ and for the head group a thickness of 5.24 ± 0.17 Å with a SLD of $1.2 \cdot 10^{-6}$ Å $^{-2} \pm 0.1 \cdot 10^{-6}$ Å $^{-2}$. This sums up a membrane thickness of 37.98 Å which is in good agreement with literature values [92], [169]. With these parameters the according fits for the d54-DMPC data sets at lower temperatures were performed. For the sample at 15 ° C a smaller thickness of the head group and a longer hydrophobic region is expected. The head group is slightly tilted in the ripple phase and therefore the head group appears smaller in the ripple phase. Unmolten acyl chains are about 20 % longer than the molten ones, making a difference of about 3 Å between the two states. For the sample at 22 ° C the values should lie in between. The resulting thickness of the head group at 15 ° C is 4 Å and 4.99 Å at 22 ° C, correspondingly the tail length at 15 ° C was fitted with 16.3 Å and for 22 ° C with 15 Å . Based on the fits for the pure lipid samples the data with increasing peptide:lipid ratios were fitted. At 15 ° C the acyl chains were fitted with a constant length of 16.3 Å ± 0.32 Å . The thickness of the head group increased with the amount of peptide added, from 4 Å ± 0.06 Å for pure d54-DMPC to 4.2 Å ± 0.06 Å at a peptide:lipid ratio of 1:100, 5 Å ± 0.06 Å at a peptide:lipide ratio of 1:50 and finally to 7.5 Å ± 0.08 Å at a ratio of 1:10. The fits for the sample incubated at 22 ° C resulted in an slight decrease of the tail length, going from 14.5 Å ± 0.28 Å , 14.2 Å ± 0.28 Å to 13.6 Å ± 0.26 Å with increasing peptide concentration. In turn the head group size increases from 4.99 Å ± 0.19 Å over 6.09 Å ± 0.17 Å and 7.75 Å ± 0.14 Å to 7.89 Å ± 0.11 Å for the highest peptide amount in the sample. In the fluid phase, at 35 ° C, the tail length again decreases slightly from 13.52 Å ± 0.25 Å (peptide:lipid ratio 1:100) to 13.4 Å ± 0.26 Å (1:50) down to 13 Å ± 0.26 Å (1:10). The fitted values for the head group are 5.73 Å ± 0.18 Å , 6.65 Å ± 0.19 Å and 7.58 Å ± 0.15 Å with increasing peptide:lipid ratio.

In addition to changes in the length of the head group and the hydrophobic tail, the SLDs were adjusted during the fitting procedure. At 15 ° C the SLD for the head group changes from $1.1 \cdot 10^{-6}$ Å $^{-2} \pm 0.01 \cdot 10^{-6}$ Å $^{-2}$ over $1.9 \cdot 10^{-6}$ Å $^{-2} \pm 0.01 \cdot 10^{-6}$ Å $^{-2}$ to $3.3 \cdot 10^{-6}$ Å $^{-2} \pm 0.03 \cdot 10^{-6}$Å $^{-2}$ and accordingly for the acyl chains drops slightly to $7.1 \cdot 10^{-6}$Å $^{-2}$. At 22 ° C the SLD of the head group also increases with increasing amounts of peptides by around $1 \cdot 10^{-6}$ Å $^{-2}$, whereas the SLD of the tails stays constant. Finally for 35 ° C the SLD of the head group stays constant for the low peptide concentrations, but increases to $2.98 \cdot 10^{-6}$ Å $^{-2}$ for a peptide:lipid ratio of 1:10. The SLD of the tail is only insignificantly decreasing.

Neutron diffraction

Neutron diffraction experiments were performed on the membrane diffractometer V1 at the Berlin Neutron Scattering Center (BeNSC). Samples containing Ang II with peptide:lipid ratios of 1:10 and 1:50 were compared to pure d54-DMPC samples. Variation of the contrast, exchanging the rehydration medium from 100 % D_2O, 50 % D_2O and 50 % H_2O, and finally to 8 % H_2O and 92 % D_2O. The sample chambers were heated to 38 ° C to ensure all lipids are in the fluid phase. For the data analysis the lamellar d-spacing was determined from the 2θ values of the reflections using the Bragg equation. The structure factor amplitueds are obtained from the square rooted integral of the Gaussian fit of the diffraction peak followed by correction for absorption and Lorentz factor. Isomorphous replacement using D_2O/H_2O exchange allowed phase assignment. The structure factors are linearly related to the D_2O/H_2O ratios, as described in literature [170][171][172]. Raw data files and plots used for the phase assignment of the SFs are given in Appendix A in the protocol section. The resulting scattering density plots are given in Figure 5.4.

The plots are displaying the scattering density with respect to the distance from the bilayer center. The profiles are symmetrical, indicating a homogenous hydration and distribution of the peptide. Comparing panel A and B reveals a clear difference in the curves for the individual peptide concentrations and the different contrasts. The center of the bilayer remains unaffected, as the profiles for the inner 14 Å are the same for both contrasts. This is approximately the thickness of the acyl chains. For distances more than 14 Å away from the bilayer center the profiles start to differ. Relating the results for the pure d54-DMPC bilayer to the bilayers interacting with the peptide as displayed in Panel A the scattering density is decreasing with increasing amount of peptide. The same result can be observed for samples in pure H_2O as displayed in Panel B. The visibility of the changes is much smaller, as the contrast between the protonated headgroup, the peptide, the buffer used for rehydration is small. These changes in the scattering density is indicating a binding to the headgroup region, approaching the interface between the headgroup and the acyl chains for the peptide:lipid ration of 1:10.

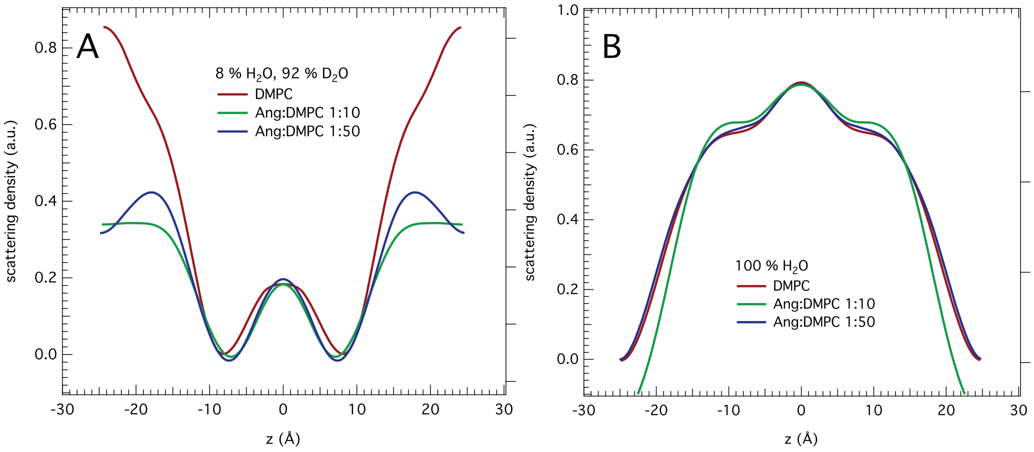

Figure 5.4: Scattering density profiles of membranes immersed in H_2O or a mixture of water and heavy water containing only 8% H_2O. Profiles from pure d54-DMPC and with peptide:lipid ratios of 1:10 and 1:50 are displayed.

Discussion

From the results of the DSC and the SANS data a concentration-dependent model for the binding of Ang II to membranes can be suggested. The DSC results for pure DMPC dispersions are in good agreement with previous studies [173]. The DSC experiments resulted in a shift of the main transition towards higher temperatures, hence a preferential binding to the gel phase is indicated. This is supported by the SANS data, as the increase in head group thickness at 15 ° C is the highest one for all the studied temperatures, accompanied by the highest increase in the SLD of the head group. The thickness of the tail stays unaffected, which can be explained by the close packing of the acyl chains in the gel phase, that can not be accessed by the peptide, even not at high peptide concentrations.

At 35 ° C the head group thickness also increases upon the binding of the peptide and in addition the tail length is slightly decreased, pointing towards a penetration of the peptide into the interface of the head group and the acyl chains. Close to the phase transition at 22 ° C this effect is even more pronounced, as the membrane is most flexible in this temperature region. This tendency is supported by the corresponding changes in the SLDs. At all temperatures the SLD of the tails stays basically constant, where as it increases for the head group region. This increase in the SLD is caused by the interaction of the peptide. The SLD of the peptide is lower than the one of the lipid headgroup, but the penetration of D_2O molecules into this region causes an increase in the SLD. For the samples at 22 ° C the SLD of the tails, again stays constant and the one for the head group is increased. At 35 ° C the SLD of the tails again can be considered as constant and the SLD of the head only changes for high concentrations of peptides.

Our data gives clear evidence for the adsorption of the peptide to the membrane surface, a tendency for preferred binding to the fluid phase is evident and only at high concentrations the peptide starts to penetrate closer to the interface between the head group and the acyl chains.

Looking at the previously published studies it becomes evident that they focus on the structure of the peptide in different chemical environments. Various experiments aimed to elucidate the peptide structure in the receptor, which would lead to a basis for rational design of Ang II peptidomimetics with potent antagonist properties. So far no experimental structural information of the peptide bound to the AT_1-receptor is available and therefore a number of secondary-structural features under various conditions with the attempt to mimic the natural environment of the receptor were performed [174][175][176][177][178] as well as in vitro binding studies of Losartan or Ang II [179].

Fatigati and Peach postulated a lipid milieu as local environment for Ang II therefore our interest focuses on the concentration-dependent interaction of Ang II on model membranes and the structural changes induced by the insertion, studied at different temperatures [180].

For the AT_1-receptor antagonist Losartan a membrane-mediated binding to the receptor was suggested, assuming the binding to the membrane surface, diffusing through the membrane bilayer, before binding to the receptor [181]. A similar mechanism may be plausible for Ang II, where the presence of the peptide is necessary for the translocation of the receptor into the membrane. Ang II may alter the membrane properties that the insertion of the receptor gets facilitated and the binding of Ang II to the active pocket in the receptor is further supported by prior binding to the membrane surface. Along with this discussion our study provides new insight into the interaction of Ang II with model membranes in this case DMPC vesicles. It can be concluded that Ang II influences the hydration of the head group and that this facilitates the insertion of the receptor in the membrane and subsequently the activation of the receptor by peptide.

Conclusion

In conclusion we could show that Ang II is in interaction with the surface of the membrane depending on the peptide concentration and the phase of the lipids. At low temperatures the peptide stays on the surface and in the head group region. With increasing temperatures and increased fluctuations close to the temperature of the phase transition a deeper penetration of the peptide into the bilayer is enabled. Ang II is altering the hydration of the lipid head groups, facilitating possible refolding of the receptor in the membrane and the subsequent binding of Ang II in the active site.

5.1.2 Losartan

Small angle x-ray scattering

SAXS experiments were performed on the cSAXS/X12SA beamline at the SLS at PSI. To trace the interaction of Losartan with lipid membranes data from pure DMPC samples is compared to data from mixtures of Losartan and DMPC. The experiments were performed with extruded unilamellar vesicles.

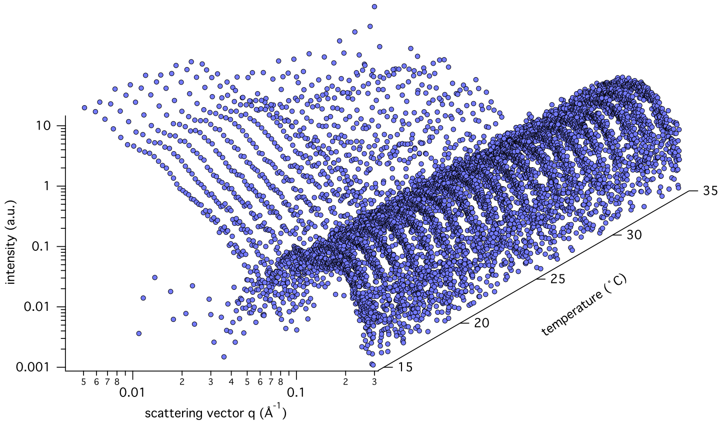

Figure 5.5: SAXS data of a Losartan DMPC mixture with a 1:100 ratio. The temperature was varied in one degree steps between 15 ° C and 35 ° C.

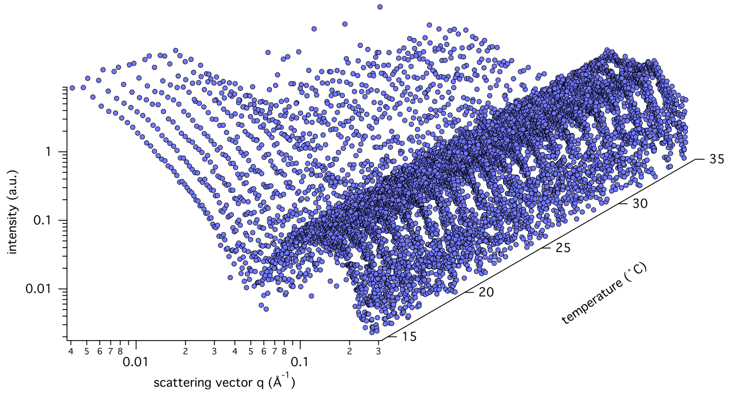

Figure 5.6: SAXS data of DMPC vesicles. The temperature was varied in one degree steps between 15 ° C and 35 ° C.

The SAXS results recorded for temperatures between 15 ° C and 35 ° C are displayed in Figure 5.5 for a Losartan:DMPC ratio of 1:100 and in Figure 5.6 for pure DMPC. The plots show a bilayer correlation peak with the onset at 0.06 $Å^{-1}$ for pure DMPC and again 0.06 $Å^{-1}$ for the sample containing Losartan. The peak width is depending on the bilayer distance, the heights on the contrast between the bilayer and the buffer. A shift in the onset of the peak indicates an increase in the bilayer thickness. For the two data sets show the bilayer correlation peak in the same region. The phase transition from gel to fluid phase is indicated by a drop in the scattering intensity. For the pure DMPC samples this drop in intensity is visible between 21 ° C and 22 ° C. The analog decrease in the Losartan data set is occurring between 22 ° C and 23 ° C.

Small angle neutron scattering

Similar to the studies on Ang II SANS was used to study morphological changes with special emphasize on changes in the bilayer structure. The KWS-2 SANS spectrometer at JCNS/FRM-2 was used to study protonated DMPC and chain deuterated DMPC.

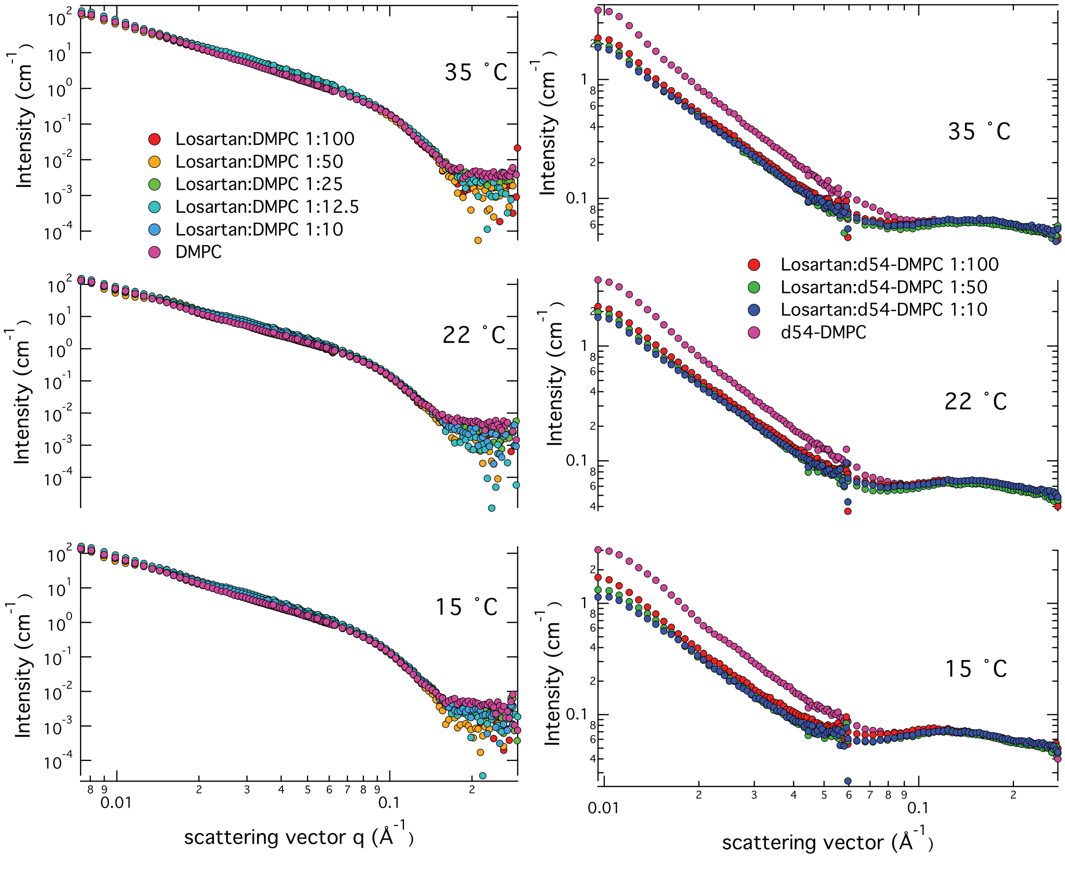

Figure 5.7: Small angle scattering data for DMPC and d54-DMPC upon interaction with Losartan. All experiments were performed at 15 ° C , 22 ° C and 35 ° C. (left) results from DMPC in comparison to scattering curves from samples with Losartan:DMPC ratios of 1:100, 1:50, 1:10 and 1:5. (right) data of experiments with pure d54-DMPC and mixtures of drug and lipid of 1:100, 1:50 and 1:10.

10 mM of protonated lipid were used and compared to drug:lipid ratios of 1:100, 1:50, 1:25, 1:12.5 and 1:10. In parallel samples with d54-DMPC were used containing the drug with ratios of 1:100, 1:50, and 1:10. All samples were extruded to produce unilamellar vesicles and prepared with heavy water buffers. Whereas the data from experiments performed with protonated lipids no changes in the low q-range got detected, small changes in the large q-range could be recorded. Upon addition of the drug the scattering is slightly decreased compared to the pure DMPC sample. More detailed information about the interaction can be derived from the studies with d54-DMPC. The scattering intensity in the high q-range for the chain-deuterated lipids is changing upon interaction with the drug. The onset of the bilayer correlation peak is shifting towards lower q-values. The minimum of the peak for pure d54-DMPC is at 0.09 Å $^{-1}$. For the highest drug concentration the peak onset is found at 0.6 Å $^{-1}$. The changes in the low q-range using the protonated and the chain-deuterated DMPC indicates a binding of the drug. Especially in the data set recorded with d54-DMPC a clear shift in the bilayer thickness is occurring upon interaction with Losartan. This shift corresponds to a broadening of the bilayer.

5.1.3 E-3174

Differential scanning calorimetry

DSC was performed as described above using DMPC, comparing it with different ratios of drug to lipid. The results are shown in Figure 5.8 and in Table 5.4. The main transition enthalpy is raised with increasing drug concentrations. The peak position of the main transition is not changing, whereas the values of the upper phase boundary are shifted towards higher temperatures. The pre-transition temperature is shifted towards lower temperatures. The data collected for the drug:lipid ratio of 1:10 don't match with the tendencies observed for the other ratios. The data points will not be considered for the further assumptions. The shift in the pre-transition peak and the decrease in the enthalpy is indicating a binding of the drug to the headgroup region. The shift of the temperature of the upper phase boundary towards higher temperatures for the highest drug concentration is proposing a preference for binding to the fluid phase. The broadening of the enthalpy peak for the high drug concentration can be caused by less cooperative melting of the acylchains. This is evidence for an effect on the hydrophobic core upon binding of drug molecules.

Table 5.4: Enthalpy and peak temperature of the main transition (peak$_{main}$) and pre-transition (peak$_{pre}$), as well as the upper phase boundary (UPB) for pure DMPC dispersions and DMPC mixed with E-3174 in the drug: lipid ratios 1:100, 1:50, 1:10, 1:5. The enthalpy c_p is given in J/mol · deg for the main transition (Enthalpy$_{main}$) and the pretransition (Enthalpy$_{pre}$).

sample	DMPC	1:100	1:50	1:10	1:5
Enthalpy$_{main}$	6.55 ± 0.91	13.7 ± 1.22	26.72 ± 1.23	5.71 ± 1.34	22.24 ± 1.45
Enthalpy$_{pre}$	1.37 ± 0.19	1.37 ± 0.20	2.38 ± 0.23	-	0.15 ± 0.24
peak$_{main}$ (°C)	23.6	23.63	23.59	23.49	23.4
peak$_{pre}$ (°C)	13.8	12.88	12.29	-	10.7
UPB (°C)	23.6	23.83	23.51	23.92	24.8

Small angle neutron scattering

SANS was performed with fully protonated DMPC and with chain-deuterated DMPC. The experiments were performed in D_2O to enhance the contrast. To take into account the phase behaviour of the lipids, data for three temperature points was collected (15 ° C, 22 ° C, 35 ° C) using unilamellar vesicles derived from extrusion. The SANS experiments performed with protonated DMPC don't reveal a change in the low q-range. Remarkable is the change in the high q-range indicating a change in the bilayer structure upon binding of the drug. The lowered intensity is representing a change in contrast in the bilayer. For protonated DMPC the contrast raising due to the scattering length density between the D_2O and the hydrogen atoms of the lipids. If the drug is now interacting with the head

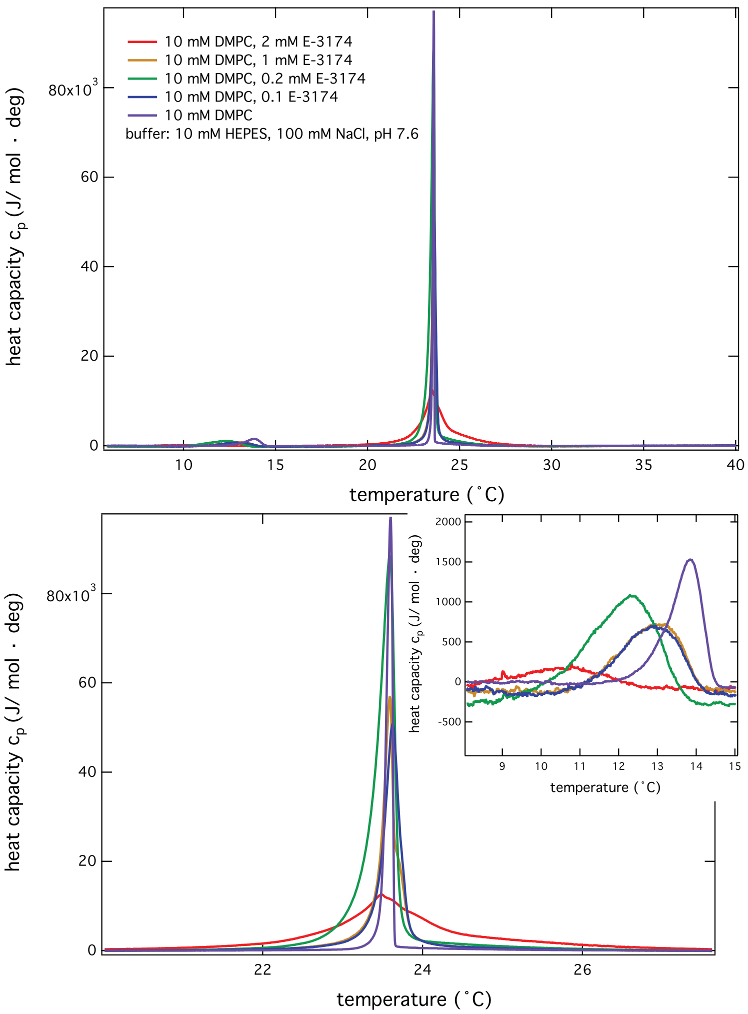

Figure 5.8: (top) DSC thermograms of DMPC samples upon interaction with E-3174 at different concentrations. (bottom) Cutout of the main transition region. (inset) Cutout on the pretransition

groups of the membrane and absorbing to the surface the contrast at the interface gets reduced. Upon intercalation of the drug between the headgroups the contrast gets further decreased, indicating that more drug molecules partition in the headgroup region. Referring to the data recorded with d54-DMPC changes in the radius of the vesicle and in the local bilayer structure. Proportional to the drug concentration the diameter of the vesicles is increasing. The bilayer thickness is changing the same fashion, showing a clear tendency for an insertion of the drug into the headgroup region. The advantage of using d54-DMPC is the sensitivity to trace changes in the headgroup region as described for Ang II. In this case the shift of the peak around 0.9 Å^{-1} is representing the binding of E-3174 intercalating between the headgroups. The change in vesicle diameter suggests an insertion of the drug perpendicular to the headgroup. Comparing the graphs for the individual temperature steps does not reveal remarkable differences.

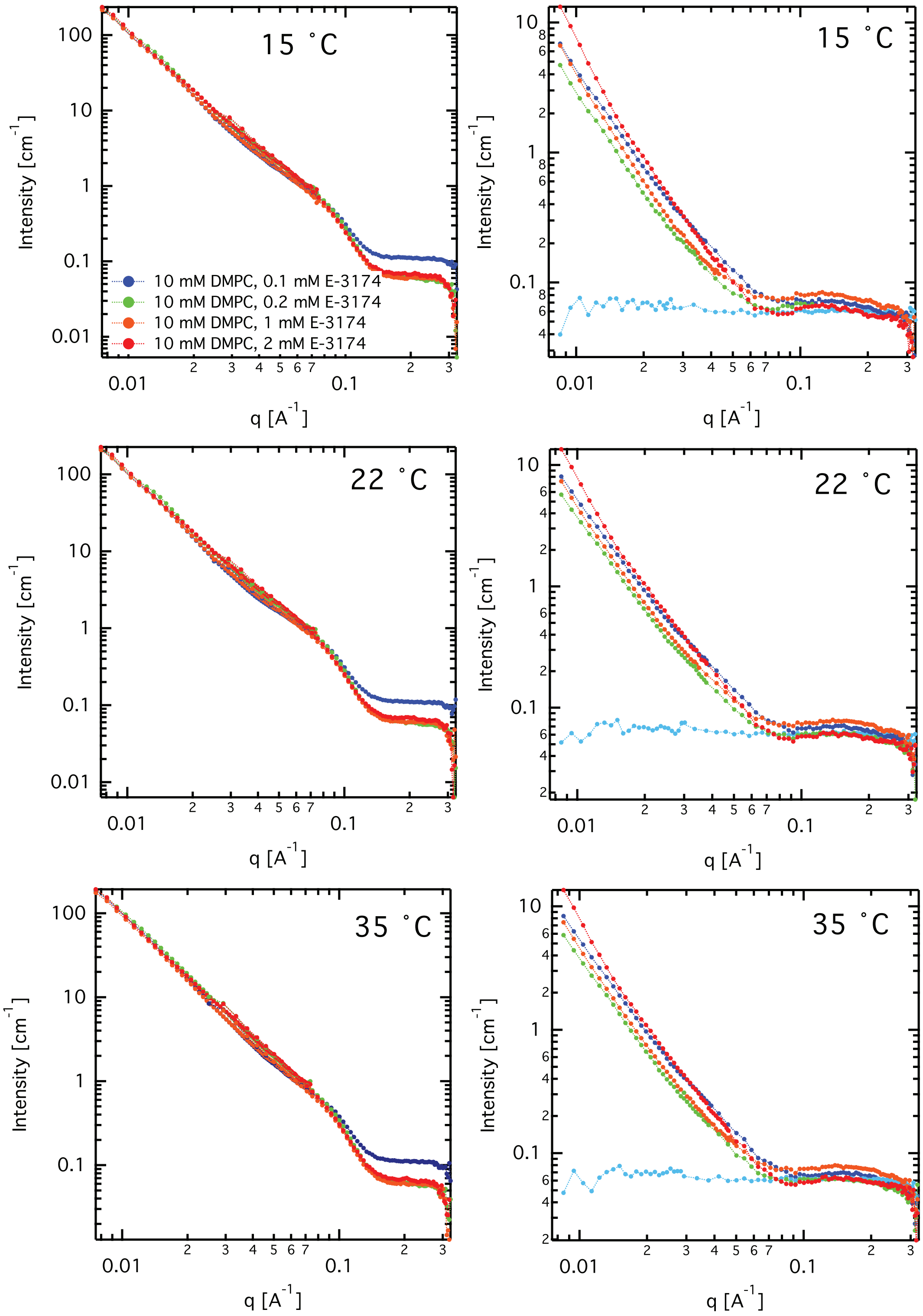

Figure 5.9: SANS curves for DMPC and d54-DMPC interacting with E-3174. All experiments were performed at 15 ° C, 22 ° C and 35 ° C. The drug concentrations of 0.1 mM, 0.2 mM, 1 mM and 2 mM were used (left) traces from experiments with DMPC are plotted. (right) results from experiments with d54-DMPC are given.

5.2 Conclusion

Experiments were performed with the three membrane-active compounds Ang II, Losartan and E-3174. Losartan is the first Ang II receptor antagonist that reached marketability after passing all clinical tests. In line with acting on a protein receptor, both Losartan and E-3174, show an interaction with the membrane, that may contribute to the final interaction with the membrane protein receptor [41]. More potent than Losartan itself is the carboxylic acid derivate E-3174 inhibiting the AT_1-receptor in a reversible non-competitive manner. *In vivo* the conversion of Losartan to E-3179 and finally E-3174 is catalyzed by cytochrome P_{450} enzymes, requiring NADPH and molecular oxygen [181]. Interesting is now to compare the binding capability to the membrane for all three compounds and elucidate in how far the binding behaviour differs, also with respect to the *in vivo* function.

For all three compounds a concentration dependent interaction with the membrane could be shown. The effects are pronounced in the DSC experiments performed for Ang II and E-3174. Changes in the calorimetric profile of DPPC dispersions with different Losartan concentrations was shown before [39]. Whereas Ang II is mainly absorbing to the surface, Losartan and E-3174 approach the interface between the headgroup and the acyl chains also at low concentrations. Even though chemically close to identical differences in the interaction of Losartan and E-3174 are evident. The same is observed in the SANS experiments in particular using chain-deuterated DMPC, enhancing the contrast between the D_2O in the buffer and the deuterated acyl chains compared to the protonated head group.

5.3 Discussion

Whereas all three compounds are interacting with the membrane, the binding of Losartan seems to have the strongest impact on the membrane structure. The structural difference between E-3174 and Losartan is a charge in the hydroxymethylgroup bound to the imidazole ring. Losartan is only carrying one charge allowing a stronger interaction of the butyl group to intercalate between the hydrophobic fatty acids. As shown by Fotakis *et al.* the interaction of Losartan with the membrane is increasing the order in the acyl chains[182]. E-3174 is twice negatively charged limiting the interaction to the headgroup region. This binding type is more similar to the effect observed for the binding of Ang II. The tendency for E-3174 to remain longer in the body and be more active than Losartan may be a result of this more natural binding behaviour, allowing a better interaction with the protein receptor. The absorption of all three compounds to the membrane surface may be the initial binding step that is also taking place in cells, mediating the binding of the compound to the membrane protein receptor.

In addition it was shown, that SANS is a suitable tool to study the interaction of a membrane-active peptide with the lipid surface. Key is the data analysis, as the combination of separated form factors gives rise to a variety of parameters that can describe a system on the level of the lamellae up to changes in the overall vesicle size. SANS and the method of contrast variation gives rise to an increase in contrast enabling a label-free sample preparation. The use of chain deuterated DMPC has the advantage that the contrast between the head group and the acyl chains is comparably high as the one between D_2O and the head group. This allows to trace even small changes in the headgroup region and at the interfaces between the solvent and the headgroup and between the headgroup and the interface along the acyl chains. The SANS results are in good agreement with the calorimetric and the neutron diffraction experiments.

In addition electrochemical impedance spectroscopy on a supported single bilayer were performed. The method allows accurate measurements on the bilayer capacity and resistance that are sensitive to changes on the lipid surface, the headgroup and the hydrophobic core. Impedance measurements revealed the same results for the interaction of the peptide with the membrane. Moreover this method is used to study the binding in response to variation of the pH.

Chapter 6

Summary and outlook

This thesis aimed to provide a better insight into the influence of charge on model membrane systems. This objective was addressed in two ways, by studying the anionic phospholipid DMPG varying the pH and the ionic strength and by tracing the interaction of charged membrane-active compounds with zwitterionic lipids.

Studies on DMPG dispersions revealed a close relation between the charge state of the headgroup and the complex melting behaviour. The phase transition is accompanied by an increase in the viscosity and a change in the optical density. Focusing on the transition region at low ionic strength a decrease in the bilayer undulations became evident, applying SAXS, SANS and Rheo-SANS.

Three membrane-active compounds were studied, Ang II, Losartan and E-3174, all involved in blood pressure regulation. For Ang II a concentration dependent interaction with the membrane, mainly absorbing to the surface, could be shown. SANS experiments showing the interaction of the peptide with d54-DMPC, analyzing the data with a separated form factor approach, was the first attempt to analyse the interaction of compounds. The method of contrast variation was shown to be a powerful tool increasing the contrast and allowing to elaborate the weak interactions upon binding of Ang II, E-3174 and Losartan mainly to the membrane surface.

To provide a more detailed picture about the bilayer undulations occurring at low ionic strength in the region of the phase transition inelastic neutron scattering techniques may be applied. Even though there may be some difficulties with the sample preparation, this type of experiments will provide a further inside into spacial fluctuations and yield information about the water layers in proximity to the bilayer surface. Basically all biological membranes are charged, making it even more important to get a more complete picture about the influence of the charge, especially on the water environment.

For the interaction studies it is advisable to continue the electrochemical impedance spectroscopy, yielding complementary results to the scattering methods and the calorimetric experiments. Inevitable is also the step towards a more realistic model system. A follow up study should be performed with reconstituted Angiotensin-receptors to get a better understanding about the *in vivo* function. A drawback here is the short list of methods capable of yielding meaningful information. Again the electrochemical impedance spectroscopy may be a step in the right direction.

Bibliography

[1] Margulis, L. (1975) Symbiotic theory of the origin of eukaryotic organelles; criteria for proof. *Symp Soc Exp Biol* pp. 21–38.

[2] Lang, B. F., Gray, M. W., and Burger, G. (1999) Mitochondrial genome evolution and the origin of eukaryotes. *Annu Rev Genet 33*, 351–97.

[3] Baluska, F. (2009) Cell-cell channels, viruses, and evolution: via infection, parasitism, and symbiosis toward higher levels of biological complexity. *Ann N Y Acad Sci 1178*, 106–19.

[4] Bao, G. and Suresh, S. (2003) Cell and molecular mechanics of biological materials. *Nat Mater 2*, 715–25.

[5] Meer, G. V., Voelker, D. R., and Feigenson, G. W. (2008) Membrane lipids: where they are and how they behave. *Nat Rev Mol Cell Biol 9*, 112–124.

[6] Bowie, J. (2005) Solving the membrane protein folding problem. *Nature 438*, 581–589.

[7] Zimmerberg, J. and Gawrisch, K. (2006) The physical chemistry of biological membranes. *Nature Chemical Biology 2*, 564–7.

[8] Karsenti, E. (2008) Self-organization in cell biology: a brief history. *Nat Rev Mol Cell Biol 9*, 255–62.

[9] Singer, S. and Nicolson, G. (1972) The fluid mosaic model of the structure of cell membranes. *Science 175*, 720–731.

[10] McLaughlin, S. and Murray, D. (2005) Plasma membrane phosphoinositide organization by protein electrostatics. *Nature 438*, 605–11.

[11] Feigenson, G. W. (2007) Phase boundaries and biological membranes. *Annual review of biophysics and biomolecular structure 36*, 63–77.

[12] Killian, J. and Nyholm, T. (2006) Peptides in lipid bilayers: the power of simple models. *Current Opinion in Structural Biology 16*, 473–479.

[13] Engelman, D. M. (2005) Membranes are more mosaic than fluid. *Nature 438*, 578–580.

[14] Gruenberg, J. (2003) Lipids in endocytic membrane transport and sorting. *Current opinion in cell biology 15*, 382–388.

[15] Hinderliter, A., Biltonen, R., and Almeida, P. (2004) Lipid modulation of protein-induced membrane domains as a mechanism for controlling signal transduction. *Biochemistry 43*, 7102–7110.

[16] Maxfield, F. R. and Tabas, I. (2005) Role of cholesterol and lipid organization in disease. *Nature 438*, 612–621.

[17] Williams, K. and Tabas, I. (1995) The response-to-retention hypothesis of early atherogenesis. *Arteriosclerosis, thrombosis, and vascular biology 15*, 551–561.

[18] Hansson, G. (2005) Inflammation, atherosclerosis, and coronary artery disease. *The New England journal of medicine 352*, 1685–1695.

[19] Berliner, J., Subbanagounder, G., Leitinger, N., Watson, A., and Vora, D. (2001) Evidence for a role of phospholipid oxidation products in atherogenesis. *Trends in Cardiovascular Medicine 11*, 142–147.

[20] Goerke, J. (1998) Pulmonary surfactant: functions and molecular composition. *Biochim Biophys Acta 1408*, 79–89.

[21] Träuble, H. and Eibl, H. (1974) Electrostatic effects on lipid phase transitions: membrane structure and ionic environment. *Proceedings of the National Academy of Sciences USA 71*, 214–9.

[22] Riske, K., Politi, M., Reed, W. F., and Lamy-Freund, M. (1997) Temperature and ionic strength dependent light scattering of dmpg dispersions. *Chemistry and Physics of Lipids 89*, 31–44.

[23] Schneider, M., Marsh, D., Jahn, W., and Kloesgen, B. (1999) Network formation of lipid membranes: Triggering structural transitions by chain melting. *Proceedings of the National Academy of Sciences USA 96*, 14312–14317.

[24] Heimburg, T. (2003) *Planar lipid bilayers (BLMs) and their applications*, eds. Tien, H. T. and Ottova-Leitmannova, A. (Elsevier, Amsterdam.), pp. 269–293.

[25] Riske, K., Amaral, L., Dobereiner, H., and Lamy, M. (2004) Mesoscopic structure in the chain-melting regime of anionic phospholipid vesicles: Dmpg. *Biophysical Journal 86*, 3722–3733.

[26] Riske, K. A., Amaral, L. Q., and Lamy, M. T. (2009) Extensive bilayer perforation coupled with the phase transition region of an anionic phospholipid. *Langmuir : the ACS journal of surfaces and colloids 25*, 10083–91.

[27] Epand, R. M. and Hui, S. W. (1986) Effect of electrostatic repulsion on the morphology and thermotropic transitions of anionic phospholipids. *FEBS Lett 209*, 257–60.

[28] Salonen, I., Eklund, K., Virtanen, J., and Kinnunen, P. (1989) Comparison of the effects of nacl on the thermotropic behaviour of sn-1'and sn-3'stereoisomers of 1, 2-dimyristoyl-sn-glycero-3-phosphatidylglycerol. *BBA-Biomembranes 982*, 205–215.

[29] Riske, K., Amaral, L., and Lamy-Freund, M. (2001) Thermal transitions of dmpg bilayers in aqueous solution: Saxs structural studies. *BBA-Biomembranes 1511*, 297–308.

[30] Riske, K., Dobereiner, H., and Lamy-Freund, M. (2002) Gel-fluid transition in dilute versus concentrated dmpg aqueous dispersions. *Journal of Physical Chemistry B-Condensed Phase 106*, 239–246.

[31] Lamy-Freund, M. and Riske, K. (2003) The peculiar thermo-structural behavior of the anionic lipid dmpg. *Chemistry and Physics of Lipids 122*, 19–32.

[32] Alakoskela, J.-M. I. and Kinnunen, P. K. J. (2007) Thermal phase behavior of dmpg: The exclusion of continuous network and dense aggregates. *Langmuir 23*, 4203–4213.

[33] Alakoskela, J., Parry, M., and Kinnunen, P. (2010) The intermediate state of dmpg is stabilized by enhanced positive spontaneous curvature. *Langmuir* p. in press.

[34] Castanho, M. A. R. B. and Fernandes, M. X. (2006) Lipid membrane-induced optimization for ligand-receptor docking: recent tools and insights for the "membrane catalysis" model. *Eur Biophys J 35*, 92–103.

[35] Alves, I., Goasdoué, N., Correia, I., Aubry, S., Galanth, C., Sagan, S., Lavielle, S., and Chassaing, G. (2008) Membrane interaction and perturbation mechanisms induced by two cationic cell penetrating peptides with distinct charge distribution. *BBA-General Subjects 1780*, 948–959.

[36] Ludtke, S. J., He, K., Heller, W. T., Harroun, T. A., Yang, L., and Huang, H. W. (1996) Membrane pores induced by magainin. *Biochemistry 35*, 13723–8.

[37] He, K., Ludtke, S., Worcester, D., and Huang, H. (1996) Neutron scattering in the plane of membranes: structure of alamethicin pores. *Biophysical Journal 70*, 2659–2666.

[38] Stearns, R. A., Chakravarty, P. K., Chen, R., and Chiu, S. H. (1995) Biotransformation of losartan to its active carboxylic acid metabolite in human liver microsomes. role of cytochrome p4502c and 3a subfamily members. *Drug Metab Dispos 23*, 207–15.

[39] Theodoropoulou, E. and Marsh, D. (1999) Interactions of angiotensin ii non-peptide at1 antagonist losartan with phospholipid membranes studied by combined use of differential scanning calorimetry and electron spin resonance spectroscopy. *Bba-Biomembranes 1461*, 135–146.

[40] Carpenter, K. A., Wilkes, B. C., and Schiller, P. W. (1998) The octapeptide angiotensin ii adopts a well-defined structure in a phospholipid environment. *Eur J Biochem 251*, 448–53.

[41] Mavromoustakos, T., Zoumpoulakis, P., and Kyrikou, I. (2004) Efforts to understand the molecular basis of hypertension through drug: Membrane interactions. *Current Topics in Medicinal Chemistry*.

[42] Svergun, D. and Koch, M. (2003) Small-angle scattering studies of biological macromolecules in solution. *Reports on Progress in Physics 66*, 1735–1782.

[43] Zernike, F. and Prins, J. (1927) Die beugung von röntgenstrahlen in flüssigkeiten als effekt der molekülanordnung. *Zeitschrift für Physik A Hadrons and Nuclei 41*, 184–194.

[44] Lindner, P. and Zemb, T., eds. (1991) *Neutron, x-ray and light scattering: introduction to an investigative tool for colloidal and polymeric systems: proceedings of the European workshop on Neutron, x-ray and light scattering as an investigative tool for colloidal and polymeric systems* (Amsterdam,New York: North-Holland), p. 375.

[45] Svergun, D. I., Feĭgin, L. A., and Taylor, G. W. (1987) *Structure analysis by small-angle x-ray and neutron scattering*. (Springer), p. 335.

[46] Stuhrmann, H., Schärpf, O., Krumpolc, M., Niinikoski, T., Rieubland, M., and Rijllart, A. (1986) Dynamic nuclear polarisation of biological matter. *Eur Biophys J 14*, 1–6.

[47] James, R. W. (1948) *The optical principles of the diffraction of x-rays*. (Ox Bow Press), p. 623.

[48] Fritz, G. and Glatter, O. (2006) Structure and interaction in dense colloidal systems: evaluation of scattering data by the generalized indirect fourier transformation method. *J. Phys.: Condens. Matter 18*, S2403–S2419.

[49] Debye, P. (1915) Zerstreuung von rontgenstrahlen. *Annalen der Physik 351*, 809–823.

[50] Debye, P. and Bueche, A. (1949) Scattering by an inhomogeneous solid. *Journal of Applied Physics 20*, 518–525.

[51] Guinier, A. (1939) Diffraction of x-rays of very small angles–application to the study of ultramicroscopic phenomena. *Ann. Phys.(Paris) 12*, 161–237.

[52] Abramowitz, M. and Stegun, I. A. (1972) *Handbook of Mathematical Functions with Formulas, Graphs, and Mathematical Tables*. (Dover Publications), p. 1060.

[53] Kratky, O., Pilz, I., and Schmitz, P. (1966) Absolute intensity measurement of small angle x-ray scattering by means of a standard sample. *Journal of Colloid and Interface Science 21*, 24–34.

[54] Jacrot, B. and Zaccai, G. (1981) Determination of molecular weight by neutron scattering. *Biopolymers 20*, 2413–2426.

[55] Letcher, J. and Schmidt, P. (1966) Small‚Äêangle x‚Äêray scattering determination of particle diameter distributions in polydisperse suspensions of spherical particles. *Journal of Applied Physics 37*, 649–655.

[56] Fedorova, I. and Schmidt, P. (1978) A general analytical method for calculating particle-dimension distributions from scattering data. *J Appl Crystallogr 11*, 405–411.

[57] Glatter, O. (1980) Determination of particle-size distribution functions from small-angle scattering data by means of indirect transformation method. *J Appl Crystallogr 13*, 7–11.

[58] Svergun, D., Semenyuk, A., and Feigin, L. (1988) Small-angle-scattering-data treatment by the regularization method. *Acta Crystallographica Section A 44*, 244–250.

[59] Knoll, W., Haas, J., Stuhrmann, H., Fuldner, H., Vogel, H., and Sackmann, E. (1981) Small-angle neutron scattering of aqueous dispersions of lipids and lipid mixtures. a contrast variation study. *J Appl Crystallogr 14*, 191–202.

[60] Knoll, W., Ibel, K., and Sackmann, E. (1981) Small-angle neutron scattering study of lipid phase diagrams by the contrast variation method. *Biochemistry 20*, 6379–83.

[61] Ibel, K. and Stuhrmann, H. (1975) Comparison of neutron and x-ray scattering of dilute myoglobin solutions. *Journal of molecular biology 93*, 255–265.

[62] Sears, V. (1992) Neutron scattering lengths and cross sections. *Neutron News 3*, 26–37.

[63] Bragg, W. (1913) The structure of some crystals as indicated by their diffraction of x-rays. *Proceedings of the Royal Society of London. Series A, Containing Papers of a Mathematical and Physical Character 89*, 248–277.

[64] Bragg, W. and Bragg, W. (1913) The reflection of x-rays by crystals. *Proceedings of the Royal Society of London. Series A, Containing Papers of a Mathematical and Physical Character* pp. 428–438.

[65] Ewald, P. (1969) Introduction to dynamical theory of x-ray diffraction. *Acta Crystall A-Crys A 25*, 103–108.

[66] Blaurock, A. (1982) Evidence of bilayer structure and of membrane interactions from x-ray diffraction analysis. *BBA-Reviews on Biomembranes 650*, 167–207.

[67] Lowe, B. and Smith, D. (1973) Glass electrode measurements in deuterium oxide. *Analytical Letters 6*, 903–907.

[68] Berger, N., Sachse, A., Bender, J., Schubert, R., and Brandl, M. (2001) Filter extrusion of liposomes using different devices: comparison of liposome size, encapsulation efficiency, and process characteristics. *International Journal of Pharmaceutics 223*, 55–68.

[69] MacDonald, R., Menco, B., Takeshita, K., Subbarao, N., and HU, L. (1991) Small-volume extrusion apparatus for preparation of large, unilamellar vesicles. *BBA-Biomembranes 1061*, 297–303.

[70] Kucerka, N., Pencer, J., Sachs, J. N., Nagle, J. F., and Katsaras, J. (2007) Curvature effect on the structure of phospholipid bilayers. *Langmuir 23*, 1292–1299.

[71] Teixeira, S., Zaccai, G., Ankner, J., Bellissentfunel, M., Bewley, R., Blakeley, M., Callow, P., Coates, L., Dahint, R., and Dalgliesh, R. (2008) New sources and instrumentation for neutrons in biology. *Chemical Physics 345*, 133–151.

[72] Neuhaus, J. and Petry, W. (2007) Correspondent's report: Forschungsneutronenquelle heinz maier-leibnitz (frm ii). *Neutron News 18*, 13–15.

[73] Fischer, W. (1997) Sinq—the spallation neutron source, a new research facility at psi. *Physica B: Physics of Condensed Matter 234-236*, 1202–1208.

[74] Blau, B., Clausen, K., Gvasaliya, S., Janoschek, M., Janssen, S., Keller, L., Roessli, B., Schefer, J., Tregenna-Piggott, P., and Wagner, W. (2009) The swiss spallation neutron source sinq at paul scherrer institut. *Neutron News 20*, 5–8.

[75] Bauer, G. (2010) Overview on spallation target design concepts and related materials issues. *Journal of Nuclear Materials 398*, 19–27.

[76] F.Groeschel, Dementjev, S., Heyck, H., Leung, W., Thomson, K., Wagner, W., and Zanini, L. (2008) *MEGAPIE-Irradiation Experience of the First Megawatt Liquid Metal Spallation Target*. (OECD Publishing).

[77] Radulescu, A. and Ioffe, A. (2007) Neutron guide system for small-angle neutron scattering instruments of the jülich centre for neutron science at frm-ii. *Nuclear Inst. and Methods in Physics Research 586*, 55–58.

[78] Aschauer, H., Fleischmann, A., and Schanzer, C. (2000) Neutron guides at the frm-ii. *Physica B: Physics of Condensed Matter 283*, 323–329.

[79] Kumar, M., Böni, P., and Clemens, D. (1998) Mechanical and structural properties of ni/ti multilayers and films: An application to neutron supermirrors. *Journal of Applied Physics 84*, 6940–6943.

[80] Rehm, C. and Agamalian, M. (2002) Flux gain for a next-generation neutron reflectometer resulting from improved supermirror performance. *Applied Physics A: Materials Science & Processing 74*, s1483–s1485.

[81] Berndt, I., Pedersen, J., Lindner, P., and Richtering, W. (2006) Influence of shell thickness and cross-link density on the structure of temperature-sensitive - poly-n-isopropylacrylamide-poly-n-isopropylmethacrylamide core-shell microgels investigated by small-angle neutron scattering. *Langmuir 22*, 459–468.

[82] Radlinski, A. (2006) Small-angle neutron scattering and the microstructure of rocks. *Reviews in Mineralogy and Geochemistry 63*, 363–397.

[83] DeBeer-Schmitt, L., Dewhurst, C. D., Hoogenboom, B. W., Petrovic, C., and Eskildsen, M. R. (2006) Field dependent coherence length in the superclean, high-kappa superconductor cecoin5. *Physical Review Letters 97*, 127001.

[84] Wang, H., Zhou, W., Ho, D., Winey, K., Fischer, J., Glinka, C., and Hobbie, E. (2004) Dispersing single-walled carbon nanotubes with surfactants: A small angle neutron scattering study. *Nano Letters 4*, 1789–1793.

[85] Lopez-Rubio, A. and Gilbert, E. (2009) Neutron scattering: A natural tool for food science and technology research. *Trends in Food Science & Technology* p. in press.

[86] Petoukhov, M. V. and Svergun, D. I. (2006) Joint use of small-angle x-ray and neutron scattering to study biological macromolecules in solution. *Eur Biophys J 35*, 567–76.

[87] Burckbuchler, V., Wintgens, V., Leborgne, C., Lecomte, S., Leygue, N., Scherman, D., Kichler, A., and Amiel, C. (2008) Development and characterization of new cyclodextrin polymer-based dna delivery systems. *Bioconjug Chem 19*, 2311–20.

[88] Wang, Y., Qiu, D., Cosgrove, T., and Denbow, M. (2009) A small-angle neutron scattering and rheology study of the composite of chitosan and gelatin. *Colloids and Surfaces B: Biointerfaces 70*, 254–258.

[89] Mason, P., Gaulin, B., Epand, R., Wignall, G., and Lin, J. (1999) Small angle neutron scattering and calorimetric studies of large unilamellar vesicles of the phospholipid dipalmitoylphosphatidylcholine. *Phys. Rev. E 59*, 3361–3367.

[90] Winter, R. (2002) Synchrotron x-ray and neutron small-angle scattering of lyotropic lipid mesophases, model biomembranes and proteins in solution at high pressure. *BBA-Protein Structure and Molecular Enzymology 1595*, 160–184.

[91] Mariani, P., Casadio, R., Carsughi, F., Ceretti, M., and Rustichelli, F. (1997) Structural analysis of membranes from photosynthetic bacteria by sans. *Europhys Lett 37*, 433–438.

[92] Kucerka, N., Nagle, J. F., Sachs, J. N., Feller, S. E., Pencer, J., Jackson, A., and Katsaras, J. (2008) Lipid bilayer structure determined by the simultaneous analysis of neutron and x-ray scattering data. *Biophysical Journal 95*, 2356–67.

[93] Kučerka, N., Nieh, M., Pencer, J., and Harroun, T. (2007) The study of liposomes, lamellae and membranes using neutrons and x-rays. *Current Opinion in Colloid & Interface Science 12*, 17–22.

[94] Nagle, J. F. and Tristram-Nagle, S. (2000) Structure of lipid bilayers. *Biochim Biophys Acta 1469*, 159–95.

[95] Nakano, M., Fukuda, M., Kudo, T., Miyazaki, M., Wada, Y., Matsuzaki, N., Endo, H., and Handa, T. (2009) Static and dynamic properties of phospholipid bilayer nanodiscs. *J Am Chem Soc 131*, 8308–8312.

[96] Balgavý, P., Dubnicková, M., Kucerka, N., Kiselev, M. A., Yaradaikin, S. P., and Uhríková, D. (2001) Bilayer thickness and lipid interface area in unilamellar extruded 1,2-diacylphosphatidylcholine liposomes: a small-angle neutron scattering study. *Biochim Biophys Acta 1512*, 40–52.

[97] Pencer, J. and Hallett, F. R. (2000) Small-angle neutron scattering from large unilamellar vesicles: an improved method for membrane thickness determination. *Physical review E, Statistical physics, plasmas, fluids, and related interdisciplinary topics 61*, 3003–8.

[98] Schmiedel, H., Almasy, L., and Klose, G. (2006) Multilamellarity, structure and hydration of extruded popc vesicles by sans. *Eur Biophys J Biophy 35*, 181–189.

[99] Tung, S., Lee, H., and Raghavan, S. (2008) A facile route for creating "reverse" vesicles: Insights into "reverse" self-assembly in organic liquids. *J. Am. Chem. Soc 130*, 8813–8817.

[100] Pencer, J., Nieh, M.-P., Harroun, T. A., Krueger, S., Adams, C., and Katsaras, J. (2005) Bilayer thickness and thermal response of dimyristoylphosphatidylcholine unilamellar vesicles containing cholesterol, ergosterol and lanosterol: a small-angle neutron scattering study. *Biochim Biophys Acta 1720*, 84–91.

[101] Gallová, J., Uhríková, D., Kucerka, N., Teixeira, J., and Balgavý, P. (2008) Hydrophobic thickness, lipid surface area and polar region hydration in monounsaturated diacylphosphatidylcholine bilayers: Sans study of effects of cholesterol and beta-sitosterol in unilamellar vesicles. *Biochim Biophys Acta 1778*, 2627–32.

[102] Kucerka, N., Nieh, M.-P., and Katsaras, J. (2009) Asymmetric distribution of cholesterol in unilamellar vesicles of monounsaturated phospholipids. *Langmuir : the ACS journal of surfaces and colloids 25*, 13522–7.

[103] Jacobson, K., Mouritsen, O., and Anderson, R. (2007) Lipid rafts: at a crossroad between cell biology and physics. *Nat Cell Biol 9*, 7–14.

[104] Pencer, J., Mills, T., Anghel, V., Krueger, S., Epand, R. M., and Katsaras, J. (2005) Detection of submicron-sized raft-like domains in membranes by small-angle neutron scattering. *The European physical journal E, Soft matter 18*, 447–58.

[105] Winter, R. and Jeworrek, C. (2009) Effect of pressure on membranes. *Soft Matter 5*, 3157–3173.

[106] Nakano, M., Fukuda, M., Kudo, T., Matsuzaki, N., Azuma, T., Sekine, K., Endo, H., and Handa, T. (2009) Flip-flop of phospholipids in vesicles: Kinetic analysis with time-resolved small-angle neutron scattering. *The journal of physical chemistry. B 113*, 6745–6748.

[107] Kiselev, M., Zemlyanaya, E., Ryabova, N., Hauss, T., Dante, S., and Lombardo, D. (2008) Water distribution function across the curved lipid bilayer: Sans study. *Chemical Physics 345*, 185–190.

[108] Lundquist, A., Wessman, P., Rennie, A. R., and Edwards, K. (2008) Melittin-lipid interaction: a comparative study using liposomes, micelles and bilayer disks. *Biochim Biophys Acta 1778*, 2210–6.

[109] Huang, H. W. (2000) Action of antimicrobial peptides: two-state model. *Biochemistry 39*, 8347–52.

[110] Han, M., Mei, Y., Khant, H., and Ludtke, S. J. (2009) Characterization of antibiotic peptide pores using cryo-em and comparison to neutron scattering. *Biophysical Journal 97*, 164–172.

[111] Biemann, P., Haese-Seiller, M., and Staron, P. (2000) User-friendly software for sans data reduction. *Physica B 276*, 156–157.

[112] Keiderling, U. (1997) A new software package for sans data processing at the hahn-meitner-institut in berlin, germany. *Physica B: Condensed Matter 234*, 1111–1113.

[113] Drews, A., Barker, J., and Glinka, C. (1997) Development of a thermal-neutron double-crystal diffractometer for usans at nist. *Physica B: Condensed Matter 241*, 189–191.

[114] Frielinghaus, H., Pipich, V., Radulescu, A., Heiderich, M., Hanslik, R., Dahlhoff, K., Iwase, H., Koizumi, S., and Schwahn, D. (2009) Aspherical refractive lenses for small-angle neutron scattering. *J Appl Crystallogr 42*, 681–690.

[115] Schaefer, D. and Agamalian, M. (2004) Ultra-small-angle neutron scattering: a new tool for materials research. *Current Opinion in Solid State and Materials Science 8*, 39–47.

[116] Kim, M. and Glinka, C. (2006) Ultra small angle neutron scattering study of the nanometer to micrometer structure of porous vycor. *Microporous and Mesoporous Materials 91*, 305–311.

[117] Takeshita, H., Kanaya, T., Nishida, K., Kaji, K., and Takahashi, T. (2000) Ultra-small-angle neutron scattering studies on phase separation of poly (vinyl alcohol) gels. *Phys. Rev. E 61*, 2125–2128.

[118] Nettesheim, F., Zipfel, J., Olsson, U., Renth, F., Lindner, P., and Richtering, W. (2003) Pathway of the shear-induced transition between planar lamellae and multilamellar vesicles as studied by time-resolved scattering techniques. *Langmuir 19*, 3603–3618.

[119] Porcar, L., Hamilton, W., Butler, P., and Warr, G. (2002) Scaling of shear-induced transformations in membrane phases. *Physical Review Letters 89*, 168301.

[120] Förster, S., Konrad, M., and Lindner, P. (2005) Shear thinning and orientational ordering of wormlike micelles. *Physical Review Letters*.

[121] Porcar, L., Hamilton, W., Butler, P., and Warr, G. (2003) Scaling of structural and rheological response of l 3 sponge phases in the" sweetened" cetylpyridinium/hexanol/dextrose/brine system. *Langmuir 19*, 10779–10794.

[122] Stellbrink, J., Lonetti, B., Rother, G., Willner, L., and Richter, D. (2008) Shear induced structures of soft colloids: Rheo-sans experiments on kinetically frozen pep–peo diblock copolymer micelles. *J. Phys.: Condens. Matter 20*, 404206.

[123] Lindner, P. and Oberthür, R. (1984) Apparatus for the investigation of liquid systems in a shear gradient by small angle neutron scattering (sans). *Revue Phys. Appl 19*, 759–763.

[124] Porcar, L., Hamilton, W., Butler, P., and Warr, G. (2002) A vapor barrier couette shear cell for small angle neutron scattering measurements. *Rev. Sci. Instrum. 73*, 2345–2355.

[125] Hay, H., Pattenden, N., and Egelstaff, P. (1958) The scattering of 4 a neutrons by a beryllium crystal. *Acta Crystallographica 11*, 228–229.

[126] Trewhella, J. (1997) Insights into biomolecular function from small-angle scattering. *Current Opinion in Structural Biology 7*, 702–708.

[127] Svergun, D., Richard, S., Koch, M., Sayers, Z., Kuprin, S., and Zaccai, G. (1998) Protein hydration in solution: experimental observation by x-ray and neutron scattering. *Proceedings of the National Academy of Sciences 95*, 2267–2272.

[128] Garidel, P., Förster, G., Richter, W., Kunst, B., Rapp, G., and Blume, A. (2000) 1, 2-dimyristoyl-sn-glycero-3-phosphoglycerol (dmpg) divalent cation complexes: an x-ray scattering and freeze-fracture electron microscopy study. *Physical Chemistry Chemical Physics 2*, 4537–4544.

[129] Nieh, M., Glinka, C., Krueger, S., Prosser, R., and Katsaras, J. (2002) Sans study on the effect of lanthanide ions and charged lipids on the morphology of phospholipid mixtures. *Biophysical Journal 82*, 2487–2498.

[130] Katsaras, J., Pencer, J., Nieh, M., Abraham, T., Kucerka, N., and Harroun, T. (2008) *Neutron and X-Ray Scattering from Isotropic and Aligned Membranes*, ed. Nag, K. (John Wiley and Sons, Inc.).

[131] Neylon, C. (2008) Small angle neutron and x-ray scattering in structural biology: recent examples from the literature. *Eur Biophys J 37*, 531–541.

[132] Henrich, B., Bergamaschi, A., Broennimann, C., Dinapoli, R., Eikenberry, E., Johnson, I., Kobas, M., Kraft, P., Mozzanica, A., and Schmitt, B. (2009) Pilatus: a single photon counting pixel detector for x-ray applications. *Nuclear Instruments and Methods in Physics Research Section A: Accelerators, Spectrometers, Detectors and Associated Equipment 607*, 247–249.

[133] Koch, M. and Bras, W. (2008) Synchrotron radiation studies of non-crystalline systems. *Annu. Rep. Prog. Chem., Sect. C 104*, 35–80.

[134] Urban, C. and Schurtenberger, P. (1998) Characterization of turbid colloidal suspensions using light scattering techniques combined with cross-correlation methods. *Journal of Colloid and Interface Science 207*, 150–158.

[135] Hiemenz, P. C. and Rajagopalan, R. (1997) *Principles of colloid and surface chemistry*. (CRC Press), p. 650.

[136] Brown, W. (1996) *Light scattering: principles and development,Äé*. (Oxford University Press), p. 528.

[137] Tripathy, S. K., Kumar, J., and Nalwa, H. S. (2002) *Handbook of Polyelectrolytes and Their Applications*, eds. Tripathy, S. K., Kumar, J., and Nalwa, H. S. (American Scientific Publishers), p. 1000.

[138] Koppel, D. (1972) Analysis of macromolecular polydispersity in intensity correlation spectroscopy: the methods of cumlants. *The Journal of Chemical Physics 57*, 4814–4821.

[139] Bruylants, G., Wouters, J., and Michaux, C. (2005) Differential scanning calorimetry in life science: thermodynamics, stability, molecular recognition and application in drug design. *Current medicinal chemistry 12*, 2011–20.

[140] Westh, P. (2009) Experimental approaches to membrane thermodynamics. *Soft Matter 5*, 3249–3257.

[141] Blume, A. (1983) Apparent molar heat capacities of phospholipids in aqueous dispersion. effects of of chain length and head group structure. *Biochemistry 22*, 5436–5442.

[142] Heimburg, T. and Biltonen, R. (1996) A monte carlo simulation study of protein-induced heat capacity changes and lipid-induced protein clustering. *Biophysical Journal 70*, 84–96.

[143] Ebel, H., Grabitz, P., and Heimburg, T. (2001) Enthalpy and volume changes in lipid membranes. i. the proportionality of heat and volume changes in the lipid melting transition and its implication for the elastic constants. *J Phys Chem B 105*, 7353–7360.

[144] Heerklotz, H. (2004) The microcalorimetry of lipid membranes. *J. Phys.: Condens. Matter 16*, R441–R467.

[145] Koukoulitsa, C., Kyrikou, I., Demetzos, C., and Mavromoustakos, T. (2006) The role of the anticancer drug vinorelbine in lipid bilayers using differential scanning calorimetry and molecular modeling. *Chemistry and Physics of Lipids 144*, 85–95.

[146] Severcan, F., Sahin, I., and Kazanci, N. (2005) Melatonin strongly interacts with zwitterionic model membranes—evidence from fourier transform infrared spectroscopy and differential scanning calorimetry. *BBA-Biomembranes 1668*, 215–222.

[147] Jung, D., Powers, J. P., Straus, S. K., and Hancock, R. E. W. (2008) Lipid-specific binding of the calcium-dependent antibiotic daptomycin leads to changes in lipid polymorphism of model membranes. *Chemistry and Physics of Lipids 154*, 120–8.

[148] Seto, G., Marwaha, S., Kobewka, D., Lewis, R., Separovic, F., and McElhaney, R. (2007) Interactions of the australian tree frog antimicrobial peptides aurein 1.2, citropin 1.1 and maculatin 1.1 with lipid model membranes: differential scanning calorimetric and fourier transform infrared spectroscopic studies. *BBA-Biomembranes 1768*, 2787–2800.

[149] Pabst, G., Grage, S., Dannerpongratz, S., Jing, W., Ulrich, A., Watts, A., Lohner, K., and Hickel, A. (2008) Membrane thickening by the antimicrobial peptide pgla. *Biophysical Journal 95*, 5779–5788.

[150] Plotnikov, V., Brandts, J., Lin, L., and Brandts, J. (1997) A new ultrasensitive scanning calorimeter. *Analytical Biochemistry 250*, 237–244.

[151] Pawley, J. B. (2006) *Handbook of biological confocal microscopy*, ed. Pawley, J. B. (Springer), p. 985.

[152] Cremer, C., Cremer, T., and Artikel, N. (1978) Considerations on a laser-scanning-microscope with high resolution and depth in field. *microscopica acta 81*, 31–44.

[153] Schneider, M. F. (1999) Reversible ausbildung eines membrannetzwerks im schmelzregime von phospholipiden.

[154] Spinozzi, F., Paccamiccio, L., Mariani, P., and Amaral, L. (2010) Melting regime of the anionic phospholipid dmpg: New lamellar phase and porous bilayer model. *Langmuir* p. in press.

[155] Buttgereit, R., Marth, M., Roths, T., and Honerkamp, J. (2000) Some aspects of data analysis of multi-angle dynamic light scattering. *Macromolecular Symposia 162*, 173–190.

[156] Buttgereit, R., Marth, M., and Honerkamp, J. (2000) Estimation of distribution functions in light scattering: the regularization method and bayes' ansatz. *Macromolecular Symposia 162*, 149–172.

[157] Nallet, F., Laversanne, R., and Roux, D. (1993) Modelling x-ray or neutron scattering spectra of lyotropic lamellar phases: interplay between form and structure factors. *J. Phys. II France 3*, 487–502.

[158] Hartung, J., Helfrich, W., and Kloesgen, B. (1994) Transformation of phosphatidylcholine multilayer systems in a large excess of water. *Biophysical Chemistry 49*, 77–81.

[159] Javierre, I., Nallet, F., Bellocq, A., and Maugey, M. (2000) Structure and dynamic properties of a polymer-induced sponge phase. *J. Phys.: Condens. Matter 12*, A295–A299.

[160] Wu, J., Wei, W., Wang, L., Su, Z., and Ma, G. (2007) A thermosensitive hydrogel based on quaternized chitosan and poly (ethylene glycol) for nasal drug delivery system. *Biomaterials 28*, 2220–2232.

[161] Feil, H., Bae, Y., Feijen, J., and Kim, S. (1992) Mutual influence of ph and temperature on the swelling of ionizable and thermosensitive hydrogels. *Macromolecules 25*, 5528–5530.

[162] Paradossi, G., Cavalieri, F., and Chiessi, E. (2005) Proton fluctuations and water diffusion in dextran chemical hydrogels studied by incoherent elastic and quasielastic neutron scattering. *Carbohydrate research 340*, 921–927.

[163] White, L., Ringo, J., and Dowse, H. (1992) Effects of deuterium oxide and temperature on heart rate in drosophila melanogaster. *Journal of Comparative Physiology B: Biochemical, Systemic, and Environmental Physiology 162*, 278–283.

[164] Pittendrigh, C., Caldarola, P., and Cosbey, E. (1973) A differential effect of heavy water on temperature-dependent and temperature-compensated aspects of the circadian system of drosophila pseudoobscura. *Proceedings of the National Academy of Sciences USA 70*, 2037.

[165] Mezei, F. (1972) Neutron spin echo: a new concept in polarized thermal neutron techniques. *Zeitschrift für Physik A Hadrons and Nuclei*.

[166] Pfeiffer, W., König, S., Legrand, J., and Bayerl, T. (1993) Neutron spin echo study of membrane undulations in lipid multibilayers. *Europhysics Letters 23*, 475–462.

[167] Farago, B., Richter, D., Huang, J., Safran, S., and Milner, S. (1990) Shape and size fluctuations of microemulsion droplets: The role of cosurfactant. *Physical Review Letters 65*, 3348–3351.

[168] Kiselev, M., Lesieur, P., Kisselev, A., Lombardo, D., and Aksenov, V. (2002) Model of separated form factors for unilamellar vesicles. *Applied Physics A: Materials Science & Processing 74*, s1654–s1656.

[169] Kiselev, M. A., Zemlyanaya, E. V., Aswal, V. K., and Neubert, R. H. H. (2006) What can we learn about the lipid vesicle structure from the small-angle neutron scattering experiment? *Eur Biophys J 35*, 477–93.

[170] Franks, N. P. and Lieb, W. R. (1979) The structure of lipid bilayers and the effects of general anaesthetics. an x-ray and neutron diffraction study. *Journal of molecular biology 133*, 469–500.

[171] Bradshaw, J. P., Davies, S. M., and Hauss, T. (1998) Interaction of substance p with phospholipid bilayers: A neutron diffraction study. *Biophysical Journal 75*, 889–95.

[172] Dante, S., Hauss, T., and Dencher, N. A. (2003) Insertion of externally administered amyloid beta peptide 25-35 and perturbation of lipid bilayers. *Biochemistry 42*, 13667–72.

[173] Heimburg, T. (2000) A model for the lipid pretransition: coupling of ripple formation with the chain-melting transition. *Biophysical Journal 78*, 1154–1165.

[174] Surewicz, W. and Mantsch, H. (1988) Conformational properties of angiotensin ii in aqueous-solution and in a lipid environment - a fourier transform infrared spectroscopic investigation. *J Am Chem Soc 110*, 4412–4414.

[175] Garcia, K. C., Ronco, P. M., Verroust, P. J., Brünger, A. T., and Amzel, L. M. (1992) Three-dimensional structure of an angiotensin ii-fab complex at 3 a: hormone recognition by an anti-idiotypic antibody. *Science 257*, 502–7.

[176] Shin, Y. and Yoo, S. (1996) Conformational study of angiotensin ii. *Biopolymers 38*.

[177] Cho, N. and Asher, S. (1996) Uv resonance raman and absorption studies of angiotensin ii conformation in lipid environments. *Biospectroscopy 2*, 71–82.

[178] Joseph, M. P., Maigret, B., Bonnafous, J. C., Marie, J., and Scheraga, H. A. (1995) A computer modeling postulated mechanism for angiotensin ii receptor activation. *J Protein Chem 14*, 381–98.

[179] Chansel, D., Bizet, T., Vandermeersch, S., Pham, P., Levy, B., and Ardaillou, R. (1994) Differential regulation of angiotensin ii and losartan binding sites in glomeruli and mesangial cells. *Am J Physiol 266*, F384–93.

[180] Fatigati, V. and Peach, M. (1988) Development of a new fluorescent angiotensin ii probe. *American Journal of Physiology- Cell Physiology 255*, C452–C458.

[181] Zoumpoulakis, P., Daliani, I., Zervou, M., Kyrikou, I., Siapi, E., Lamprinidis, G., Mikros, E., and Mavromoustakos, T. (2003) Losartan's molecular basis of interaction with membranes and at1 receptor. *Chemistry and Physics of Lipids 125*, 13–25.

[182] Fotakis, C., Christodouleas, D., Chatzigeorgiou, P., Zervou, M., Benetis, N.-P., Viras, K., and Mavromoustakos, T. (2009) Development of a cp 13p nmr broadline simulation methodology for studying the interactions of antihypertensive at1 antagonist losartan with phospholipid bilayers. *Biophysical Journal 96*, 2227–2236.

[183] Kline, S. (2006) Reduction and analysis of sans and usans data using igor pro. *J Appl Crystallogr 39*, 895–900.

[184] Guinier, A. and Fournet, G. (1955) *Small-angle Scattering of X-rays (translated from french)*. (John Wiley), p. 268.

[185] Bartlett, P. and Ottewill, R. (1992) A neutron-scattering study of the structural of a bimodal colloidal crystal. *J Chem Phys 96*, 3306–3318.

Appendix A

Materials and protocols

A.1 Materials

A.1.1 buffer preparation

A number of buffers were needed to perform the different experiments, containing different amounts of salt and adjusted to different pH values. In general all buffers were prepared with ultrapure water from a Millipore system with a resistance larger than 18 MΩ was used. Powder equivalent 10 mM of the buffering substance was dissolved in water together with the required amount of NaCl and stirred until all solid particles were dissolved. The pH was adjusted using a pH meter, adding small quantities of HCl and NaOH to the solution. To show the dependence on the ionic strength solutions with different amounts of NaCl were prepared accordingly. The buffer always contained 10 mM NaCl and the pH was

Table A.1: Buffers used for experiments at different pH-values. All buffering substances were used at a concentration of 10 mM. NaCl was added on demand.

pH	buffering substance
4	citric acid
5	citric acid
6	MES
7	HEPES
8	HEPES
9	TAPS
10	sodium bicarbonate
11	sodium bicarbonate

Neutron diffraction

Neutron diffraction experiments are performed on supported, aligned bilayer stacks. To ensure a good sample quality the lipid powder immersed in buffer. One sample was prepared with pure d54-DMPC, the rest was prepared with Ang II dissolved in the buffer prior to mixing with the lipid powder. To ensure a homogenous distribution of the peptide and later good alignment of the bilayer the sample was sonicated for at least 15 min, until the dispersion became transparent. The clear dispersion was transfered to a quartz wafer and dried over night. To ensure a good alignment of the bilayer stacks the samples was tempered at least 12 hours at 40 ° C in a petri dish with a D_2O reservoir. After tempering the wafer is transferred to the sample holder. To reach an equilibrium the sample is incubated under controlled humidity for another 6 hours prior to the experiment.

The data collection reveals Bragg peaks up to the fifth order. The raw data files are shown in Figure A.1.

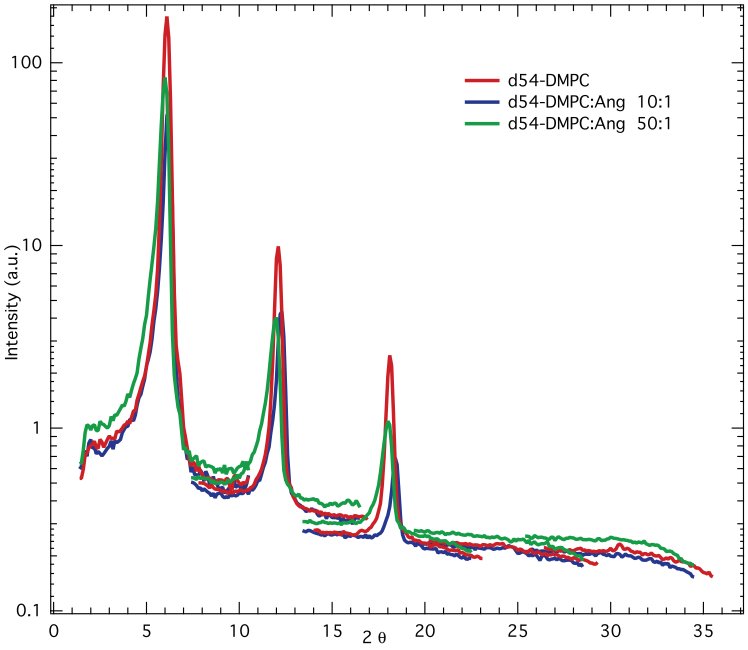

Figure A.1: Neutron diffraction data, showing the Bragg peaks recorded for pure d54-DMPC and mixtures with Ang II.

Based on the diffraction peaks the structure factors are calculated. To assign the correct phases the SFs for the different diffraction orders are plotted, giving linear plots in dependence of the D_2O concentration as shown in Figure A.2. In case of the right assignment the point are lying on a straight line. For the higher order diffraction this criterium is fullfilled. For the lower diffraction orders small derivations are observed, caused by shifts in the diffraction peak position.

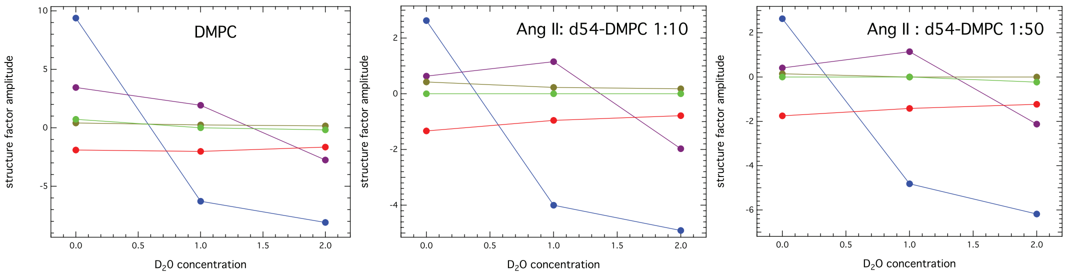

Figure A.2: Plots used for the assignment of the phases of the SFs. The SFs for the individual diffraction order and the contrast are plotted.

Confocal Fluorescence Microscopy

To perform the confocal fluorescence microscopy different samples with fluorescent dyes needed to be prepared. The protocol used was the same for all dyes. A dye:lipid ratio of 1:500 was used. The dyes were dissolved in methanol and the appropriate amount was added to the lipid dissolved in a mixture of Chloroform and Methanol. To ensure a precise mixing a dilution series from a dye stock solution was performed. The mixture was dried under a nitrogen stream and subsequently dried in a vacuum bell. The dried film was stored in the freezer if necessary and rehydrated right before the experiment. Buffer was added to the lipid film and the vial was thoroughly vortex to ensure a homogeneous mixing of the sample. For the measurement the dispersion was transferred to LabTek^{TM} chambers (NUNC, Rochester, NY, USA).

Appendix B

Suppliers of chemicals

DMPC	Avanti Polar Lipids	Alabaster, AL, USA
Chloroform	Fluka Analyticals	St. Louis, MO, USA
citric acid	Sigma Aldrich	St. Louis, MO, USA
d-54 DMPC	Avanti Polar Lipids	Alabaster, AL, USA
D_2O	Sigma Aldrich	St. Louis, MO, USA
Di-C_{18}	Invitrogen	Carlsbad, CA, USA
DMPG	Avanti Polar Lipids	Alabaster, AL, USA
NBD-head	Avanti Polar Lipids	Alabaster, AL, USA
NBD-chain	Avanti Polar Lipids	Alabaster, AL, USA
E-3174	Merck Sharp & Dohme Corp	Whitehouse Station, NJ, USA
HEPES	Sigma Aldrich	St. Louis, MO, USA
Losartan	Merck Sharp & Dohme Corp	Whitehouse Station, NJ, USA
MES	Sigma Aldrich	St. Louis, MO, USA
Methanol	Fluka Analyticals	St. Louis, MO, USA
NaCl	Sigma Aldrich	St. Louis, MO, USA
sodium bicarbonate	Sigma Aldrich	St. Louis, MO, USA
TAPS	Sigma Aldrich	St. Louis, MO, USA
TriTC- DHPE	Invitrogen	Carlsbad, CA, USA

Appendix C

Mathematical Models for data fitting

The analysis of the SANS data was performed using the software package described by Kline [183] based on macros running under Igor Pro (WaveMetrics Inc., Portland, USA). This data analysis software provides the possibilty to undergo non-linear data fitting, based on a variety of included form factors.

C.1 SANS data analysis for DMPG

C.1.1 Rheo-SANS - Core shell cylinder with polydisperse radius

Rheo-SANS data resulted in data with a slope of -1 indicating an elongated hollow particle. The data was hence fitted with a cylinder FF allowing for the variation of the radius. The FF is containing a set of variable parameters. The spacial dimensions are defined by the particle length and the radius of the cylinder, defining the core. The thickness of the bilayer along the cylinder and at the cap is given. In addition to the spacial parameters differences in the scattering length density (SLD) are calculated for the core, the shell and the solvent. As vesicles are displaying a size distribution a FF needs to be chosen that allows to adjust for this polydispersity. The scattering intensity is scaled according to the forward scattering and a parameter for the background is added.

$$I(q) = background + \frac{scale}{V_p} \sum_{R_p} n\left(R_p, \sigma_p\right)\ P\left(q, R_p, R_l, H_p, H_l, \rho_p, \rho_l, \rho_{solv}\right) \tag{C.1}$$

$$n(R_p) = \frac{exp\left(-\frac{1}{2}\left[\frac{ln(R_p/R_0)}{\sigma_p}\right]^2\right)}{\sqrt{(2\pi)}\sigma_p R_p} \tag{C.2}$$

$$P(q) = \int_0^{\pi/2} sin\theta \cdot d\theta \cdot \left(V_l\left(rho_l - \rho_{solv}\right)\frac{sin\left(\frac{qh_l cos\theta}{2}\right)2J_1(qR_l sin\theta)}{\frac{qH_l cos\theta}{2}qR_l sin\theta} + V_p\left(\rho_p - \rho_l\right)\frac{sin\left(\frac{qh_p cos\theta}{2}\right)2J_1(qR_p sin\theta)}{\frac{qH_p cos\theta}{2}qR_p sin\theta}\right)^2 \tag{C.3}$$

$$V_x = \pi R_x^H{}_x \tag{C.4}$$

$J_1(x)$ is the first order Bessel function. Theta is defined as the angle between the cylinder axis and the scattering vector, q. The integral over theta averages the form factor over all possible orientations of the cylinder with respect to q The core radius = R_p, core length = H_p (the mean core radius is R_o). Note that the shell radius and shell length incorporate the dimensions of the bare particle (i.e H_l = H_p + 2 $\cdot$ face thickness and R_l = R_p + radial thickness). Sigma is equivalent to the standard deviation of the log-normal distribution.

The form factor P(q) is normalised by multiplying by scale/V_p. If scale represents the volume fraction of the core particles then the multiplication factor is the number density of particles and an absolute intensity is returned. Note that the shell has a constant thickness around the edge of the particle. More details about the FF can be found in [184].

C.2 SANS data analysis for Ang II

To analyse the data in particular the combination of form factors became necessary. Following the separated form factor approach, as published by Kiselev et al. [168], two form factors were summed up in order to reflect the changes in the sample with an appropriate model. One of the two form factors describes a lamellae, taking into account different scattering length densities for the chain and the head group region [157][159]. Second a form factor representing a polydisperse vesicle [185] was used. The initially used scattering length densities (SLDs) were calculated values. The scattering length values for D_2O were fixed. For the bilayer thickness, the length of the head group and the hydrophobic region of pure DMPC literature values were used as an orientation [94][92][169].

C.2.1 Form factor of polydisperse vesicle

The form factor (FF) for a vesicle with a polydisperse core with constant shell thickness was used as described by Bartlett and Ottewill [185]. To derive the relation and to define the parameters of the FF a suspension of noninteracting particles is considered showing only coherent scattering and no multiple scattering.

$$\frac{d\Sigma}{d\omega}(\mathbf{q}) = n\left\langle |\sum_{i(v)} b_i exp(i\mathbf{q}\cdot\mathbf{r}_i)|^2 \right\rangle \tag{C.5}$$

b_i the atomic scattering length density, n is the number density of particles and the sum is adding over all atoms in the particle volume v . As SANS experiments do not yield information on the atomic scale the atomic scattering lengths b_i can be replaced by the locally averaged scattering length density defined as

$$\rho(\mathbf{r}) = \sum_i b_i \delta(\mathbf{r}-\mathbf{r}_i) \tag{C.6}$$

b_i is the scattering length of the atom at the position r_i. Replacing the sum in Eq. C.5 by an integral yields an expression for the scattering from a suspension of noninteracting spheres

$$\frac{d\Sigma}{d\omega}(\mathbf{q}) = nF(\mathbf{q})^2 \tag{C.7}$$

where the scattering amplitude id defined by the Fourier transform

$$F(\mathbf{q}) = \int \left[\rho(\mathbf{r}) - \rho_m\right] exp(i\mathbf{q}\cdot\mathbf{r})d\mathbf{r} \tag{C.8}$$

ρ_m is the scattering length density of the buffer. Assuming a spherically symmetric profile $\rho(r)$ the scattering amplitude for a single particle reduces to

$$F(q) = 4\pi \int r^2 \left[\rho(r) - \rho_m\right] \frac{sin\ qr}{qr} dr \tag{C.9}$$

The scattering profile has the form

$$\rho(r) = \begin{cases} \rho_c & r \le r_c \\ \rho_s & r_c < r \le r_c + \Delta \end{cases} \tag{C.10}$$

with r_c the radius of the spherical core and the scattering length density

ρ_c surrounded by a shell of the thickness Δ with the scattering length density ρ_s. Correspondingly the particle scattering amplitude can be written as

$$F(x) = \frac{4\pi}{q^3}(\rho_s - \rho_c)\{\gamma j(x + \delta x) - j(x)\} \tag{C.11}$$

$\rho = \Delta / r_c$ and $x = q\, r_c$. The function $j(x) = \sin x - x \cos x$. The scaled medium contrast $\gamma = (\rho_m - \rho_s) / (\rho_c - \rho_s)$ determines the relative proportion of the scattering from the core or the shell. To take into account the polydispersity of the vesicle a particle distribution is introduced. For this Eq. C.7 needs to be averaged over the particle size distribution, assuming that only the size of the particle core is varying whereas the shell thickness Δ is constant. For this the single particle FF F^2 $(q\, r_c)$ is replaced by the size average

$$\bar{F}^2(q\bar{r}_c) = \int_0^\infty G(r_c) F^2(q r_c) dr_c \tag{C.12}$$

$G(r_c)$ is the normalized probability to find a particle with a core radius between r_c and $r_c + d\, r_c$, $\bar{r}_c$ is the mean core radius. For the distribution of the mean core radius a Schulz distribution is picked. The normalized form of this distribution is

$$G(r_c) = \frac{r_c^Z}{\Gamma(Z+1)} \left(\frac{Z+1}{\bar{r}_c}\right)^{Z+1} \cdot exp\left[-\frac{r_c}{\bar{r}_c}(Z+1)\right] \tag{C.13}$$

with $\bar{r}_c$ is the mean core radius and Z is related to the normalized polydispersity σ_c of the particle core radius distribution

$$\sigma_c^2 = \left(\frac{\bar{r_c^2}}{\bar{r}_c^2} - 1\right) = \frac{1}{Z+1} \tag{C.14}$$

C.2.2 Lamellar form factor

For the description of the bilayer a lamellar FF was used as published by [157][159]. To describe the different segments of the bilayer a two-square profile is defined, with two variable parameters for each segment. The segments are the headgroup with the thickness δ_H and the scattering length density σ_H and accordingly the tail with the thickness δ_T and the scattering length density σ_T. To derive the form factor the following assumptions were made

$$\Delta\sigma_H = \sigma_H - \sigma_{solvent} \tag{C.15}$$

$$\Delta\sigma_T = \sigma_T - \sigma_H \tag{C.16}$$

$$2(\delta_H + \delta_T) = \text{ total bilayer thickness} \tag{C.17}$$

The resulting FF has the following format.

$$P(q) = \frac{4}{q^2}\left\{\Delta\rho_H\left[sin\left[q(\rho_H+\rho_T)\right] - sin(q\rho_T)\right] + \Delta\rho_T sin(q\delta_T)\right\}^2 \tag{C.18}$$

List of Figures

List of Tables

Abbreviations

ACE	Angiotensin converting enzyme
Ang II	Angiotensin II
BeNSC	Berlin Neutron Science Center
d54-DMPC	chain deuterated DMPC
Di-C_{18}	1,1’-dioctadecyl-3,3,3’,3’-tetramethyl-indocarbocyanine perchlorate
DLS	Dynamic light scattering
DMPC	Dimyristoylphoshpatidylcholine
DMPG	Dimyristoylphosphatidylglycerol
DSC	Differential scanning calorimetry
FF	Form factor
FRM (G)	Forschungsreaktor München (Geesthacht)
HEPES	4-(2-hydroxyethyl)-1-piperazineethanesulfonic acid
JCNS	Jülich Center for Neutron Science
NBD-chain	1,2-dimyristoyl-sn-glycero-3-phosphoethanolamine-N-(7-nitro-2-1,3 -benzoxadiazol-4-yl) (ammonium salt)
NBD-head	1-myristoyl-2- {12-[(7-nitro-2-1,3-benzo-xadiazol-4-yl) amino] lauroyl }-sn-glycero-3- [phospho-rac- (1-glycerol)] (ammonium salt)
pH (D)	potentia hydrogenii (deuteron)
PSI	Paul Scherrer Institut
RAS	Renin-angiotensin system
Rheo	Rheology
SAXS	Small angle x-ray scattering
SF	Structure factor
SLD	Scattering length density
SLS	Static light scattering
SLS	Swiss Light Source
TriTC-DHPE	N-(6-tetramethylrhodaminethiocarbamoyl) - 1,2-dihexadecanoyl-sn-glycero-3-phosphoethanolamine, triethylammonium salt
UPB	Upper phase boundary
(U)SANS	(Ultra)small angle neutron scattering

Acknowledgements

First I would like to thank Thomas Heimburg and Thomas Gutberlet for giving me the opportunity to work on the topics performed in this thesis and introducing me to the world of Membrane Biophysics.

A bit more than three years ago I decided to leave the world of biochemistry, molecular biology and protein crystallography and change a synchrotron in ground floor against a neutron source across the street (at least for a while). This made me move from Hamburg to Switzerland and moreover to change my lifestyle completely. Starting from the second month of my PhD I became a traveller, exploring new countries, meeting new people, attending workshops and conferences and doing experiments. How exciting these times were, there is of course a reverse side, that I don't want to stress here, but it is one of the reasons why quite a number of people deserve a special thanks. I would like to thank all the beamline scientists supporting me during and after my neutron and x-ray scattering experiments, Vasil Haramus, Henrich Frielinghaus, Aurel Radulescu, Vitaliy Pipich, Thomas Hauss, Bruno Deme and Andreas Menzel. Further the cSAXS group at PSI deserves a thanks for allowing to use the light scattering setup and early experiments during the commissioning of the beamline.

A number of people deserve an honest thank for their support and their ideas during the course of the project. Joachim Kohlbrecher for help with the design of cuvettes suitable for the use at the cSAXS beamline and having just the right glasses in a drawer of his desk. Lionel Porcar for measuring some of my samples at NIST and answering my questions about Rheo-SANS. The biggest thanks deserves Thomas Gutberlet for

Beni Thielemann and Conradin Kraemer at PSI and later Andreas Blicher at NBI for being just the right office mates.